



## 저작자표시-비영리-변경금지 2.0 대한민국

이용자는 아래의 조건을 따르는 경우에 한하여 자유롭게

- 이 저작물을 복제, 배포, 전송, 전시, 공연 및 방송할 수 있습니다.

다음과 같은 조건을 따라야 합니다:



저작자표시. 귀하는 원저작자를 표시하여야 합니다.



비영리. 귀하는 이 저작물을 영리 목적으로 이용할 수 없습니다.



변경금지. 귀하는 이 저작물을 개작, 변형 또는 가공할 수 없습니다.

- 귀하는, 이 저작물의 재이용이나 배포의 경우, 이 저작물에 적용된 이용허락조건을 명확하게 나타내어야 합니다.
- 저작권자로부터 별도의 허가를 받으면 이러한 조건들은 적용되지 않습니다.

저작권법에 따른 이용자의 권리는 위의 내용에 의하여 영향을 받지 않습니다.

이것은 [이용허락규약\(Legal Code\)](#)을 이해하기 쉽게 요약한 것입니다.

[Disclaimer](#)

이학박사학위논문

Observed Characteristics and Modeling  
of Monsoonal Precipitation in  
Bangladesh and Northeast India

방글라데시와 인도 북동부 지역  
몬순 강수의 관측된 특성 및 모델링

2021년 8월

서울대학교 대학원  
협동과정 계산과학전공  
Tanvir Ahmed



Observed Characteristics and Modeling  
of Monsoonal Precipitation in  
Bangladesh and Northeast India

방글라데시와 인도 북동부 지역 몬순 강수의 관측된  
특성 및 모델링

지도교수 백 종 진

이 논문을 이학박사 학위논문으로 제출함

2021년 5월

서울대학교 대학원

협동과정 계산과학전공

Tanvir Ahmed

Tanvir Ahmed의 이학박사 학위논문을 인준함

2021년 7월

위 원 장      박 성 수

부위원장      백 종 진

위      원      김 상 우

위      원      이 현 호

위      원      송 효 종





Observed Characteristics and Modeling  
of Monsoonal Precipitation in  
Bangladesh and Northeast India

by

Tanvir Ahmed

A Dissertation Submitted to the Faculty of the  
Graduate School of Seoul National University in  
Partial Fulfillment of the Requirements for the  
Degree of Doctor of Philosophy

August 2021

Advisory Committee:

Professor Sungsu Park, Chair  
Professor Jong-Jin Baik, Advisor  
Professor Sang-Woo Kim  
Professor Hyunho Lee  
Professor Hyo-Jong Song



Copyright © 2021 by Tanvir Ahmed  
All rights reserved.

The manuscript printed and bound in the present form is intended for personal use and distribution among the author's colleagues, friends, and family.

An electronic copy of the document has been submitted to the Seoul National University Library with minor formatting modifications in accordance with the University's requirements.

This dissertation contains contents of the following journal publications:

A., Jin & Baik, 2020. *Asia-Pac. J. Atmos. Sci.* 56, 593–602;

A., Jin & Baik, 2020. *Quart. J. Roy. Meteor. Soc.* 146, 3368–3383.

List valid at the time of submission—Material from the dissertation may produce up to two additional publications in the future.

*A catalogue record is available from the National Library of Korea*

Manuscript typeset with Microsoft<sup>®</sup> Word

Title pages typeset with L<sup>A</sup>T<sub>E</sub>X using a user-modified version of cumg-template

References follow the American Meteorological Society (AMS) citation style.

To view the author's profile, visit  
[www.researchgate.net/profile/Ahmed-Tanvir](http://www.researchgate.net/profile/Ahmed-Tanvir)

Printed in South Korea

1 3 5 7 8 6 4 2

*Dedicated to my beloved sons*

*Faiyaz Al Farabi*

*&*

*Fawad Al Fahmi*



## **Abstract**

Bangladesh is under the strong influence of the South Asian monsoon. Extensive damages caused by frequent severe flood events in this country call for a study of nationwide precipitation climatology. Here, we examine spatiotemporal variations of precipitation in Bangladesh using rain gauge data at 35 stations for the period 2003–2016. The annual precipitation amount in Bangladesh is 2263 mm, and it shows large spatial variations. The annual precipitation amount is large in the southeastern coastal region of the country and the region close to the Meghalaya Plateau, and it is small in the west central region. 17% and 73% of the annual precipitation amount are observed in the pre-monsoon season (March to May) and monsoon season (June to September), respectively. The pattern of the diurnal variation of precipitation differs depending on regions of Bangladesh. In the northern region of the country, the precipitation maximum occurs in the late night to early morning in both the pre-monsoon and monsoon seasons. The late night to early morning maximum of precipitation is associated with the large horizontal convergence of low-level water vapor flux. The Himalaya Mountains and the Meghalaya Plateau together with more nighttime moisture transport due to the strengthened nighttime low-level wind seem to play roles in enhancing nighttime precipitation. In the southwestern region of the country, the precipitation maximum is observed in the early evening in the pre-monsoon season, which is associated with the large convective instability in the afternoon, and it is observed in the early afternoon in the monsoon season. In the southeastern region of the country, the diurnal variability of precipitation is smallest in the pre-monsoon season compared with other regions of the country in the

pre-monsoon and monsoon seasons and the precipitation maximum occurs in the late night to early morning in the monsoon season.

Satellite retrieval-based precipitation data with high spatial and temporal resolutions give opportunity for precipitation research in regions with coarse networks of precipitation-measuring instruments. This study evaluates the applicability of the Integrated Multi-satellitE Retrievals for Global Precipitation Measurement (IMERG) data to studying precipitation in Bangladesh and surrounding regions, and examines important features of the diurnal variation of precipitation in these regions using the IMERG data and the cyclostationary empirical orthogonal function (CSEOF) analysis method. The IMERG data capture the overall patterns of the diurnal variation of precipitation well, except for the overestimation of the degree of diurnal variability in the pre-monsoon season. The spatial distribution of precipitation is also captured well, except for the drastic horizontal change in precipitation within the northeastern region of Bangladesh. These encourage the use of the IMERG data for studying precipitation characteristics in Bangladesh and surrounding regions. Through the CSEOF analysis, the pre-monsoonal precipitation is characterized by the enhanced precipitation in the northern region of Bangladesh and the Meghalaya Plateau region in the late night to early morning. The monsoonal precipitation consists of two contrasting CSEOF modes. One shows enhanced precipitation in the northern region of the Bay of Bengal in 0600–1500 LST, related to the strong westerly moisture transport over the Bay of Bengal. The other shows enhanced precipitation in the southern slopes of the Meghalaya Plateau and Himalayan Foothills in 0000–0600 LST, associated with the strong southwesterly moisture transport toward these slopes that is neither blocked or deflected by the Arakan Mountains.

Accretion process in bulk cloud microphysics schemes can be parameterized using the stochastic collection equation (SCE). In this study, the collection efficiency of each raindrop–cloud droplet pair is applied to the SCE to derive a new accretion parameterization that considers a strong variability of accretion rate depending on the cloud droplet and raindrop size distributions. To evaluate the new accretion parameterization (NP), it is implemented into a cloud-resolving model, replacing the original accretion parameterization (OP) based on the continuous collection equation. In the idealized simulations of deep convective clouds, NP predicts overall larger accretion rates and smaller autoconversion rates than OP. The resultant high accretion/autoconversion rate ratio in NP increases the mean raindrop size. This induces faster sedimentation of raindrops that is associated with the earlier onset of surface precipitation and also weakens the evaporation cooling of raindrops that can affect the thermodynamics and dynamics of clouds. Meanwhile, for a given pair of rainwater and cloud water mass contents, the accretion rates in NP have a broad distribution while those in OP are less variant, suggesting that the dependence of the accretion rates on bulk microphysical properties other than the mass contents also needs to be properly considered in accretion parameterizations. Most of the aforementioned differences between the two accretion parameterizations found in the idealized simulations are also found in the real-case simulations of a precipitation event over Bangladesh but the differences are smaller, and the spatial distribution of the accumulated precipitation amount is relatively well predicted by NP compared to OP.

The Meghalaya Plateau (MP) located in Northeast India is one of the rainiest regions in the world. On 18–19 August 2015, the southern slope of MP received



extremely heavy precipitation with the 1-day accumulated precipitation amount of 745 mm at Mawsynram. This study investigates the dynamical, thermodynamical, and cloud microphysical processes associated with this event through numerical simulations with fine horizontal resolutions (1 km and 1/3 km). The control (CNTL) simulation with 1-km grid spacing successfully reproduces the observed spatial pattern of accumulated precipitation. From 1500 LST 18 to 0000 LST 19 (P1) when the low-level jet that carries warm and moist air toward MP is relatively weak, the upslope region receives a moderate amount of precipitation which is initiated over this region due to the orographic lifting, while almost no precipitation is received there in the simulation without MP (noMP). Warm microphysical processes play dominant roles in the precipitation in P1. From 0000 to 0900 LST 19 (P2) when the low-level jet is enhanced, the noMP simulation shows a moderate amount of precipitation in the upslope region and the CNTL simulation shows much heavier precipitation there. Deep convective systems developed upwind of MP move toward MP. These convective systems merge together and strengthen over the upslope region. The accretion process is substantially enhanced by the vigorous updrafts at low levels over the steep slope of MP, resulting in heavy precipitation. The simulation with 1/3-km grid spacing shows much heavier precipitation in the upslope region than the CNTL simulation. The increased horizontal resolution makes the slopes steeper, which results in further intensification of the updrafts over this region. This increase in simulated precipitation reduces the deviation from the rain gauge observation, implying the importance of very high horizontal resolutions in the simulations of extremely heavy precipitation in MP. Further study investigates the sensitivities of simulated precipitation to various physical parameterization schemes and the performance of the multiphysics

ensemble. Six different cloud microphysics, four different PBL, and three different radiation schemes are used. The performance of each scheme and the multiphysics ensemble are evaluated. An improved cloud microphysics scheme that includes the stochastic autoconversion and accretion processes is also evaluated. Simulations with different microphysics schemes show similar spatial distribution patterns of precipitation, but precipitation intensity differs depending on which microphysics scheme is employed. The multiphysics ensemble shows better performance compared to most of the individual ensemble members. The performance of the improved microphysics scheme is similar to that of the multiphysics ensemble, improving precipitation prediction considerably.

**Keywords:** monsoonal precipitation, Bangladesh, Meghalaya Plateau, diurnal variation, IMERG, accretion parameterization, extreme precipitation

**Student ID:** 2017-33971

# Contents

<b>Abstract</b>	<b>i</b>
<b>Contents</b>	<b>vi</b>
<b>List of figures</b>	<b>x</b>
<b>List of tables</b>	<b>xix</b>
<b>1 Introduction</b>	<b>1</b>
1.1 Characteristics of observed precipitation in Bangladesh.....	1
1.2 Applicability of IMERG data to precipitation studies in and around Bangladesh.....	5
1.3 Raindrop-cloud droplet accretion parameterization in bulk microphysics schemes.....	8
1.4 Extreme monsoonal precipitation in the Meghalaya Plateau region .....	12
<b>2 Spatiotemporal variations of precipitation in Bangladesh revealed by     nationwide rain gauge data</b>	<b>16</b>
2.1 Data .....	16
2.2 Results and discussion .....	16
2.2.1 Yearly and monthly variation of precipitation .....	16
2.2.2 Diurnal variation of precipitation .....	25

<b>3</b>	<b>Evaluation and CSEOF analysis of IMERG data for precipitation studies in Bangladesh and surrounding regions</b>	<b>38</b>
3.1	IMERG data description and CSEOF analysis method.....	38
3.1.1	IMERG data description .....	38
3.1.2	CSEOF analysis method.....	41
3.2	Results and discussion .....	44
3.2.1	Evaluation of IMERG data .....	44
3.2.2	CSEOF analysis.....	52
3.2.2.1	Pre-monsoon .....	52
3.2.2.2	Monsoon .....	58
<b>4</b>	<b>Development of a physically based raindrop-cloud droplet accretion parameterization and its evaluation through cloud and precipitation simulations</b>	<b>65</b>
4.1	A new accretion parameterization .....	65
4.2	Evaluation through cloud-resolving model simulation .....	65
4.2.1	Idealized simulations .....	76
4.2.2	Real-case simulations.....	88
<b>5</b>	<b>Dynamical, thermodynamical, and cloud microphysical processes associated with extremely heavy precipitation in the Meghalaya Plateau region</b>	<b>101</b>
5.1	Case description and simulation setup.....	101
5.1.1	Case description .....	101

5.1.2 Model description and simulation design .....	103
5.2 Results .....	107
5.2.1 Validation and precipitation characteristics .....	107
5.2.2 Dynamical and thermodynamical characteristics.....	112
5.2.3 Cloud microphysical characteristics .....	119
5.2.4 Local topographic effect on precipitation .....	126
5.3 Sensitivities to physical parameterization schemes and the ensemble prediction .....	131
<b>6 Summary and conclusions</b>	<b>140</b>
6.1 Spatiotemporal variations of precipitation in Bangladesh revealed by nationwide rain gauge data .....	140
6.2 Evaluation and CSEOF analysis of IMERG data for precipitation studies in Bangladesh and surrounding regions .....	145
6.3 Development of a physically based raindrop-cloud droplet accretion parameterization and its evaluation through cloud and precipitation simulations .....	142
6.4 Dynamical, thermodynamical, and cloud microphysical processes associated with extremely heavy precipitation in the Meghalaya Plateau region.....	145
<b>References</b>	<b>149</b>

<b>초 록</b>	<b>164</b>
<b>Acknowledgements</b>	<b>168</b>

## List of figures

2.1	Terrain height (color shading) and locations of 35 meteorological stations (closed circles). Three regions are indicated: northern (N) region, southwestern (SW) region, and southeastern (SE) region. HM, MP, and AM represent the Himalaya Mountains, the Meghalaya Plateau, and the Arakan Mountains, respectively. ....	17
2.2	Temporal variation of annual precipitation amount averaged over Bangladesh. ....	18
2.3	Monthly precipitation amounts averaged over Bangladesh and the period 2003–2016. ....	20
2.4	Spatial distributions of (a) annual, (b) pre-monsoon season, and (c) monsoon season precipitation amounts averaged over the period 2003–2016. ....	21
2.5	Fields of water vapor flux vector and its magnitude (color shading) at 900-hPa level averaged over the period 2003–2016 in the (a) pre-monsoon season and (b) monsoon season. (c) and (d) are the same as (a) and (b), respectively, except for the divergence of water vapor flux. ....	23
2.6	Diurnal variations of 3-h accumulated precipitation amount averaged over stations in the (a) northern (N), (c) southwestern (SW), and (e) southeastern (SE) regions in the pre-monsoon season and those in the (b) N, (d) SW, and (f) SE regions in the monsoon season. Note that the	

	y-axis limits in the plots of the pre-monsoon and monsoon seasons are different.....	27
2.7	Vertical profiles of equivalent potential temperature at 00, 06, 12, and 18 LST averaged over stations in the (a) northern (N), (c) southwestern (SW), and (e) southeastern (SE) regions in the pre-monsoon season and those in the (b) N, (d) SW, and (f) SE regions in the monsoon season. ....	31
2.8	Fields of horizontal wind vector and the divergence of water vapor flux (color shading) at 950 hPa level averaged over the period 2003–2016: (a) 00 LST, (c) 06 LST, (e) 12 LST, and (g) 18 LST in the pre-monsoon season and (b) 00 LST, (d) 06 LST, (f) 12 LST, and (h) 18 LST in the monsoon season. ....	35
3.1	Topographic map of Bangladesh and surrounding regions with the locations of 35 rain gauge stations (black circles) .....	40
3.2	Density scatter plot between 3-hourly precipitation amounts from the IMERG data and those from rain gauge data in the (a) pre-monsoon, (b) monsoon, (c) post-monsoon, and (d) winter seasons .....	45
3.3	Seasonal variations of monthly-mean precipitation amount averaged over the period 2015–2019 for the IMERG data and rain gauge data .....	47
3.4	Diurnal variations of 3-hourly precipitation amount in the (a) pre-monsoon, (b) monsoon, (c) post-monsoon, and (d) winter seasons averaged over the period 2015–2019 for the IMERG data and rain gauge data .....	49



3.5	Spatial distributions of monthly precipitation amounts in the pre-monsoon (first row), monsoon (second row), post-monsoon (third row), and winter (fourth row) seasons averaged over the period 2015–2019 for the IMERG data (first column), rain gauge data (second column), their differences (IMERG – rain gauge) (third column) and their relative differences (fourth column) .....	51
3.6	3-hourly CSLVs for the first (two leftmost columns) and second (two rightmost columns) CSEOF modes of precipitation amount anomaly in the pre-monsoon season.....	53
3.7	PC time series for the (a) first and (b) second CSEOF modes of precipitation amount anomaly in the pre-monsoon season.....	54
3.8	Regressed 3-hourly CSLVs of 900-hPa water vapor flux anomaly ( $\text{g kg}^{-1} \text{ m s}^{-1}$ ) associated with the first (two leftmost columns) and second (two rightmost columns) modes of precipitation amount anomaly in the pre-monsoon season.....	57
3.9	As in Fig. 3.6, but for precipitation amount anomaly in the monsoon season.....	58
3.10	As in Fig. 3.7, but for precipitation amount anomaly in the monsoon season.....	60
3.11	As in Fig. 3.8, but for in the monsoon season.....	62

4.1	Terminal velocities of (a) cloud droplets (Lee and Baik 2017) and (b) raindrops. The star symbols indicate the terminal velocities from Beard (1976), and the solid lines are the fitted equations. ....	68
4.2	(a) The reference collision efficiency between raindrops and cloud droplets which is a combination of the collision efficiencies of Pinsky et al. (2001) and Beard and Grover (1974). (b) The fitted collision efficiency and (c) the fitted collision efficiency minus the reference collision efficiency.....	71
4.3	Composite of thermodynamic soundings at Dhaka radiosonde station in June 2014. The thick red and blue solid lines indicate the temperature and dew point temperature, respectively, and the thick black dashed line indicates the temperature of air parcel lifted moist-adiabatically from the level of free convection.....	77
4.4	Time series of domain-averaged (a) accumulated surface precipitation amount and (b) surface precipitation rate in the idealized simulations with the new and original accretion parameterizations.....	79
4.5	Time- and domain-averaged vertical profiles of (a) hydrometeor mixing ratios and mass-weighted mean radii of (b) raindrops and (c) cloud droplets in the idealized simulations with the new (solid lines) and original (dashed lines) parameterizations. ....	80
4.6	Time series of domain-averaged (a) accretion rate, (b) autoconversion rate, (c) the sum of accretion and autoconversion rates, and (d) the ratio	

	between accretion and autoconversion rates in the idealized simulations with the new and original parameterizations. ....	83
4.7	Time series of domain-averaged (a) liquid water path and (b) ice water path in the idealized simulations with the new and original parameterizations. ....	85
4.8	Time- and domain-averaged vertical profiles of (a) the heating rates due to condensation/evaporation, deposition/sublimation, riming, and freezing/melting in the idealized simulation with the new parameterization and (b) the differences in the heating rates between the new and original parameterizations. (c) Time- and domain-averaged vertical profiles of updraft velocity ( $w > 0.1 \text{ m s}^{-1}$ ) in the idealized simulations with the new and original parameterizations. ....	87
4.9	Normalized accretion rates as a function of internal time scale $\tau$ in the idealized simulations with the (a) new and (b) original parameterizations. The red dots correspond to the idealized simulation results for $t \leq 40 \text{ min}$ , and the black dots correspond to those for $t > 40 \text{ min}$ . ....	89
4.10	Three nested model domains for the real-case simulations and terrain height. ....	91
4.11	Spatial distributions of 7-day accumulated precipitation amount simulated with (a) NP and (b) OP and (c) observed at meteorological stations. The simulation results are interpolated to the locations of the meteorological stations in (a) and (b). ....	93

4.12	Brier scores calculated using the simulated and observed 7-day accumulated precipitation amounts at the location of each meteorological station. ....	94
4.13	As in Fig. 4.5, but for the real-case simulations. ....	95
4.14	As in Fig. 4.6, but for the real-case simulations. ....	97
4.15	As in Fig. 4.7, but for the real-case simulations. ....	98
4.16	Time- and domain-averaged vertical profiles of (a) the heating rates due to condensation/evaporation, deposition/sublimation, riming, and freezing/melting in the real-case simulation with the new parameterization and (b) the differences in the heating rates between the new and original parameterizations. ....	100
5.1	900-hPa equivalent potential temperature (shaded), horizontal wind vector (arrows), and geopotential height (m, black solid lines) fields at (a) 1500 LST 18 and (b) 0300 LST 19 from the ERA5 reanalysis data. Subfigures (c) and (d) are analogous to (a) and (b) but at 500 hPa. The green dot denotes Cherrapunji. ....	102
5.2	Four nested domains in the CNTL and noMP simulations and one additional domain in the HRES simulation with terrain height (m, shaded). d1, d2, d3, and d4 indicate domains 1, 2, 3, and 4, respectively. Domain 5 of the HRES simulation is indicated by red box. ....	104
5.3	Terrain height in the innermost domain (domain 4) of the (a) CNTL and (b) noMP simulations. Black, blue, and red boxes represent the upwind, upslope, and downwind regions, respectively. Black hollow circle and	

	triangle indicate Mawsynram (25.30°N, 91.58°E) and Cherrapunji (25.25°N, 91.73°E), respectively. Red line (Line A) represents the reference line used for analysis.....	105
5.4	24-hr accumulated precipitation amount from the rain gauge observation (circles) and the CNTL simulation (shaded), and (b) their difference. (c) Scatter plot of the rain gauge observation and CNTL simulation for the 24-hr accumulated precipitation amount. ....	108
5.5	Time series of area-averaged precipitation rate for the (a) upwind, (b) upslope, and (c) downwind regions in the CNTL (solid) and noMP (dashed) simulations. ....	109
5.6	9-hr accumulated precipitation amount (shaded in color) and 900-hPa level wind vector (arrows) fields with terrain height (shaded in black) during (a) 1500 LST 18–0000 LST 19 and (b) 0000–0900 LST 19 August 2015. ....	111
5.7	Vertical profiles of the area-averaged (a) wind speed component along the direction of Line A in Figure 4.3a and (b) equivalent potential temperature in the upwind region. ....	113
5.8	Time series of (a) horizontal wind speed and (b) water vapor flux at 900 hPa along the direction of Line A averaged over the upwind region. ....	115
5.9	Vertical cross-sections of water vapor flux (shaded) and wind vectors along Line A at 1800 LST 18 and 0600 LST 19 August 2015. ....	116
5.10	Vertical cross-sections of vertical velocity along Line A at (a) 2100 LST 18, (b) 0200 LST 19, and (c) 0600 LST 19 August 2015. ....	118

5.11	Time series of LWP (top row) and IWP (bottom row) averaged over the upwind (first column), upslope (second column) and downwind (third column) regions in the CNTL (solid) and noMP (dashed) simulations. ....	120
5.12	Vertical profiles of hydrometeors averaged over the upslope region at 2100 LST 18 (top row) and 0600 LST 19 (bottom row) August 2015 in the CNTL (first column) and noMP (second column) simulations and their differences (third column). ....	121
5.13	Vertical profiles of microphysical conversion rates related to rainwater production (AU: autoconversion, AC: accretion, ML: melting) averaged over the upslope region at 2100 LST 18 (top row) and 0600 LST 19 (bottom row) August 2015 in the CNTL (first column) and noMP (second column) simulations and their differences (third column). ....	122
5.14	Vertical cross-sections of the liquid and ice hydrometeor mixing ratios at 2100 LST 18 (top row), 0200 LST 19 (middle row), and 0600 LST 19 (bottom row) August 2015 in the CNTL (left column) and noMP (right column) simulations.....	125
5.15	(a) Terrain height in the HRES simulation and (b) the difference between the HRES and CNTL simulations. (c) 24-hr accumulated precipitation amount in the HRES simulation and (d) the difference between the HRES and CNTL simulations. Terrain height is contoured at 400-m intervals in (b), (c), and (d). ....	127

5.16	Horizontal distributions of vertical velocity at $z = 3$ km averaged over P2 (0000–0900 LST 19) in the (a) HRES and (b) CNTL simulations and (c) their difference. Terrain height is contoured at 400 m intervals. ....	128
5.17	Contoured frequency by altitude diagrams (CFADs) of vertical velocity in the (a) HRES and (b) CNTL simulations and (c) their difference. Bins with HRES values only are indicated by grey color in (c). ....	129
5.18	Spatial distribution of 24-hr accumulated precipitation amount in the simulations with different microphysics schemes: (a) CNTL, (b) MP_Morrison, (c) MP_MY, (d) MP_NSSL, (e) MP_P3, (f) MP_WDM6, (g) is the ensemble average (MP_EN), and (h) MP_ITE, focusing on the southern slope of MP .....	134
5.19	Same as Fig. 5.18 but for simulations with different PBL schemes: (a) CNTL, (b) PBL_ACM2, (c) PBL_MYJ, and (d) PBL_UW. (e) is the ensemble average (PBL_EN). ....	136
5.20	Same as Fig. 5.18 but for the simulations with different radiation schemes: (a) CNTL, (b) RAD_CAM, and (c) RAD_RRTMG. (e) is the ensemble average (RAD_EN). ....	137
5.21	Same as Fig. 5.18 but for ensemble average of all 11 simulations .....	139
6.1	The schematic diagram for processes associated with extremely heavy precipitation in MP during (a) P1 and (b) P2 .....	147

## List of tables

2.1	Diurnal variability of precipitation $D$ in each region and each season. ....	29
-----	---	----



# 1 Introduction

## 1.1 Characteristics of observed precipitation in Bangladesh

Bangladesh is a South Asian deltaic country with three main rivers, the Ganges, the Brahmaputra, and the Meghna, running through it. Its topography is mostly flat except for some portions of northeastern and southeastern regions of the country where the elevation is higher than 100 m above the sea level. Bangladesh is under the strong influence of the South Asian monsoon and experiences frequent severe flood events which cause serious losses of lives and properties.

Bangladesh is a country with much rains. The Mawsynram region of Meghalaya state in northeast India is one of the rainiest places in the world. The northeastern region of Bangladesh, which is adjacent to the Meghalaya Plateau, and the southeastern coastal region of the country adjacent to the Chittagong Hill Tracts receives considerable amounts of rain. The rainy season in and around Bangladesh can be divided into pre-monsoon season (MAM: March, April, and May), monsoon season (JJAS: June, July, August, and September), and post-monsoon season (ON: October and November) (Islam and Uyeda 2007). Using the rain gauge data from 1998 to 2002, Islam and Uyeda (2007) showed that average daily precipitation rates are 5.30, 15.14, and 4.56 mm/day in the pre-monsoon, monsoon, and post-monsoon seasons, respectively.

Although the precipitation amount is much smaller in the pre-monsoon season than in the monsoon season, investigations of pre-monsoon precipitating systems are important because they result in the first precipitation after the end of the dry winter season (December to February) and they are convective (Romatschke and Houze 2011). In the pre-monsoon season, especially in April, the high thermal instability and vertical

wind shear are present over Bangladesh (Yamane and Hayashi 2006), which favors the generation of precipitating convective systems. In the northeastern region of Bangladesh, precipitating systems in the pre-monsoon season exhibit an extremely convective nature (Romatschke et al. 2010). In the regions which include the Meghalaya Plateau region, pre-monsoon convection seems to be more sensitive to synoptic forcing than monsoon convection (Romatschke and Houze 2011).

In the monsoon season, on the other hand, strong moist low-level southwesterly winds prevail over the Bay of Bengal, which is related to the thermal contrast between South Asia and the Indian Ocean (Li and Yanai 1996). In Bangladesh, the summer monsoon begins earliest in the extreme southeastern part of the country with a mean start date of 2 June, and it begins latest in the extreme northwestern part of the country with a mean start date of 15 June (Ahmed and Karmakar 1993). The Meghalaya Plateau plays significant roles in producing heavy precipitation in the northeastern region of the country (Sato 2013). It is known that monsoon intraseasonal oscillations modulate precipitating systems in and around Bangladesh (Ohsawa et al. 2000; Goswami and Mohan 2001). An analysis of precipitation in Bangladesh during the 1995 summer monsoon season by Ohsawa et al. (2000) shows that the north-south oscillation of the monsoon trough dominates the precipitation.

The diurnal variation of precipitation is an important ingredient of the water cycle at any location (Ohsawa et al. 2001). Many observational studies have been conducted to examine the diurnal variation of precipitation in India and some part of Bangladesh which shares a border with India (Prasad 1970; Ohsawa et al. 2001; Terao et al. 2006). Prasad (1970) showed that the precipitation maximum at Cherrapunji located in the Meghalaya

Plateau occurs in the late night to early morning. He conjectured that the low-level convergence produced by nocturnal katabatic winds may be responsible for the precipitation maximum. Ohsawa et al. (2001) found the late night to early morning precipitation maximum at stations on the windward side of the Meghalaya Plateau. Through a case study using a mesoscale numerical model, Kataoka and Satomura (2005) showed that the Meghalaya Plateau or the dammed deep cold air mass in the concave area northeast of Bangladesh acts to raise air with high equivalent potential temperature to the level of free convection and trigger strong convective systems in the nighttime, thus leading to the late night to early morning precipitation maximum. Using the rain gauge and rawinsonde data in 2000, Terao et al. (2006) showed that the nocturnal low-level jet is one of the causes for the late night to early morning precipitation maximum in the northeastern region of the country through the intensified wind which blows against the southern side of the Meghalaya Plateau.

Many studies of precipitation in Bangladesh and surrounding areas have used satellite data (e.g., Islam and Uyeda 2008). Satellite-estimated precipitation data have fine spatial resolutions but contain some biases and uncertainties (Dai et al. 2007; Islam and Uyeda 2008; Zhou et al. 2008; Yuan et al. 2012). Islam and Uyeda (2008) showed that the Tropical Rainfall Measuring Mission (TRMM) data overestimate the pre-monsoon precipitation and underestimate the monsoon precipitation in Bangladesh. Tarek et al. (2017) showed that in Bangladesh, TRMM data is well matched with rain gauge data for average precipitation values on an annual basis, but the deviation is significant for daily peak precipitation values. A recent study of comparing six satellite-retrieved precipitation products with rain gauge data in Bangladesh (Islam 2018) reveals that the satellite-

retrieved precipitation products are good in detecting the precipitation occurrence but not so good in estimating the precipitation amount. It seems that the precipitation in Bangladesh could be better characterized using nationwide rain gauge data rather than satellite data. It is noted that studies of the diurnal variation of precipitation in Bangladesh have been performed focusing on the northeastern region of the country (or focusing on the region of the Meghalaya Plateau and its surrounding) or using short-term data (e.g., Islam et al. 2005). Since the diurnal variation of precipitation can vary depending on regions (Yang and Slingo 2001), diurnal variations in other regions of Bangladesh deserve an investigation with long-term precipitation data. The characteristics of the diurnal variation of precipitation in the monsoon season can be to some extent different from those in the pre-monsoon season. This also deserves an investigation.

Bangladesh is a densely populated country where people mostly depend on agriculture. Moreover, the country is very vulnerable to flooding. A long-term precipitation analysis study using data at 12 stations in Bangladesh (Endo et al. 2015) shows increasing trends in the annual precipitation amount and the number of wet days. Bari et al. (2017) found an increasing trend in precipitation seasonality at some locations of northern Bangladesh. A recent study by Basher et al. (2018) reveals that all the indices of precipitation extremes in northeast Bangladesh are in a decreasing trend in both the pre-monsoon and monsoon seasons, implying that the region might suffer from water stress in the future if the decreasing trend continues. For better weather forecasting, climate change assessment, agricultural planning, water resource management, and so on,

it is necessary, as a first step, to document a reliable climatology of precipitation in it is Bangladesh.

In this study, spatial and temporal variations of precipitation in Bangladesh, particularly focusing on its diurnal variation, are examined using 14-year nationwide rain gauge data and reanalysis data in chapter 2. In subsection 2.1, the data used in this study are described. In subsection 2.2, the results are presented and discussed. In chapter 6.1, summary and conclusions are given.

## **1.2 Applicability of IMERG data to precipitation studies in and around Bangladesh**

Bangladesh is located in South Asia and is the largest deltaic country in the world. Its location and geographical features make the country one of the heaviest precipitated regions in the world. Bangladesh receives 17%, 73%, and 9% of annual precipitation amount in the pre-monsoon (March to May), monsoon (June to September), and post-monsoon (October to November) seasons, respectively (Chapter 2). There are large variations of annual precipitation amount across the country, with maximum precipitation occurring in the northeastern region and the southeastern coastal region and minimum precipitation occurring in the western region (Tarek et al. 2017). Recent studies report a significant decreasing trend of precipitation in the western region of Bangladesh (Chowdhury et al. 2019) and frequent precipitation extremes in the northeastern region of Bangladesh (Mohsenipour et al. 2020), making Bangladesh more vulnerable to natural disasters.

The precipitation characteristics in Bangladesh and surrounding regions have been examined using rain gauge data. Using long-term daily precipitation data from 19 rain gauge stations, Ahmed and Kim (2003) showed that the average number of rainy days in the monsoon season is 60 in the western region and 100 in the northeastern region. Shahid and Khairulmaini (2009) found a gradual increase of annual precipitation amount across the country from west to east (7 mm km<sup>-1</sup>). The monsoonal precipitation in Bangladesh exhibits a clear diurnal variation where the precipitation maximum occurs in the late night to early morning in the northern and southeastern regions (Chapter 2). Precipitation in Bangladesh and the Meghalaya Plateau region in the monsoon season has the submonthly scale (7–25 days) intra-seasonal oscillation (ISO) (Murata et al. 2008; Fujinami et al. 2011). Satellite-based precipitation products have been also used to examine the precipitation characteristics in Bangladesh and surrounding regions. Islam and Uyeda (2007) showed that the precipitation amount averaged over the period from March to November in Bangladesh from the Tropical Rainfall Measuring Mission (TRMM) satellite precipitation product is about 97% of that obtained from the rain gauge observation. Using the TRMM data for 13 years (1998–2010), Tarek et al. (2017) showed that the TRMM data reproduce the spatial and temporal distributions of precipitation and are reliable for use in hydrological analyses of watersheds in Bangladesh.

Reliable precipitation data are a precondition for precipitation studies in and around Bangladesh. Rain gauge data have been considered to be most consistent and precise (He et al. 2011). However, the sparse distribution of rain gauge stations provides incomplete spatial variations of precipitation (Kidd et al. 2017). Nowadays, satellite-based precipitation products are widely used as an alternative due to their higher spatial

and temporal resolutions. Among satellite-based precipitation products, the Integrated Multi-satellitE Retrievals for Global Precipitation Measurement (IMERG) data have fine spatial ( $\sim 0.1^\circ$ ) and temporal ( $\sim 30$  min) resolutions (Huffman et al. 2020). Tan et al. (2019) showed that the IMERG data adequately reproduce the diurnal variation of precipitation in Bangladesh. However, satellite-based precipitation products tend to show underestimation (overestimation) in the wet (dry) region and random errors due to the limitations in the precipitation retrieval algorithms and sampling frequency (Islam and Uyeda, 2007; Nair et al. 2009). Therefore, it is necessary to evaluate satellite-based precipitation products with in situ observation before using them for precipitation analysis.

Various statistical methods have been employed to investigate precipitation in and around Bangladesh. Chowdhury et al. (2019) calibrated the Decadal and Hierarchical Markov Chain (DHMC) model with the precipitation data from rain gauge stations in Bangladesh and evaluated its performance to reproduce the observed temporal variabilities of precipitation in various temporal scales. Mohsenipour et al. (2020) used monthly precipitation data at each station as an input in the quantile regression model (Koenker and Bassett 1978) and examined the long-term changes in distributions of monsoonal precipitation in Bangladesh. Using monthly precipitation data at 14 stations from 1901 to 1977 in Bangladesh and the empirical orthogonal function (EOF) analysis method, Kripalani et al. (1996) found that the first and second EOF modes are associated with the inter-annual variation of monsoonal precipitation and the onset or withdrawal phase of monsoonal precipitation, respectively.

The EOF analysis method has been widely used in meteorology and climatology but has some limitations (Kim 2017). The EOF analysis method assumes that statistics (e.g., mean, variance, covariance) of variables are stationary, that is, do not change with time. In fact, however, statistics of many meteorological variables are non-stationary, changing with time. A non-stationary physical process changing with time cannot be represented by an individual EOF mode which is a single spatial pattern with a time-varying amplitude. The cyclostationary EOF (CSEOF) analysis method decomposes original data into multiple time-varying spatial patterns which are periodic in time, and each time-varying spatial pattern is regarded as a periodic physical process. This method assumes that statistics of variables are a periodic function of time, which relaxes the assumption of the EOF analysis method. The CSEOF analysis method has been successfully used in analyses of climate data (Kullgren and Kim 2006; Kim et al. 2010; Roh et al. 2012; Kim and Kim 2020).

In this study, we evaluate the IMERG data against rain gauge observation to examine its usability in studies of precipitation in Bangladesh and surrounding regions in chapter 3. Then, we analyse the IMERG data using the CSEOF analysis method, focussing on the diurnal variation of precipitation in Bangladesh and surrounding regions. Subsection 3.1 describes the IMERG data and CSEOF analysis method. Subsection 3.3 presents the results and discussion. In chapter 6.2, summary and conclusions are given.

### **1.3 Raindrop-cloud droplet accretion parameterization in bulk microphysics schemes**

Cloud-resolving models which represent moist convective processes explicitly



have been widely used for weather research and prediction. Cloud-resolving models adopt cloud microphysics schemes to represent grid-scale cloud and precipitation processes. Cloud microphysics schemes are categorized into bin microphysics schemes and bulk microphysics schemes. Because of simpler representations of microphysical processes and much lower computational cost, bulk microphysics schemes are exclusively employed in operational numerical weather prediction (NWP) models. Predictions using bulk microphysics schemes contain some degree of uncertainty involved with assumptions and limited observations used to represent cloud particle size distributions and parameterize cloud microphysical processes (Johnson et al. 2015). To better understand moist convection through numerical simulations and more accurately predict weather, developments of physically based bulk microphysics schemes need to be continued (Naumann and Seifert 2016; Paukert et al. 2019).

Kessler (1969) proposed one of the first bulk microphysics schemes for warm clouds. In this scheme, liquid-phase cloud particles are divided into cloud droplets and raindrops, and the rainwater is produced by the autoconversion of cloud droplets into raindrops and the accretion of cloud droplets by raindrops. The importance of the autoconversion and accretion processes in warm clouds has been well investigated through numerical simulations of cumulus and stratocumulus clouds (e.g., Wood 2005; Morrison and Grabowski 2007; Michibata and Takemura 2015). The autoconversion process plays an important role in the initiation of precipitation, and the accretion process mainly contributes to the precipitation intensity (Wu et al. 2018).

For the accretion process, Kessler (1969) parameterized the accretion rate based on a continuous collection concept, which is expressed in a power-law equation and is a

function of cloud water and rainwater mixing ratios. After the Kessler's accretion parameterization, various forms of accretion parameterizations have been developed. Tripoli and Cotton (1980) derived the accretion rate in a simple form using the continuous collection equation. Using the results of a large-eddy simulation model with a bin microphysics scheme, Khairoutdinov and Kogan (2000) proposed a simple fitting equation for the accretion rate. Seifert and Beheng (2001) proposed an analytic form of the accretion rate derived from the stochastic collection equation (SCE) by simplifying it with an approximate collection kernel of Long (1974) and corrected using the numerical solution of the full SCE where more accurate collection kernel than Long's is considered. The SCE gives the time rate of change in the expected value of drop number concentration for a given drop size using a collection kernel. Note that possible fluctuations in drop number concentration around its expected value are not considered in the SCE (Dziekan and Pawlowska 2017).

Wood (2005) evaluated the widely used accretion parameterizations in the literature through comparison with the numerical solution of the SCE for drizzling stratiform clouds. The accretion parameterizations showed relatively good performance compared to the autoconversion parameterizations, but still exhibited non-negligible biases. The biases may result from the simplicity of the accretion parameterizations. The accretion parameterizations evaluated depend only on cloud water and rainwater mass contents and the functional forms are too simple, making it difficult to represent the variation of the accretion rate with various size distributions of cloud droplets and raindrops; the collection efficiency that varies with the sizes of colliding particles is not considered. Furthermore, the parameterization based on the results of bin microphysics

model simulations for one environment (e.g., Khairoutdinov and Kogan 2000) may yield deviations in simulations for another environment (Morrison and Grabowski 2007).

The best way to minimize the deviation of the parameterized accretion rate from the numerical solution of the SCE would be to derive the accretion rate analytically from the SCE and avoid unnecessary assumptions. Recently, Lee and Baik (2017; LB17 hereafter) proposed an elaborate autoconversion parameterization derived analytically from the SCE. In their autoconversion parameterization, the collection efficiency between cloud droplets, which has been often assumed to be a constant, is expressed as a function of individual sizes of colliding cloud droplets. The developed parameterization predicted the autoconversion-related quantities that are closest to those predicted by a bin-based direct SCE solver, compared to other autoconversion parameterizations. As an extension of the autoconversion parameterization of LB17, a similar approach can be applied to the parameterization of the accretion process. An accretion parameterization derived analytically based on the SCE is expected to yield a better representation of the accretion process in reality compared to accretion parameterizations based on the continuous collection equation or based on SCEs that are simplified to some extent, which is the motivation of this study. This new parameterization takes into consideration the collection efficiency of individual raindrop–cloud droplet pairs which is not considered in the simpler previous accretion parameterizations. The new parameterization also considers the contribution of the cloud droplets to the geometric sweep-out volume in the SCE often neglected in the simpler parameterizations.

In this study, a parameterization of the accretion of cloud water by rainwater for use in weather and climate models with bulk microphysics schemes is derived

analytically based on the SCE and evaluated in chapter 4. The drop size-dependent collection efficiency obtained using a particle trajectory model (Pinsky et al. 2001) is used for the parameterization. The derivation of a new accretion parameterization is given in subsection 4.1. In subsection 4.2, the new accretion parameterization is evaluated against a conventional accretion parameterization through idealized and real-case simulations using a cloud-resolving model. A summary and conclusions are presented in chapter 6.3.

## **1.4 Extreme monsoonal precipitation in the Meghalaya Plateau region**

The Meghalaya Plateau (MP), located in Northeast India and bordered to the south by Bangladesh, is one of the rainiest regions in the world. MP is oriented in the east–west direction, and its southern slope is made up of undulating hills and deep valleys responsible for the unique topographic features of the plateau. When the humid monsoonal wind blows from the Bay of Bengal, MP acts as a first orographic barrier in its way to the Himalayas. Cherrapunji, a town located atop a steep cliff in southern MP, receives an average annual precipitation of ~12000 mm (Murata et al. 2008). Most of the heavy precipitation events in MP occur during the active spells of the South Asian summer monsoon which has submonthly-scale intraseasonal oscillations (Fujinami et al. 2011; Murata et al. 2017). The rainwater runs off via streams and the Surma River to the lowland area of Sylhet district of Bangladesh and generates flash floods that cause considerable loss of life and property in this region (Ohsawa et al. 2001; Habib et al. 2019).

The heavy rainfall in MP has been examined in many observational studies. Using daily rainfall data from 15 stations during 32 years (1975–2006), Goswami et al. (2010) showed that the heavy rainfall events ( $> 150 \text{ mm d}^{-1}$ ) in Northeast India mainly occur during the peak monsoon season (June–August). By examining the lengths and phases of rainy spells, it was shown that the most extreme events are associated with either mesoscale, synoptic, or large-scale systems rather than isolated thunderstorms. Accordingly, the observed rainfall in MP during the monsoon season shows the quasi-biweekly intraseasonal (7–25 days) variability which is in the temporal range of the aforementioned systems (Murata et al. 2008; Sato 2013; Fujinami et al. 2017). Murata et al. (2017) showed that when the anomalous anticyclonic circulation at 850 hPa propagating westward from the South China Sea and western North Pacific stays over the northern part of the Bay of Bengal and central India, the westerlies are predominant at the north of the anomalous anticyclonic circulation. These westerlies enhance the moisture flux from the Bay of Bengal and the moisture convergence at Northeast India. The combination of this synoptic condition and orographic lifting produces the heavy rainfall over MP. In northeastern Bangladesh located in the vicinity of MP, the maximum rainfall is usually observed in the late night to early morning (Ohsawa et al. 2001; Islam et al. 2005; Terao et al. 2006). Using 6-hourly rawinsonde data, Terao et al. (2006) showed that the meridional wind speed is maximum at 0000 LST and the wind direction changes in the clockwise direction with height, indicating the existence of a nocturnal low-level jet (LLJ). They suggested that the nocturnal LLJ is a possible cause for the rainfall peak in the late night to early morning.

Compared to the observational studies, only a few numerical studies have been conducted to understand the mechanisms and characteristics of precipitation in MP. Kataoka and Satomura (2005) showed that the diurnal variation of precipitation, especially the maximum in the late night to early morning, is closely associated with the deep convective activity index derived from 3-hourly satellite data and that severe precipitation systems are triggered when strong southwesterlies with high equivalent potential temperature climb MP or a thick cold pool. Sato (2013) showed that the sufficient intensity and proper direction (southerly/southwesterly) of LLJ are needed to initiate orographic convection.

These previous numerical studies mainly focused on dynamical and thermodynamical processes. Orr et al. (2017) demonstrated the importance of cloud microphysical processes in the monsoonal precipitation in the Himalayan region, located nearby MP, through several numerical simulations using different cloud microphysics schemes. For the precipitation in MP region, however, cloud microphysical processes and their interactions with dynamical and thermodynamical processes have not been investigated in depth. This study aims to examine the cloud microphysical, dynamical, and thermodynamical processes of extremely heavy precipitation in MP and their interactions. This study also aims to examine the effects of the complex topography within the plateau through numerical simulations using very fine horizontal resolutions. The horizontal resolutions used in previous numerical studies (2–3.6 km) may not be sufficient to resolve the complex topography such as steep slopes and deep narrow valleys. Furthermore, simulating and predicting extreme precipitation in the MP region is challenging because of the complex topography and its interactions with various physical

processes. Therefore, sensitivities of simulated precipitation to various physical parameterization schemes deserve an investigation in the MP region.

The chapter 5 is organized as follows. The case description and the model setup are presented in subsection 5.1. Subsection 5.2 is dedicated to the simulation results and discussion. Sensitivities to physical parameterization schemes and the ensemble prediction are described in subsection 5.3. In chapter 6.4, summary and conclusions are given.

## **2 Spatiotemporal variations of precipitation in Bangladesh revealed by nationwide rain gauge data**

### **2.1 Data**

The Bangladesh Meteorological Department (BMD) has 35 meteorological stations which are distributed all over the country (Fig. 2.1). For this study, the BMD 3-h accumulated precipitation amount data collected from 2003 to 2016 are used. Exceptions are at Cox's Bazar (21.43°N, 91.93°E), Chittagong (22.27°N, 91.82°E), and Hatiya (22.43°N, 91.10°E) stations located in the southeastern coastal region whose data are available from 2004, 2004, and 2008, respectively. The 3-h accumulated precipitation amount data for the 14-year period are used to document and analyze diurnal, monthly, and yearly precipitation climatology in the country.

The ERA5 reanalysis data with  $0.25^\circ \times 0.25^\circ$  horizontal grid resolution (Hersbach and Dee 2016) are used to examine large-scale thermodynamic and dynamic characteristics associated with the features of precipitation in Bangladesh. For this, fields of velocity, water vapor flux and its divergence and vertical profiles of equivalent potential temperature are analyzed.

### **2.2 Results and discussion**

#### **2.2.1 Yearly and monthly variation of precipitation**

The variation of annual precipitation amount from 2003 to 2016 is examined (Fig. 2.2). The average annual precipitation amount in Bangladesh is 2263 mm, with its



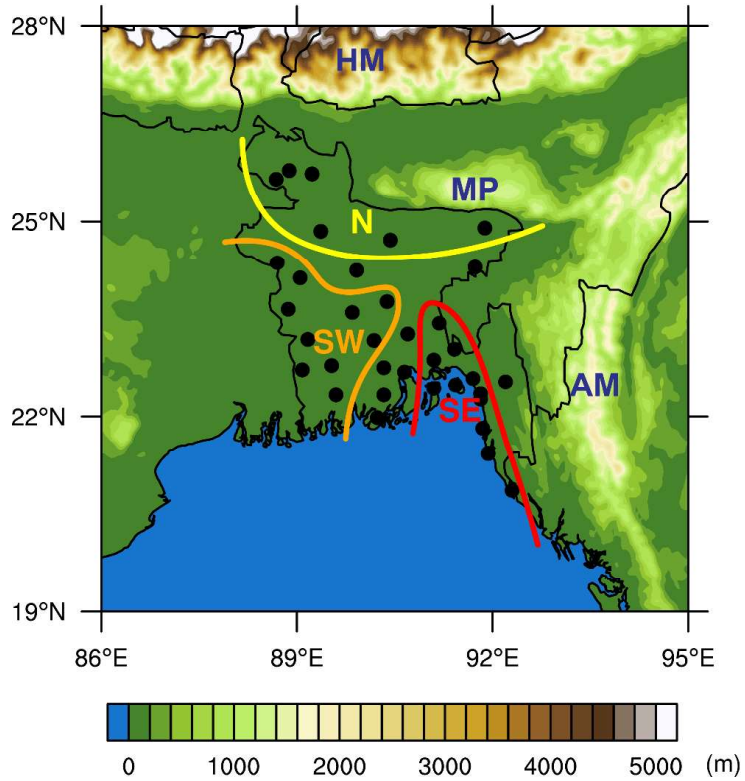


Figure 2.1 Terrain height (color shading) and locations of 35 meteorological stations (closed circles). Three regions are indicated: northern (N) region, southwestern (SW) region, and southeastern (SE) region. HM, MP, and AM represent the Himalaya Mountains, the Meghalaya Plateau, and the Arakan Mountains, respectively.

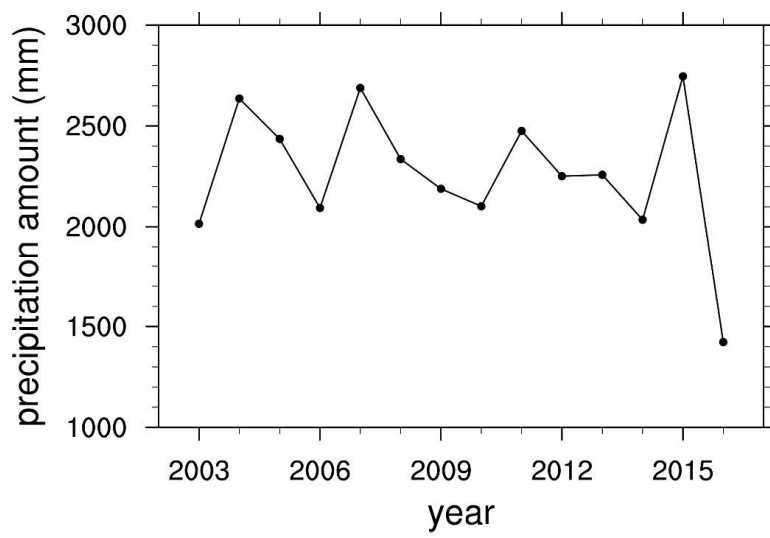


Figure 2.2 Temporal variation of annual precipitation amount averaged over Bangladesh.

standard deviation of 341 mm. The deviation of the annual precipitation amount from its average value (2263 mm) varies from 425 mm in 2015 to –840 mm in 2016. The interannual variability with a 3- or 4-year oscillation period is clearly seen from 2003 to 2014. In 2016, the precipitation amount is distinctly smaller compared with the other 13 years.

The Indian Ocean Dipole (IOD) is regarded as a large-scale phenomenon that is partially responsible for the interannual variability of precipitation amount in Bangladesh, especially for the western region (Ahmed et al. 2017). Fujinami et al. (2011), however, suggested that the monsoon precipitation, which occupies a large portion of annual precipitation, is modulated by the submonthly-scale intraseasonal oscillation which belongs to internal variability of monsoon. Causes for the interannual variability shown in Fig. 2.2 are not clear, but it appears to be associated with large-scale phenomena such as IOD, intraseasonal oscillation of monsoon, and so on. Studies on this issue are needed.

The monthly precipitation amount (Fig. 2.3) increases with time, peaks in July, and then decreases. July is the rainiest month (488 mm). 17% and 73% of the annual precipitation amount are observed in the pre-monsoon season (MAM) and monsoon season (JJAS), respectively. The precipitation amount in the monsoon season is more than four times larger than that in the pre-monsoon season. The contribution of the post-monsoon season (ON) to the annual precipitation amount is 8.7%. December to February is characterized as a dry season.

The annual precipitation amount is considerably large in the southeastern coastal region of Bangladesh and the region close to the Meghalaya Plateau (Fig. 2.4a). The rainiest place in Bangladesh is Teknaf (20.87°N, 92.30°E) with an annual precipitation

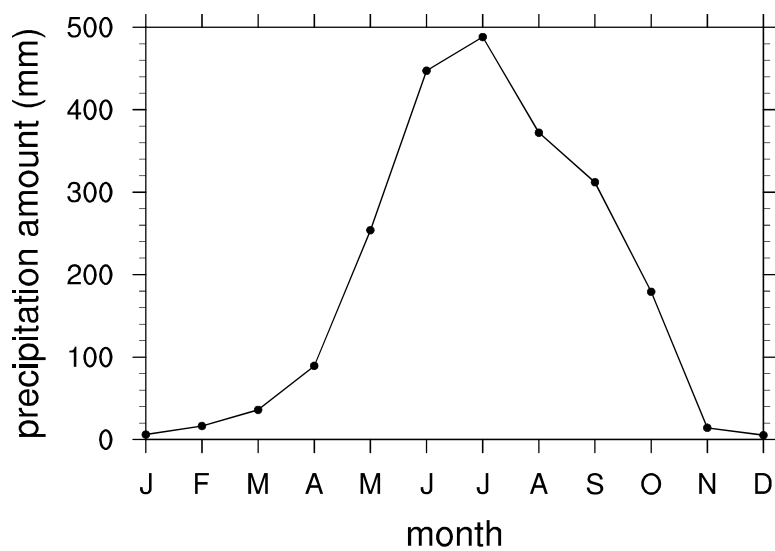


Figure 2.3 Monthly precipitation amounts averaged over Bangladesh and the period 2003–2016.

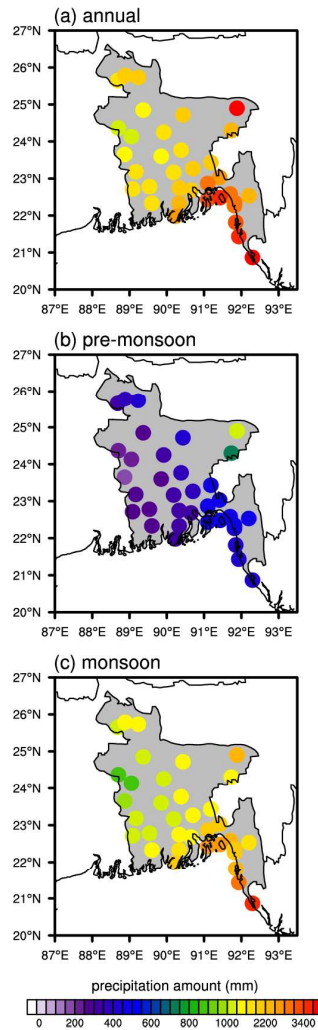


Figure 2.4 Spatial distributions of (a) annual, (b) pre-monsoon season, and (c) monsoon season precipitation amounts averaged over the period 2003–2016.

amount of 4261 mm. In the west central region of the country, the annual precipitation amount is smallest. Rajshahi (24.37°N, 88.70°E) has the least annual precipitation amount (1252 mm).

In the pre-monsoon season, the precipitation amount is largest in the northeastern region of the country and it is larger in the southeastern region of the country than in the southwestern region (Fig. 2.4b). Sylhet (24.90°N, 91.88°E) near the Meghalaya Plateau is the rainiest place in the pre-monsoon season. In the monsoon season, the precipitation amount varies from 896 mm at Ishurdi (24.13°N, 89.05°E) in the west central region of the country to 3539 mm at Teknaf in the southeastern coastal region (Fig. 2.4c). Relatively large precipitation is observed in the northeastern region near the Meghalaya Plateau.

The water vapor flux  $q\mathbf{u}$ , where  $q$  is the water vapor mixing ratio and  $\mathbf{u}$  is the horizontal velocity, is calculated to examine differences in large-scale flow and moisture between the pre-monsoon and monsoon seasons in association with precipitation amount. The 900-hPa water vapor flux vector and its magnitude in the pre-monsoon and monsoon seasons are presented in Figs. 2.5a and 2.5b. Differences in water vapor flux between the pre-monsoon and monsoon seasons are clearly seen. In the pre-monsoon season, the relatively weak low-level southwesterly wind is prevalent over Bangladesh, and it transports moisture from the Bay of Bengal to inland area (Fig. 2.5a). In addition, the Arabian Sea serves as another moisture source for precipitation in Bangladesh, although its contribution is smaller than that of the Bay of Bengal (Tanoue et al. 2018). The water vapor flux is large in the northeastern region of the country. This is associated with the large precipitation amount there (Fig. 2.4b). In the monsoon season, on the other hand,

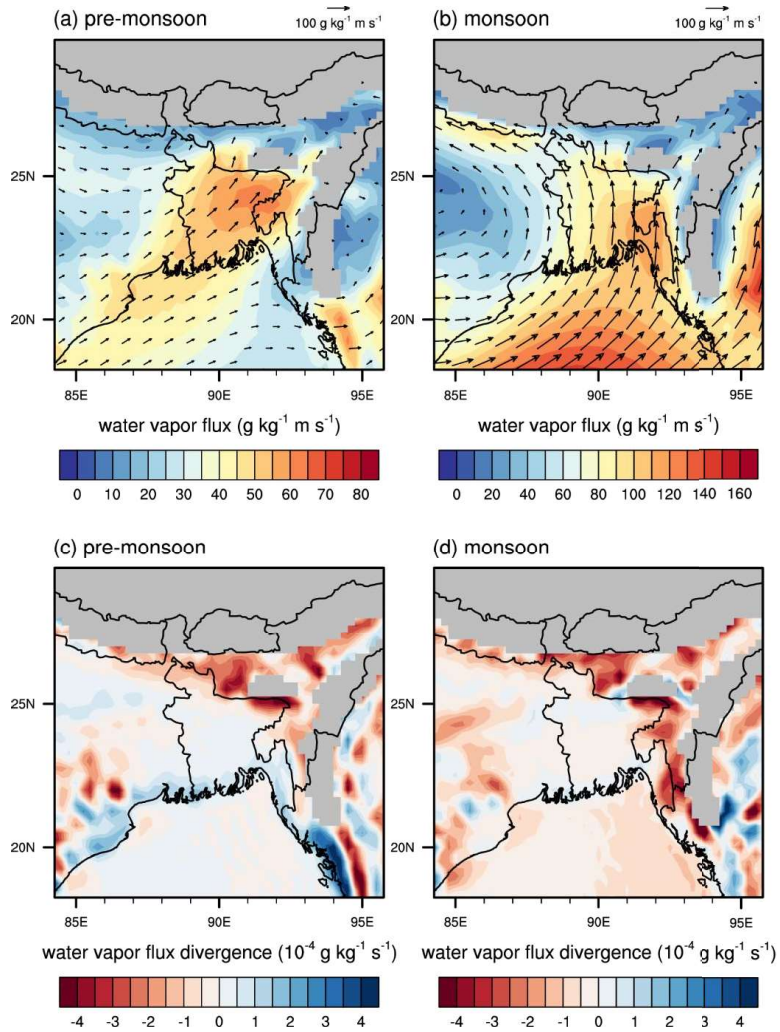


Figure 2.5 Fields of water vapor flux vector and its magnitude (color shading) at 900-hPa level averaged over the period 2003–2016 in the (a) pre-monsoon season and (b) monsoon season. (c) and (d) are the same as (a) and (b), respectively, except for the divergence of water vapor flux.

the strong low-level southwesterly wind from the Bay of Bengal enters the southern coast of the country with abundant moisture, indicating that the moisture source for monsoonal precipitation comes mainly from the Bay of Bengal. The southwesterly wind, then, turns to southerly wind, which is attributable to the blocking and deflecting effects of the Arakan Mountains (Wu et al. 2014), and the southerly wind becomes dominant over the country. The water vapor flux is large in the southeastern region of the country, which is associated with the large precipitation amount there (Fig. 2.4c).

Figures 2.5c and 2.5d shows the divergence of water vapor flux, that is,  $\nabla \cdot (q\mathbf{u})$ , at 900 hPa. In the pre-monsoon season, as expected from Fig. 2.5a, the water vapor flux convergence is large in the Meghalaya Plateau region, which is closely related to the large precipitation amount in the northeastern region of Bangladesh (Fig. 2.4b). A weak divergence of water vapor flux is found in the southeastern region although the precipitation amount in this region is larger compared to that in the southwestern region. This may be related to the large diurnal variability of the water vapor flux divergence in this region, which will be shown in the following subsection (see Fig. 2.8). In the monsoon season, the region of the Arakan Mountains exhibits a large water vapor flux convergence. This is closely related to the large precipitation amount in the southeastern region of the country (Fig. 2.4c).

The annual precipitation amount is distinctly smaller in 2016 (Fig. 2.2). As an attempt to find causes for this, we analyzed the annual, pre-monsoon, and monsoon precipitation amounts and the 900-hPa water vapor flux in the pre-monsoon and monsoon seasons for the year 2016 (not shown) and compared the results with those of Figs. 2.4 and 2.5. In 2016, the annual precipitation amount is decreased at all stations in



comparison with Fig. 2.4a. This implies that the distinctly smaller annual precipitation amount in 2016 could be associated with large-scale phenomena. The noticeable reduction of precipitation amount in the monsoon season in 2016 is mainly responsible for the distinctly smaller annual precipitation amount in 2016. The water vapor transport from the Bay of Bengal is noticeably reduced in 2016. However, it is unclear what caused the noticeable reduction in the water vapor transport, needing a further investigation.

### **2.2.2 Diurnal variation of precipitation**

The precipitation data at each station are analyzed to find the time of day at which the precipitation amount is largest. The stations whose precipitation peaks appear at similar times are grouped to investigate the diurnal variation of precipitation. In this way, Bangladesh is divided into three regions: northern (N), southwestern (SW), and southeastern (SE) regions (Fig. 2.1). The number of stations included is 6 in the N region, 10 in the SW region, and 11 in the SE region. The 3-h accumulated precipitation amounts averaged over stations in each region in the pre-monsoon and monsoon seasons are calculated. Their diurnal variations are presented in Fig. 2.6.

In the pre-monsoon season (Figs. 2.6a, 2.6c and 2.6e), the degree of the diurnal variability of precipitation is large in the N and SW regions but small in the SE region. In the N region, the precipitation amount largest in 0000–0300 LST and smallest in 1500–1800 LST. On the contrary, the pattern is almost opposite in the SW region: the precipitation amount is largest in 1800–2100 LST and smallest in 0300–0600 LST. In the monsoon season (Figs. 2.6b, 2.6d and 2.6f), the precipitation amount is larger in the SE

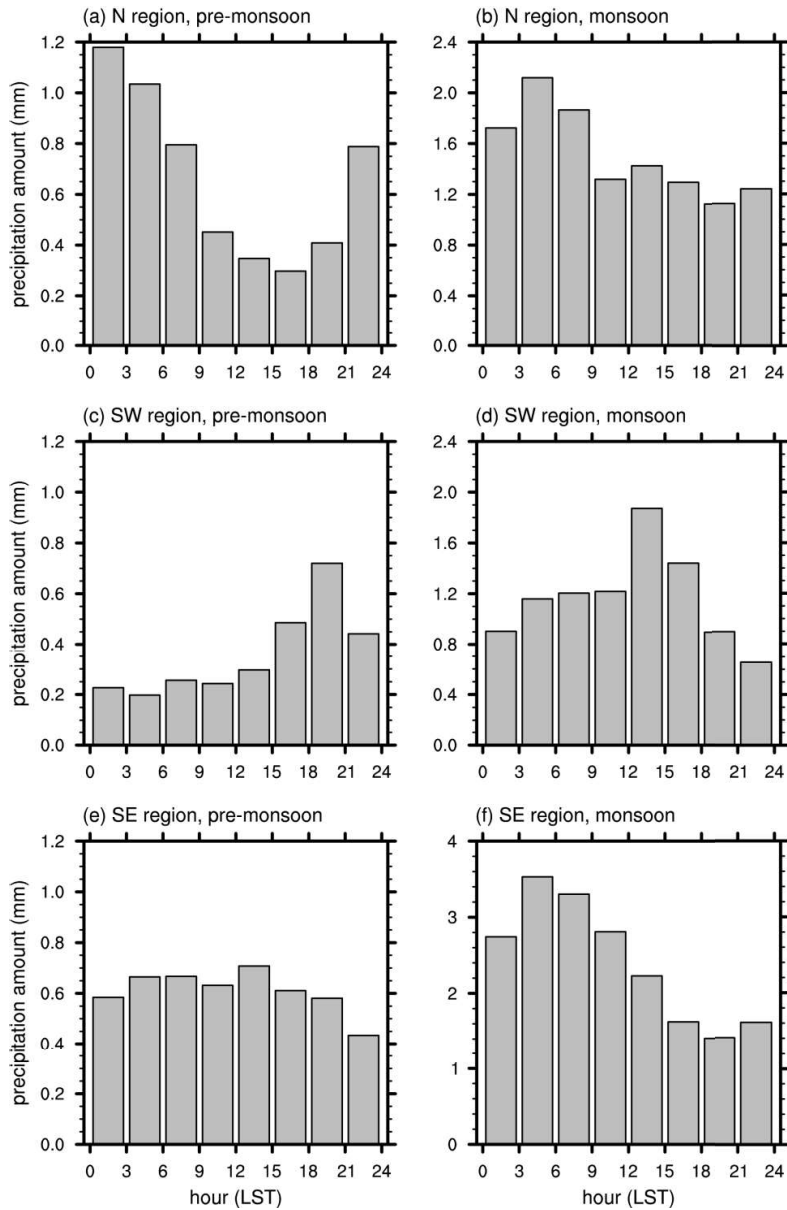


Figure 2.6 Diurnal variations of 3-h accumulated precipitation amount averaged over stations in the (a) northern (N), (c) southwestern (SW), and (e) southeastern (SE) regions in the pre-monsoon season and those in the (b) N, (d) SW, and (f) SE regions in the monsoon season. Note that the  $y$ -axis limits in the plots of the pre-monsoon and monsoon seasons are different.

region than in the N and SW regions and the degree of the diurnal variability of precipitation in the SW region is larger than that in the N region. The pattern of the diurnal variation of precipitation in the SE region is similar to that in the N region: the precipitation amount is largest in 0300–0600 LST and smallest in 1800–2100 LST. In the SW region, the precipitation amount is largest in 1200–1500 LST and smallest in 2100–0000 LST. These results from Fig. 2.6 imply that mechanisms or factors responsible for the diurnal variation of precipitation are different depending on regions of Bangladesh.

To quantify a diurnal variability of precipitation in each region and each season,  $D$  is defined as Eqs. (2.1) and is calculated using the data used to plot Fig. 2.6.

$$D = \frac{P_{\max} - P_{\min}}{P_m}, \quad (2.1)$$

where  $P_{\max}$ ,  $P_{\min}$ , and  $P_m$  are the daily maximum (largest), minimum (smallest), and mean precipitation amounts, respectively. The calculated  $D$  values in the N, SW, and SE regions in the pre-monsoon and monsoon seasons are given in Table 2.1. Compared with the N and SE regions, the SW region experiences the largest diurnal variability of precipitation in both the pre-monsoon and monsoon seasons. In the pre-monsoon season, the diurnal variability of precipitation is larger in the SW region than in the SE region. This seems to be associated with the larger diurnal variation of convective instability in the SW region than in the SE region, as will be shown in Figs. 2.7c and 2.7e.

Table 2.1 Diurnal variability of precipitation  $D$  in each region and each season.

Season	Region		
	N	SW	SE
Pre-monsoon	1.33	1.46	0.45
Monsoon	0.66	1.04	0.88

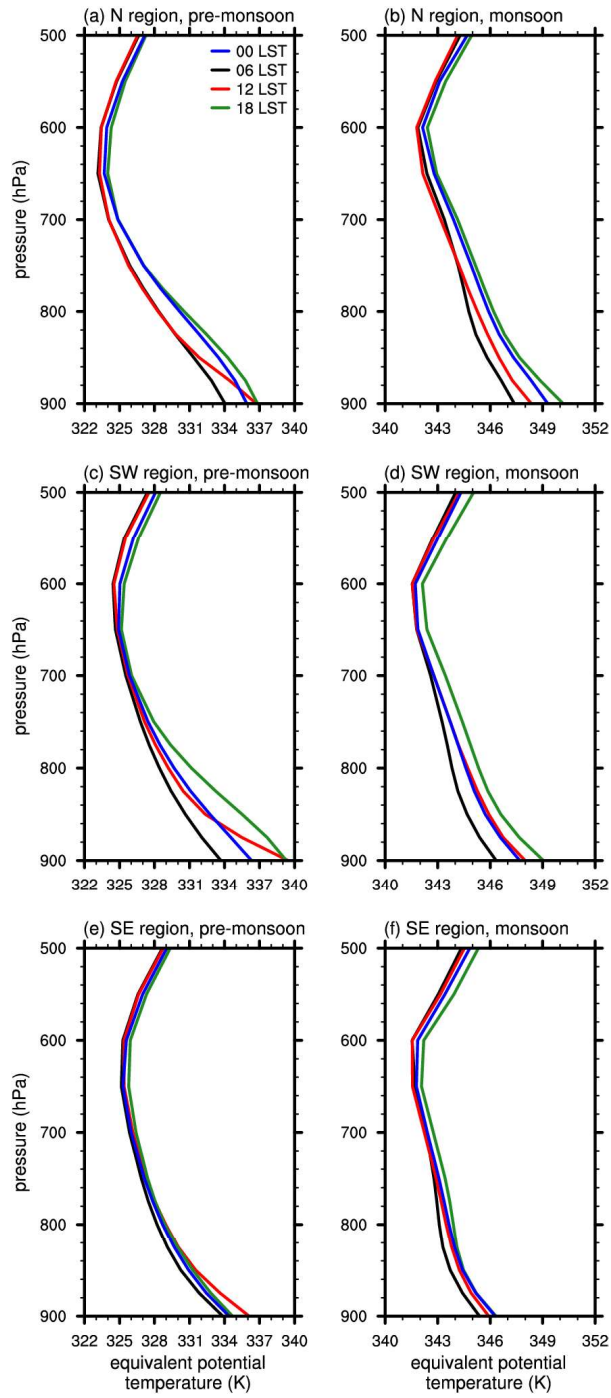


Figure 2.7 Vertical profiles of equivalent potential temperature at 0000, 0600, 1200, and 1800 LST averaged over stations in the (a) northern (N), (c) southwestern (SW), and (e) southeastern (SE) regions in the pre-monsoon season and those in the (b) N, (d) SW, and (f) SE regions in the monsoon season.

Next, we attempt to associate the features of the diurnal variations of precipitation in Bangladesh with large-scale thermodynamic and dynamic characteristics. The vertical profiles of equivalent potential temperature at different local times are presented in Fig. 2.7. Two features are pronounced in Fig. 2.7. One prominent feature is that in both the pre-monsoon and monsoon seasons, the atmosphere is conditionally unstable (i.e., the equivalent potential temperature decreases with height) below  $\sim 600\text{--}650$  hPa and stable (i.e., the equivalent potential temperature increases with height) above it. The other prominent feature is that the atmosphere is more conditionally unstable in the pre-monsoon season than in the monsoon season. This implies that the pre-monsoonal precipitation is more convective in nature than the monsoonal precipitation.

In the pre-monsoon season, the diurnal variation of equivalent potential temperature below  $\sim 700$  hPa is larger in the SW region than in the N and SE regions (Figs. 2.7a, 2.7c and 2.7e). The effect of this large diurnal variation of equivalent potential temperature is to some extent reflected in the large diurnal variability of precipitation (Fig. 2.6c). In the SW region, the atmosphere is noticeably conditionally unstable below  $\sim 830$  hPa at 1200 LST compared with other times. The large convective instability could be a cause for the precipitation maximum in the early evening in the SW region (Fig. 2.6c). The SE region experiences the least diurnal variation of equivalent potential temperature. In the monsoon season, the diurnal variation of equivalent potential temperature is small compared with the pre-monsoon season in all of the three regions. As in the pre-monsoon season, the diurnal variation of equivalent potential temperature in the monsoon season is smallest in the SE region among the three regions. It is, however, interesting to note that the diurnal variability of precipitation in the SE region is about



two times larger in the monsoon season ( $D = 0.88$ ) than in the pre-monsoon season ( $D = 0.45$ ), indicating that factors other than conditional instability would be responsible for the larger diurnal variability of precipitation in the monsoon season.

The 950-hPa horizontal velocity and water vapor flux divergence are examined (Fig. 2.8). The 950-hPa level rather than the 900-hPa level as in Fig. 2.5 is chosen to get a more glimpse of the influences of the high mountains in and near Bangladesh. Over Bangladesh, the low-level wind is stronger at all times in the monsoon season than in the pre-monsoon season. In the pre-monsoon season, the convergence of water vapor flux in the N region is largest at 0000 LST, which is associated with the precipitation maximum in 0000–0300 LST (Fig. 2.6a). It becomes weak at 1200 and 1800 LST, even with the divergence of water vapor flux being present at 1200 LST in part of the N region, which is associated with the precipitation minimum in 1500–1800 LST (Fig. 2.6a). Similar features are also evident in the monsoon season, but with slightly different times of the precipitation maximum/minimum (Fig. 2.6b and 2.8b). There is a divergence of water vapor flux in part of the SW region at 0000 LST in the pre-monsoon season (Fig. 2.8a), which is connected with the precipitation minimum in 0300–0600 LST (Fig. 2.6c). In the monsoon season, the convergence of water vapor flux overall becomes weak over Bangladesh except for the southwestern region of the country, with the divergence of the water vapor flux appearing in part of the northwestern region of the country. In the SW region, the convergence of water vapor flux is largest at 1200 LST (Fig. 2.8f) and this is associated with the precipitation maximum in 1200–1500 LST (Fig. 2.6d). In the SE region, the convergence of water vapor flux is largest at 1200 LST (Fig. 2.8f) and this is associated with the precipitation maximum in 1200–1500 LST (Fig. 2.6d). In the SE

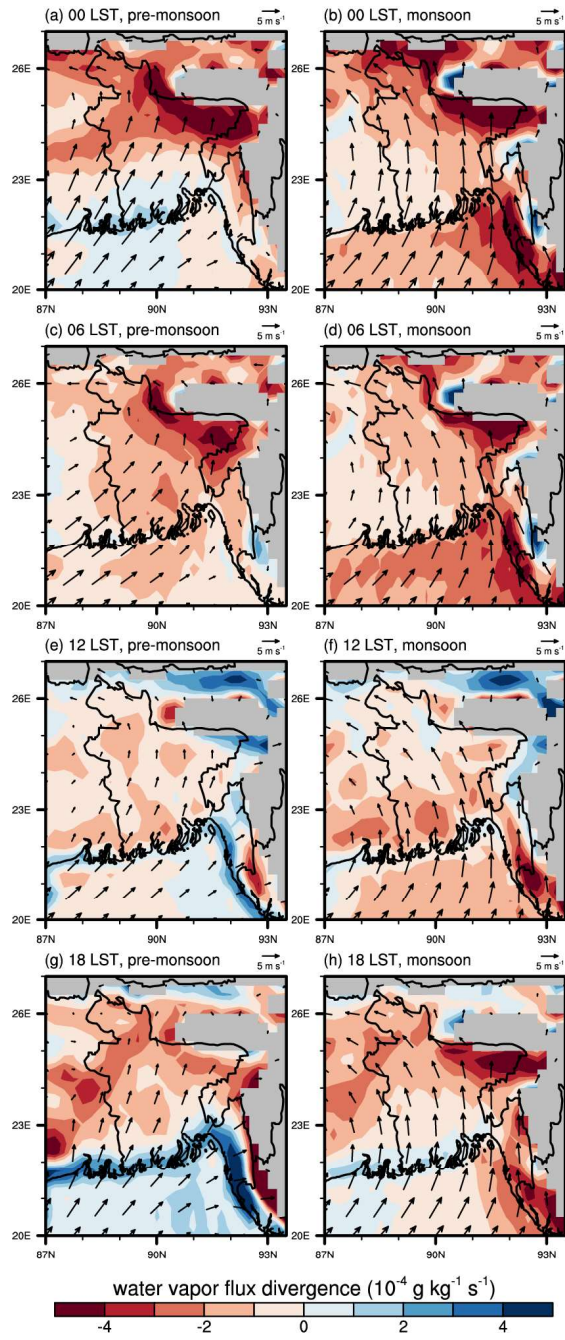


Figure 2.8 Fields of horizontal wind vector and the divergence of water vapor flux (color shading) at 950 hPa level averaged over the period 2003–2016: (a) 0000 LST, (c) 0600 LST, (e) 1200 LST, and (g) 1800 LST in the pre-monsoon season and (b) 0000 LST, (d) 0600 LST, (f) 1200 LST, and (h) 1800 LST in the monsoon season.

region, the convergence of water vapor flux is generally large in the nighttime compared with that in the daytime (Figs. 2.8b, 2.8d, 2.8f and 2.8h), overall consistent with the precipitation maximum 0300–0600 LST (Fig. 2.6f). It is observed from Fig. 2.8 that in both the pre-monsoon and monsoon seasons, the low-level wind over Bangladesh is stronger in the nighttime than in the daytime. This leads to more nighttime moisture transport, especially from the Bay of Bengal in the monsoon season.

In the nighttime, the downslope wind produced by cooling over the high terrain of the Himalaya Mountains meets with the approaching low-level moist unstable airflow and causes nighttime or early morning precipitation maxima near the Himalayan foot (Romatschke et al. 2010; Houze 2014). The northwestern region of Bangladesh is located close to the Himalayan Foothills. So, this mechanism could to some extent explain the late night to early morning maximum of precipitation in the northwestern region of the country. However, further investigations are needed to confirm this mechanism. It should be noted that in the nighttime, the converging wind due to the Himalaya Mountains, which is accompanied by more moisture transport due to the strengthened nighttime low-level wind, plays an important role in enhancing nighttime precipitation in the northwestern region of Bangladesh. Similarly, the Meghalaya Plateau and more nighttime moisture transport could contribute to the nighttime maximum of precipitation in the northeastern region of the country.

Kataoka and Satomura (2005) reported an interesting numerical modeling result that the katabatic mountain wind does not play a major role in the diurnal variation of precipitation in the northeastern region of Bangladesh. Although the result is obtained through a case study, it is in contradiction with the speculation that in the northeastern

region of the country, the katabatic mountain wind plays a major role in the diurnal variation of precipitation (Prasad 1970; Ohsawa et al. 2000). Further numerical modeling studies with numerous cases would help to find to what extent the katabatic mountain wind (the downslope wind) contributes to the late night to early morning precipitation maximum in the northeastern region of Bangladesh.

Fujinami et al. (2017) showed that in the monsoon season, the reduced vertical mixing in the stable boundary layer in the nighttime accelerates the low-level jet towards the Meghalaya Plateau, which acts to intensify nighttime precipitation. This is largely in line with our result.

The averaged spatiotemporal characteristics of precipitation found in this study may be to some or large extent affected by extreme variations of large-scale circulation. To examine whether our conclusions are the same even after excluding extreme large-scale events, the analysis is performed in which the years with strong IOD, La Niña, and El Niño are excluded. It is found that the analysis ends up with the results that are very similar to those calculated from the whole 14-year period, because the positive and negative deviations in these years are cancelled out by each other (not shown).

### **3 Evaluation and CSEOF analysis of IMERG data for precipitation studies in Bangladesh and surrounding regions**

#### **3.1 IMERG data description and CSEOF analysis method**

##### **3.1.1 IMERG data description**

As a next generation satellite precipitation observation system, the Global Precipitation Measurement (GPM) mission was launched on February 2014 by the National Aeronautics and Space Administration (NASA) and the Japan Aerospace Exploration Agency (JAXA) as a successor of TRMM (Hou et al. 2014; Yong et al. 2015). Accordingly, a new precipitation product made by GPM satellites, IMERG, became available to the public since January 2015, in place of an old precipitation product, TRMM Multi-satellite Precipitation Analysis (TMPA). The GPM satellites are equipped with upgraded instruments compared to the TRMM satellite. The GPM satellite constellation consists of a main satellite called the GPM Core Observatory and many supplementary satellites. The GPM Core Observatory uses the Dual-frequency (Ku-band at 13.6 GHz and Ka-band at 35.5 GHz) Precipitation Radar (DPR) instead of the single-frequency Precipitation Radar (PR) in the TRMM satellite. The GPM Core Observatory also carries the multichannel GPM Microwave Imager (GMI) which has high-frequency channels (165.5, 183.3±3, and 183.3±7 GHz) that the TRMM Microwave Imager (TMI) does not have. The use of a broader spectrum enables the GPM satellites to detect light precipitation better than the TRMM satellite.

IMERG version 06B with a spatial resolution of  $0.1^{\circ} \times 0.1^{\circ}$  and a temporal resolution of 30 min is used in this study. The IMERG data are created by the following procedure. First, initial precipitation estimates are calculated by the 2017 version of Goddard Profiling Algorithm (GPROF2017) using data from passive microwave (PMI) sensors in the GPM satellite constellation. Second, the initial precipitation estimates go through the Climate Prediction Centre (CPC) Morphing-Kalman Filter (CMORPH-KF) quasi-Lagrangian time interpolation procedure and the Precipitation Estimation from Remotely Sensed Information using Artificial Neural Networks-Cloud Classification System (PERSIANN-CCS) infrared (IR) re-calibration procedure. Finally, the outputs from the second stage are multiplied by some spatially varying factor in order to match the summation of the outputs for a month with that of the rain gauge data from Global Precipitation Climatology Centre (GPCC) (Schneider et al. 2018). For more detailed information about the IMERG data and the GPM mission, see Huffman et al. (2019, 2020).

In this study, the 3-hourly rain gauge data from the Bangladesh Meteorological Department (BMD) during 2015–2019 are used for the evaluation of the IMERG data. Total 35 meteorological stations (Fig. 3.1) are spread in the country, but the data from Jessore ( $23.18^{\circ}\text{N}$ ,  $89.16^{\circ}\text{E}$ ) and Hatiya ( $22.58^{\circ}\text{N}$ ,  $91.7^{\circ}\text{E}$ ) are excluded from the analysis because of missing values. For the comparison between the IMERG data and the rain gauge data, the IMERG data with  $0.1^{\circ} \times 0.1^{\circ}$  spatial resolution and 30-min time interval are bilinearly interpolated to the locations of the rain gauge stations and converted to 3-hourly data. We confirmed that, in this study, using the IMERG data of the grid point closest to each rain gauge station does not make any significantly different results from

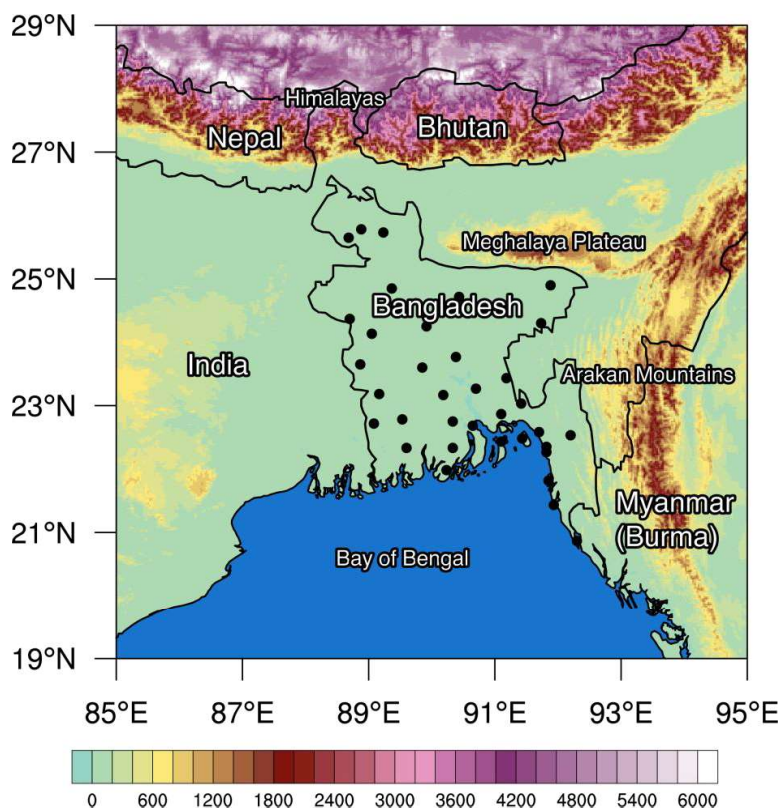


Figure 3.1 Topographic map of Bangladesh and surrounding regions with the locations of 35 rain gauge stations (black circles)



using the bilinear interpolation method.

### 3.1.2 CSEOF analysis method

In the CSEOF analysis method (Kim and North 1997; Kim et al. 2015; Kim 2017), original data  $T(r, t)$  called the target variable are decomposed as follows:

$$T(r, t) = \sum_n B_n(r, t) T_n(t). \quad (3.1)$$

Here,  $B_n(r, t)$  are decomposed spatio-temporal patterns called the CSEOF loading vectors (hereafter, CSLVs) and  $T_n(t)$  are corresponding time-varying amplitudes called the principal component time series (hereafter, PC time series).  $B_n(r, t)$  are periodic in time and mutually orthogonal to each other:

$$B_n(r, t) = B_n(r, t + d), \quad (3.2)$$

$$\frac{1}{Nd} \sum_{r=1}^N \sum_{t=1}^d B_n(r, t) B_m(r, t) = \delta_{nm}, \quad (3.3)$$

where  $d$  is the nested period,  $N$  is the number of spatial points in the original data, and  $\delta_{nm}$  is the Kronecker delta.  $T_n(t)$  are mutually uncorrelated to each other:

$$\frac{1}{M} \sum_{t=1}^M T_n(t) T_m(t) = \lambda_n \delta_{nm}, \quad (3.4)$$

where  $M$  is the number of temporal points in the original data and  $\lambda_n$  is the variance of  $T_n(t)$ . Each CSLV and its PC time series are collectively called a mode. Each mode is regarded as representing a distinct physical process.

In this study, the IMERG data are processed before the CSEOF analysis is conducted. First, the half-hourly IMERG data are converted to 3-hourly data for comparison with rain gauge data. Then, the 3-hourly data are averaged across the 5 years; for example, the precipitation amount in 0000–0300 LST on 1 January is obtained by averaging the precipitation amounts in the same time and date in the five different years. The CSEOF analysis is conducted for the pre-monsoon (March to May) and monsoon (June to September) seasons separately to find characteristic precipitation patterns for each season. The nested period is set to 24 h to examine diurnal variations of precipitation in the pre-monsoon and monsoon seasons.

The main variable in this study is the anomaly of precipitation amount, computed by subtracting the seasonal-mean precipitation amount field. This variable is the target variable which is  $T(r, t)$  in Equation (3.1). For each CSEOF mode of the target variable, spatio-temporal patterns of another variable (predictor variable,  $P(r, t)$ ), which are physically consistent with those of the target variable, can be obtained using the regression analysis in CSEOF space (Kim et al. 2015). Here, physical consistency means that two spatio-temporal patterns originated from different variables have identical time-varying amplitudes:

$$\{T(r,t), P(r,t)\} = \sum_n \{B_n(r,t), C_n^{(\text{reg})}(r,t)\} T_n(t), \quad (3.5)$$

where  $C_n^{(\text{reg})}(r,t)$  are the regressed spatio-temporal patterns extracted from the predictor variable. By conducting the regression analysis on other variables which are related to the target variable, a mechanism corresponding to each CSEOF mode of the target variable can be suggested.

In this study, the reanalysis data from the European Centre for Medium-Range Weather Forecasts Reanalysis version 5 (ERA5, Hersbach et al. 2020) are used for the regression analysis. The anomaly of water vapor flux at 900 hPa is selected as a predictor variable and calculated from the wind vector and specific humidity in the hourly ERA5 data. The data of the predictor variable are processed using the same method used to process the IMERG data (i.e., converting to 3-hourly data, averaging across the 5 years). Note that when converting the hourly data to 3-hourly data, for example generating the data in 0000–0300 LST (UTC + 6 h), the three hourly data at 0000, 0100, and 0200 LST are averaged. More detailed descriptions of the CSEOF analysis method and the regression analysis method are provided in Kim and North (1997), Kim et al. (2015), and Kim (2017).

## **3.2 Results and discussion**

### **3.2.1 Evaluation of IMERG data**

In this subsection, the IMERG data in the period 2015–2019 are evaluated through the comparison with the rain gauge data provided by BMD. The 3-h accumulated precipitation amounts from the IMERG data are compared with the rain gauge data in density scatter plots, for each season (Fig. 3.2). The density scatter plots show somewhat dispersed patterns of relative frequency. Overestimation of precipitation by the IMERG data occurs relatively frequently for very small precipitation amounts, and underestimation occurs relatively frequently for large precipitation amounts. The correlation coefficients between 3-hourly precipitation amounts from the IMERG data and those from the rain gauge data are 0.58, 0.58, and 0.60 for the pre-monsoon, monsoon, and post-monsoon seasons. The winter season when the seasonal precipitation amount is small shows a relatively low correlation coefficient (0.51). The IMERG data are known to have a better accuracy for a coarser temporal resolution, for example, for 1-day precipitation amounts (e.g., Tang et al. 2016). The correlation coefficients for 1-day precipitation amounts are 0.71, 0.76, 0.80, and 0.63 for the pre-monsoon, monsoon, post-monsoon, and winter seasons, which are much higher than those for 3-hourly precipitation amounts. This implies that the IMERG data can be used with a higher reliability for precipitation studies considering a larger time scale.

Latest versions of the IMERG data also provide the precipitation estimates for the period before the operation of the GPM Core Observatory satellite, when the TRMM satellite was operating, using the data from the TRMM satellite. The IMERG data in this period (2003–2013) are less accurate than the data in the later period, showing lower

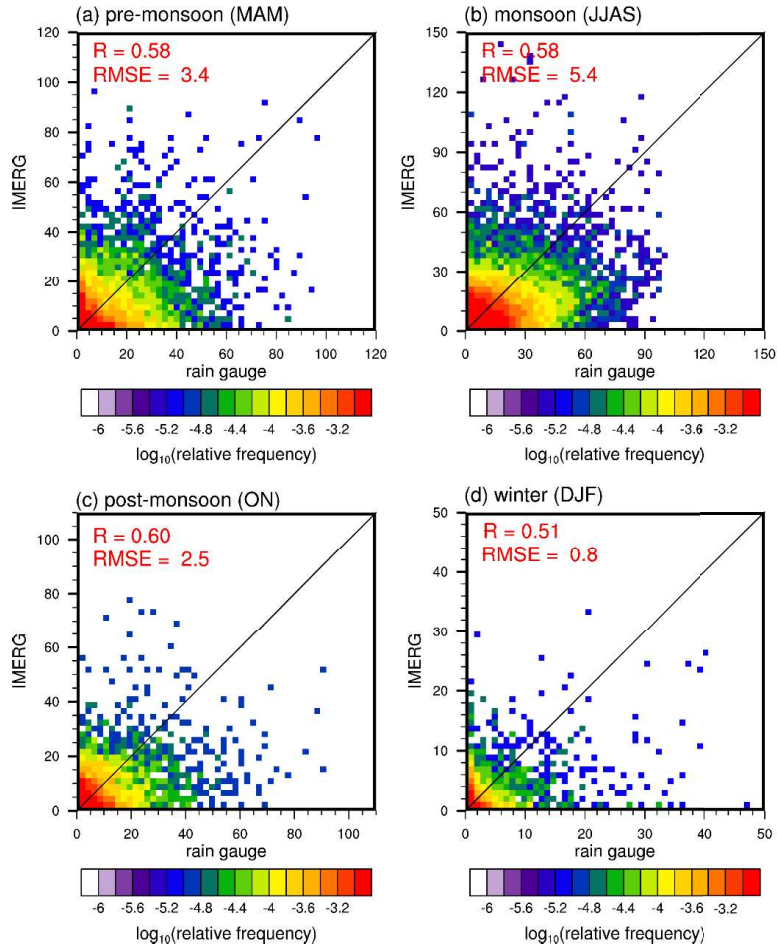


Figure 3.2 Density scatter plot between 3-hourly precipitation amounts from the IMERG data and those from rain gauge data in the (a) pre-monsoon, (b) monsoon, (c) post-monsoon, and (d) winter seasons.

correlation coefficients against the rain gauge data (0.54, 0.55, 0.57, and 0.44 for the pre-monsoon, monsoon, post-monsoon, and winter seasons). For this reason, only the IMERG data in the period 2015–2019 when the GPM Core Observatory satellite was operating are used for the evaluation in this study.

The comparison of precipitation amount in each season obtained from the rain gauge and IMERG data in Bangladesh is shown in Fig. 3.3. In the pre-monsoon season, the monthly-mean precipitation amounts in the IMERG and rain gauge are 160 mm and 155 mm respectively, indicating a small overestimation (3%) in the IMERG. The IMERG well estimates the monthly-mean precipitation amount in the monsoon season with a 6% overestimation. A relatively large overestimation (11%) is shown in the post-monsoon season. In the winter season, a negligible amount of precipitation is observed and the precipitation amount is overestimated in the IMERG. Overall, the IMERG estimates are in good agreement with the rain gauge observation.

The diurnal variation of precipitation is one of the most important features of precipitation in Bangladesh (Islam et al. 2005). Figure 3.4 shows the diurnal variations of precipitation amount in the country in each season revealed by both the IMERG and rain gauge data. The rain gauge shows that in the pre-monsoon season (Fig. 3.4a), the degree of diurnal variability is low and the precipitation maximum occurs in 0600–0900 LST. In contrast, the IMERG shows a higher degree of diurnal variability and the precipitation maximum occurs in 2100–0000 LST. The IMERG tends to underestimate precipitation in 0300–1200 LST, while it overestimates precipitation in 1200–0300 LST. In the monsoon season (Fig. 3.4b), precipitation exhibits a primary peak in the early morning (0300–0600 LST) and a secondary peak in the afternoon (1200–1500 LST) in both the IMERG and

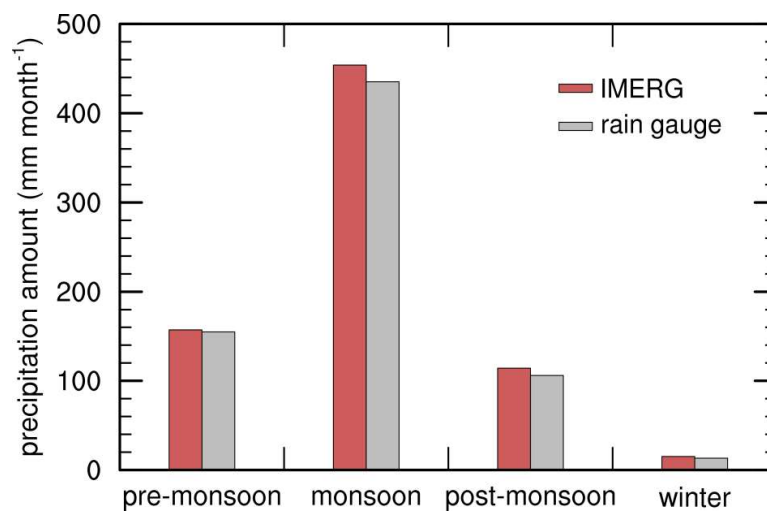


Figure 3.3 Seasonal variations of monthly-mean precipitation amount averaged over the period 2015–2019 for the IMERG data and rain gauge data.

rain gauge. The IMERG identifies the two peaks in the rain gauge, with a slight underestimation (5%) for the primary peak and a slight overestimation (2%) for the secondary peak. It is also shown that the IMERG overestimates precipitation in 0900–0300 LST and underestimates precipitation in 0300–0900 LST. The diurnal variation of precipitation in the post-monsoon season (Fig. 3.4c) is quite different from that in the monsoon season. In the post-monsoon season, precipitation is decreased and its peak is shifted to a later time compared to the monsoon season, indicating a seasonal change of the diurnal variation of precipitation. The rain gauge shows a primary peak in 1200–1500 LST. The IMERG successfully captures the diurnal variation of precipitation pattern with a precipitation peak in 1200–1500 LST and a precipitation amount of 0.58 mm in 1200–1500 LST that is the same as the rain gauge observation. However, precipitation is overestimated in other times. In the winter season (Fig. 3.4d), the diurnal variation of precipitation is somewhat similar to that in the monsoon season with a peak in 0300–0600 LST. The IMERG underestimates precipitation in times with relatively large precipitation amount (0300–0900 LST) and overestimates precipitation in times with relatively small precipitation amount (0900–2400 LST), showing a lower degree of diurnal variability than the rain gauge.

The spatial distributions of monthly-mean precipitation amounts in the IMERG data are evaluated in Fig. 3.5. The observed spatial patterns of precipitation are overall well reproduced by the IMERG, while substantial overestimations and underestimations are found in some regions in some seasons. In the pre-monsoon season, the underestimation of the monthly-mean precipitation amount at Sylhet (24.90°N, 91.88°E), located near the southern slope of the Meghalaya Plateau, is noticeable. In the monsoon



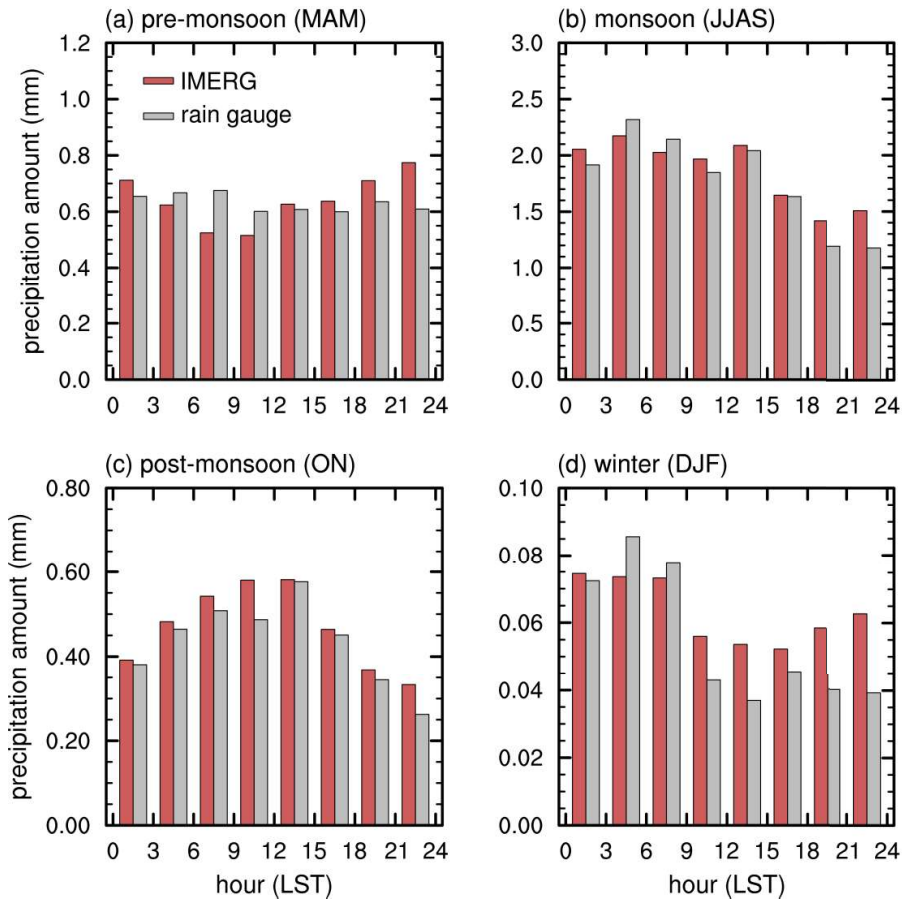


Figure 3.4 Diurnal variations of 3-hourly precipitation amount in the (a) pre-monsoon, (b) monsoon, (c) post-monsoon, and (d) winter seasons averaged over the period 2015–2019 for the IMERG data and rain gauge data.

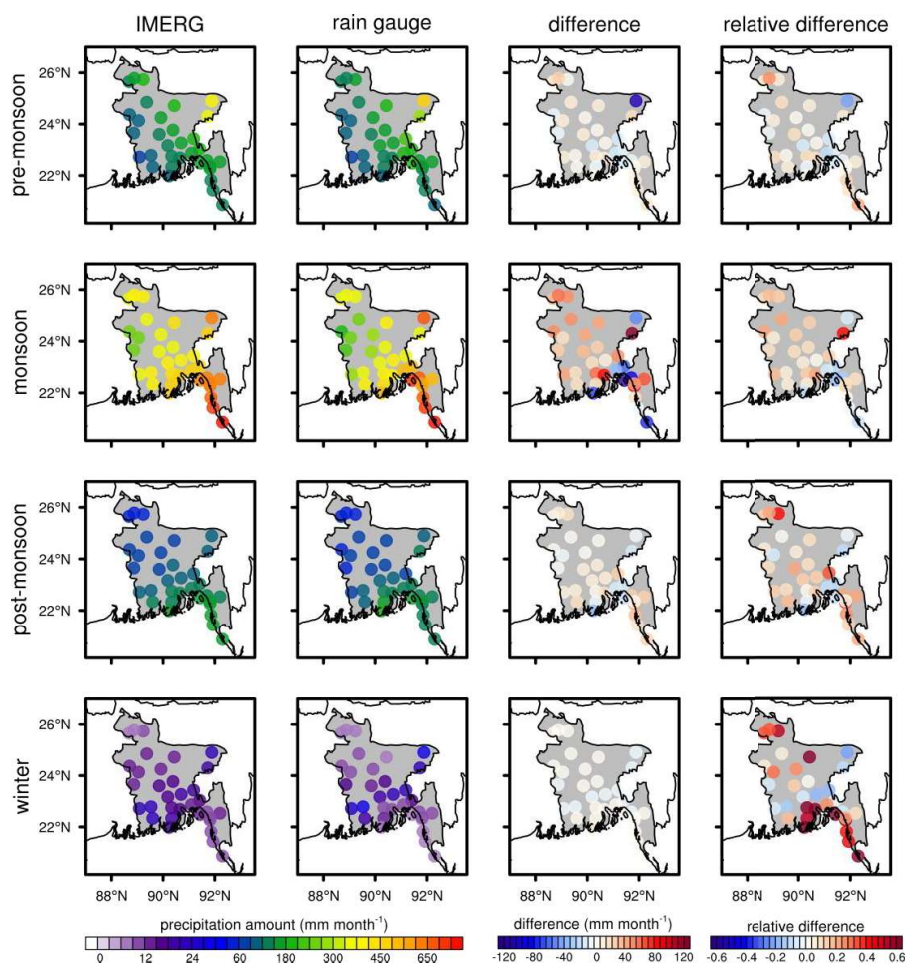


Figure 3.5 Spatial distributions of monthly precipitation amounts in the pre-monsoon (first row), monsoon (second row), post-monsoon (third row), and winter (fourth row) seasons averaged over the period 2015–2019 for the IMERG data (first column), rain gauge data (second column), their differences (IMERG – rain gauge) (third column) and their relative differences (fourth column).

season, the IMERG tends to overestimate precipitation in the western half of Bangladesh where the precipitation amounts are relatively small and it underestimates precipitation at Sylhet and some stations in the southeastern region where the precipitation amounts are relatively large. The largest overestimation in the monsoon season is found at Srimangal (24.30°N, 91.73°E), located a little south of Sylhet where a significant underestimation occurs. The IMERG does not capture the drastic horizontal change in precipitation amount observed in the northeastern region of Bangladesh. In the post-monsoon season, overestimations are found at a majority of rain gauge stations. In the winter season, big relative differences are found at some stations in the northwestern and southeastern regions where the observed precipitation amounts are very small and overestimated by the IMERG.

The IMERG well reproduces the seasonal variation of precipitation. For the diurnal variation of precipitation, the IMERG captures the overall patterns despite some overestimations and underestimations. The spatial distribution of precipitation is also captured well, except for the northeastern region which exhibits the drastic horizontal change in precipitation amount. These results suggest that the IMERG precipitation product can be used for studying the spatio-temporal variations of precipitation in Bangladesh, with a proper consideration of the revealed biases.

### **3.2.2 CSEOF analysis**

#### **3.2.2.1 Pre-monsoon**

Figure 3.6 shows the fields of diurnal variations of the first and second CSLVs of precipitation amount anomaly in the pre-monsoon season, and Fig. 3.7 shows

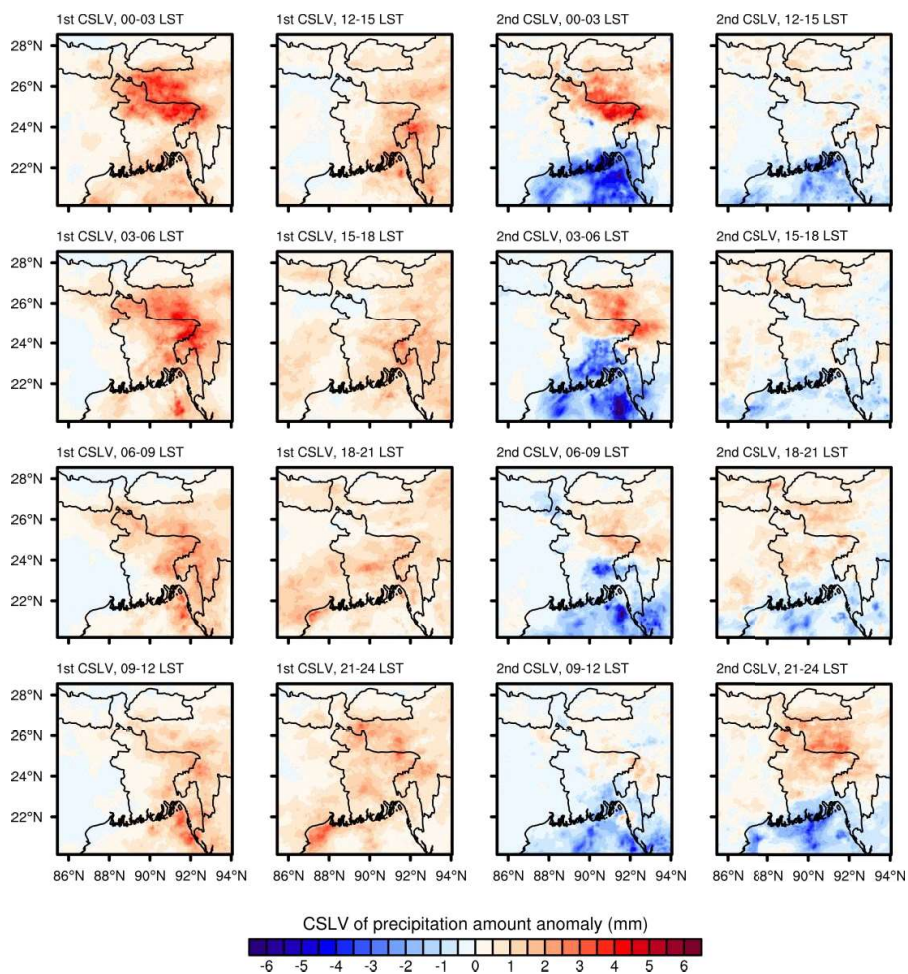


Figure 3.6 3-hourly CSLVs for the first (two leftmost columns) and second (two rightmost columns) CSEOF modes of precipitation amount anomaly in the pre-monsoon season.

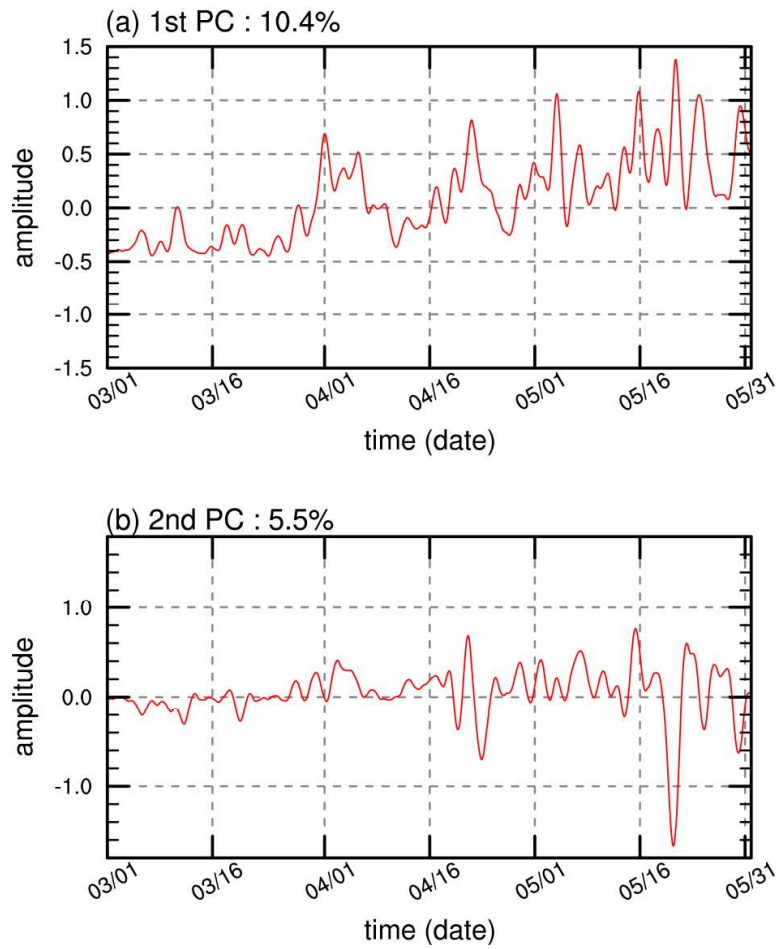


Figure 3.7 PC time series for the (a) first and (b) second CSEOF modes of precipitation amount anomaly in the pre-monsoon season.

corresponding PC time series. The first CSLV is characterized by strong positive precipitation anomalies in the northern region of Bangladesh and the Meghalaya Plateau region in 0000–0600 LST. These anomalies are weakened in the daytime and strengthened in the late night, exhibiting a clear diurnal cycle. In 1800–2100 LST, the central region of the country exhibits a relatively strong positive anomaly compared to other regions. The PC time series of the first CSEOF mode shows that the amplitude of diurnal cycle is relatively small in March, and it grows overall from mid-April to late May. The peak times of precipitation anomalies in the northern and central regions of Bangladesh are consistent with the peak times of pre-monsoonal precipitation in those regions, implying that the first mode represents the general characteristics of the diurnal variation of precipitation. The first mode contributes 10.4% to the total variance of the pre-monsoonal precipitation.

The second CSLV is characterized by strong positive precipitation anomalies in the northeastern region of Bangladesh and the Meghalaya Plateau region and strong negative precipitation anomalies in the southern region of the country and the northern region of the Bay of Bengal (BOB) in 0000–0600 LST. The PC time series of the second CSEOF mode is mostly in a positive phase since late March. The positive phase indicates the enhancement of precipitation in the northern region of Bangladesh and the Meghalaya Plateau region and the suppression of precipitation in the southern region of Bangladesh and the northern region of the BOB. The second mode that represents the north–south precipitation difference contributes 5.5% to the total variance of the pre-monsoonal precipitation.

Figure 3.8 shows the fields of diurnal variations of CSLVs of 900-hPa water vapor flux anomaly regressed to the first and second modes of the pre-monsoonal precipitation anomaly. In the first regressed mode, the water vapor flux anomaly is southwesterly over the BOB and mainly southerly in Bangladesh, indicating the enhancement of moisture transport from the BOB to inland Bangladesh. The southern slope of the Meghalaya Plateau exhibits southerly water vapor flux anomaly in 0000–0600 LST and southeasterly water vapor flux anomaly in 0900–1500 LST. Because the southern slope of the Meghalaya Plateau is east–west oriented, the enhancement of the meridional component of water vapor flux anomaly in this region in 0000–0600 LST results in stronger orographic lifting and upward moisture transport. This can intensify precipitation in the plateau and surrounding regions in this time, which is represented by the strong positive precipitation anomalies (Fig. 3.6). The strengthening of the diurnal cycle of precipitation since mid-April is linked with the enhancement of the water vapor flux anomaly in the same period (Fig. 3.7a).

In the second regressed mode, the water vapor flux anomaly in Bangladesh is relatively strong, while it is relatively weak in the northern region of the BOB. In contrast with the first regressed mode, the second regressed mode shows the spatial pattern of water vapor flux anomaly that varies substantially with time. In 0000–0900 LST, the water vapor flux anomaly is mostly directed toward the BOB at the east coast of India and the west coast of Myanmar. In contrast, in 1500–2100 LST, the water vapor flux anomaly is mostly directed toward land at the coasts. These can be somewhat attributed to the land-sea breeze circulation in the coastal regions along with the mountain-valley breeze circulation around the Arakan Mountains. The southwesterly water vapor flux



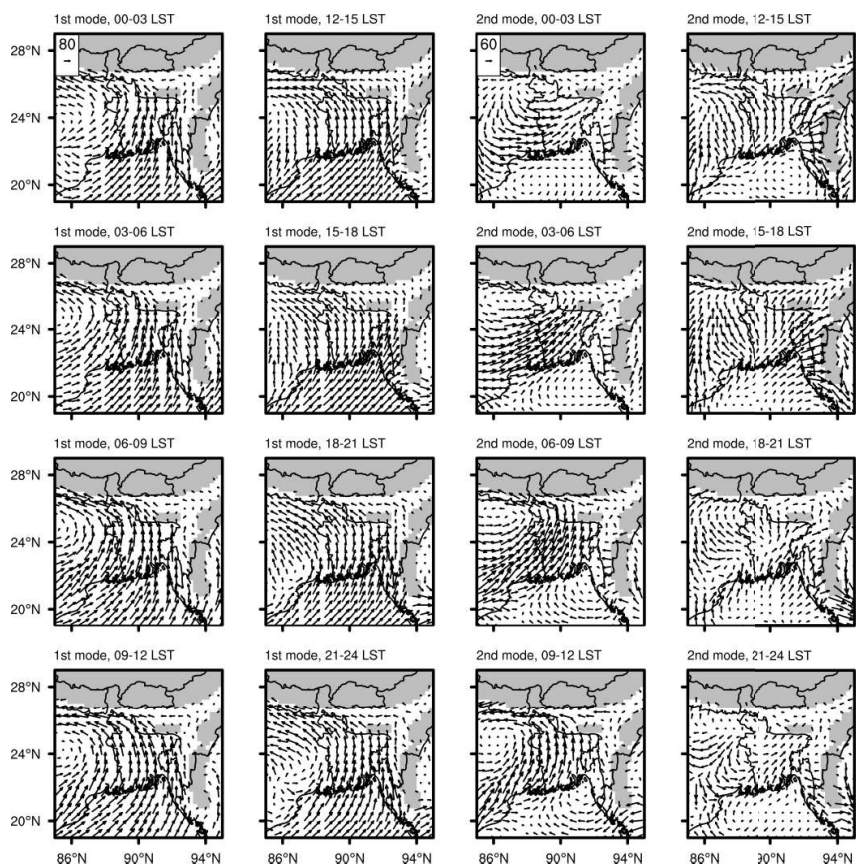


Figure 3.8 Regressed 3-hourly CSLVs of 900-hPa water vapor flux anomaly ( $\text{g kg}^{-1} \text{ m s}^{-1}$ ) associated with the first (two leftmost columns) and second (two rightmost columns) CSEOF modes of precipitation amount anomaly in the pre-monsoon season.

anomaly in Bangladesh is strong in 0000–0900 LST, indicating that the precipitation anomalies in the northeastern region and the Meghalaya Plateau region in this time in this mode is associated with the enhancement of southwesterly moisture transport, which does not directly come from the BOB. On the other hand, the suppression of precipitation in the northern region of the BOB in this mode can be linked with the relatively weak water vapor flux anomaly in this region. When the PC time series is in a negative phase, the southwesterly water vapor flux anomaly in Bangladesh in 0000–0900 LST is reversed and it acts against the mean southwesterly water vapor flux in the pre-monsoon season. The weakening of moisture transport approaching the southern slope of the Meghalaya Plateau reduces the precipitation in the northeastern region of Bangladesh and the Meghalaya Plateau region and enhances the precipitation in the southern region of Bangladesh and the northern region of the BOB.

### **3.2.2.2 Monsoon**

The fields of diurnal variations of the first and second CSLVs of precipitation amount anomaly in the monsoon season and corresponding PC time series are presented in Figs. 3.9 and 3.10, respectively. The first CSLV is characterized by strong positive precipitation anomalies in the northern region of the BOB in 0600–1500 LST and in the southeastern region of Bangladesh in 1200–1500 LST. The precipitation anomaly in the northern region of the BOB starts to develop in 0000–0300 LST, peaks in 0600–0900 LST, and is weakened in 1200–1500 LST, exhibiting a clear diurnal cycle. The PC time series of the first CSEOF mode has small values in most of the time, but its values soars at some specific times. This means that this mode is strongly activated occasionally but

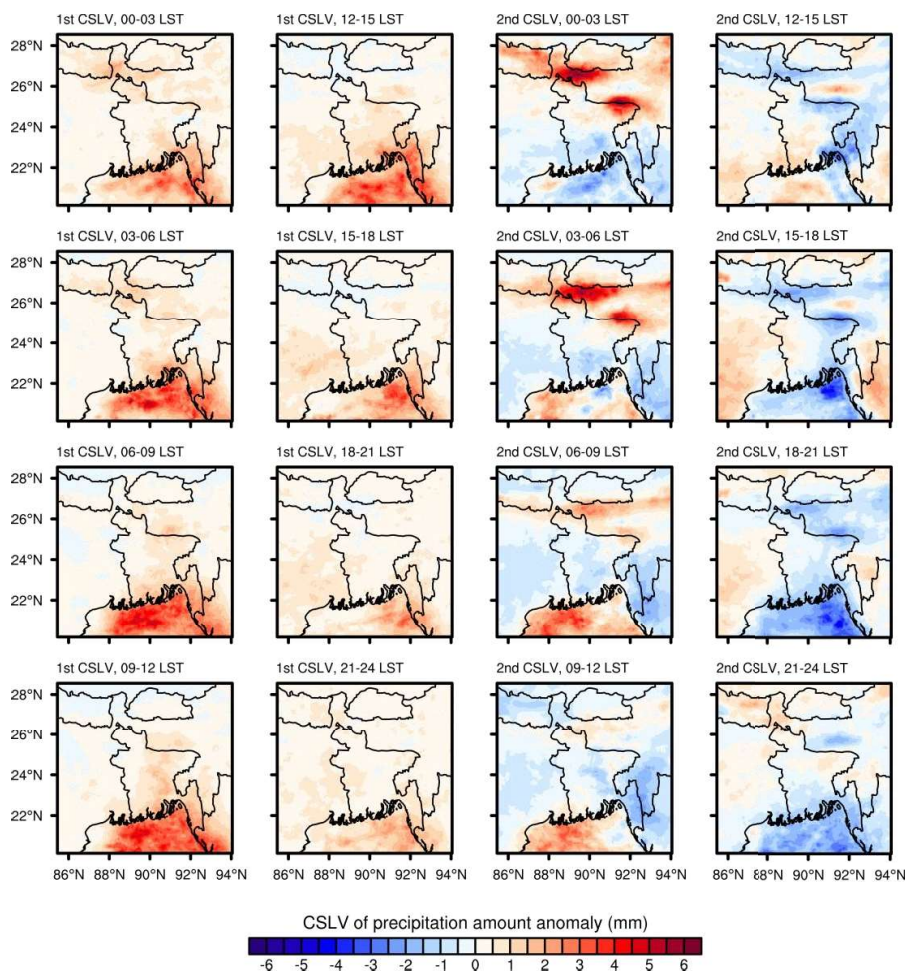


Figure 3.9 As in Fig. 3.6, but for precipitation amount anomaly in the monsoon season.

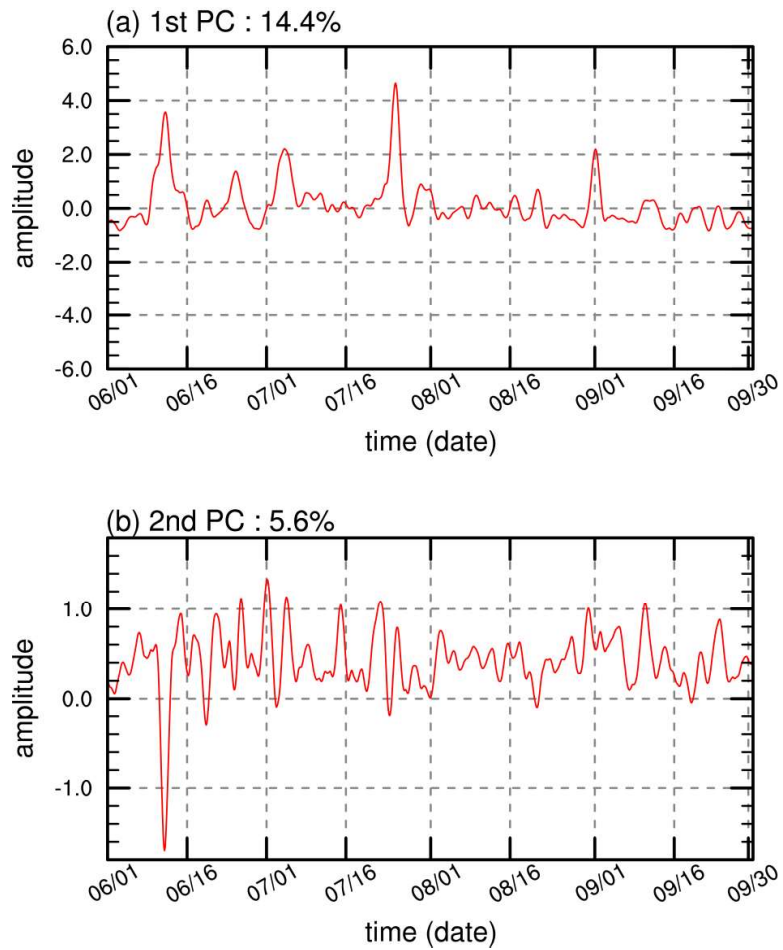


Figure 3.10 As in Fig 3.7, but for precipitation amount anomaly in the monsoon season.

deactivated ordinarily. The first mode contributes 14.4% to the total variance of the monsoonal precipitation.

The second CSLV is characterized by strong positive precipitation anomalies in the northeastern region of Bangladesh and the southern slopes of the Meghalaya Plateau and Himalayan Foothills in 0000–0600 LST and in the northwestern region of the BOB in 0600–1200 LST. In the southwestern region of Bangladesh, the precipitation anomaly peaks in 1200–1500 LST. The precipitation anomaly peaks in the Arakan Mountains in 1500–1800 LST. The PC time series of the second CSEOF mode is in a positive phase in most of the time in the monsoon season. The peak times of precipitation anomalies in the northern and southwestern regions of Bangladesh roughly match with the peak times of monsoonal precipitation in these regions (Chapter 2). In 1500–1800 LST, the precipitation anomalies in the southeastern coastal region of Bangladesh and the nearby region close to the Arakan Mountains show a big contrast. This difference is confirmed by both the IMERG and rain gauge data (not shown). The high spatial resolution of the IMERG data can play an important role in identifying such a big contrast in the region where rain gauge stations are sparsely distributed. The second mode contributes 5.6% to the total variance of the monsoonal precipitation.

The fields of diurnal variations of CSLVs of 900-hPa water vapor flux anomaly regressed to the first and second modes of the monsoonal precipitation anomaly are presented in Fig. 3.11. Note that the mean 900-hPa water vapor flux in the monsoon season is southwesterly in the northern region of the BOB and mainly southerly in Bangladesh (Chapter 2). In the first regressed mode, a strong westerly water vapor flux anomaly prevails in the northern region of the BOB and it is deflected northward by the

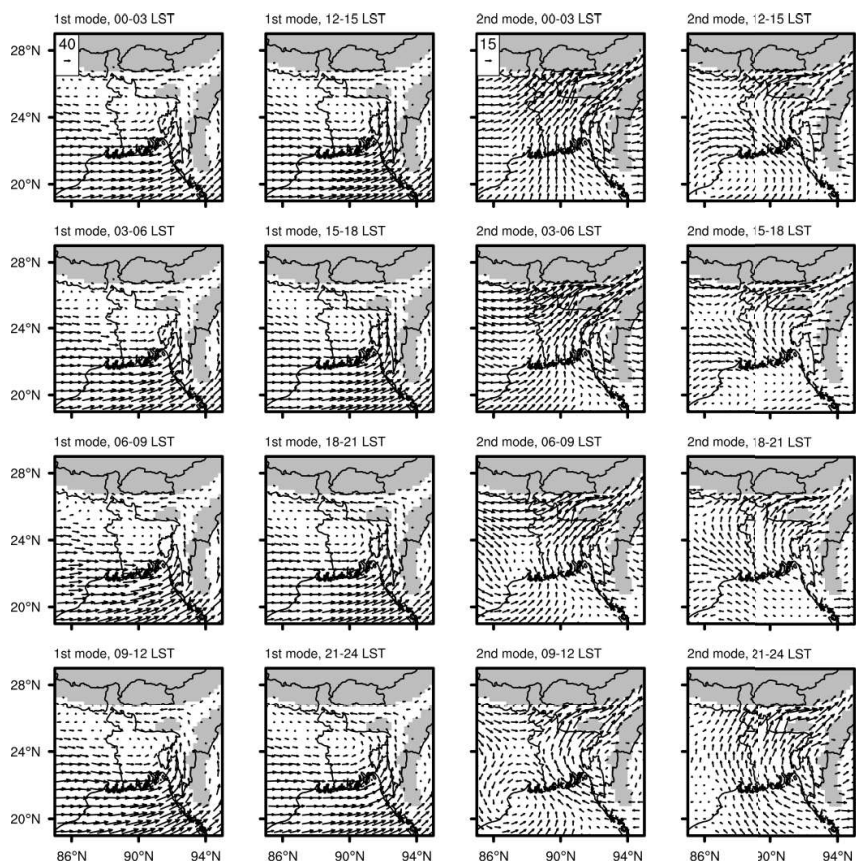


Figure 3.11 As in Fig. 3.8, but for in the monsoon season.

Arakan Mountains. The spatial patterns of water vapor flux anomaly in this mode do not show a strong diurnal variation. The magnitude of water vapor flux anomaly in the northern region of the BOB is largest in 0900–1200 LST, and the convergence of water vapor flux anomaly in the southeastern region of Bangladesh is largest in 1200–1500 LST (not shown). This indicates that if a strong westerly anomaly prevails in the northern region of the BOB, the moist wind climbs the slope of the Arakan Mountains, piling moisture in the southeastern region of Bangladesh and resulting in maximum precipitation anomaly there in 1200–1500 LST. The peak time of precipitation anomaly in the northern region of the BOB agrees with that of the magnitude of 900-hPa water vapor flux in the northern region of the BOB. This characteristic moisture transport pattern occasionally occurs in the monsoon season (Fig. 3.10a), enhancing precipitation in the northern region of the BOB and the southeastern region of Bangladesh.

The second regressed mode shows a relatively strong diurnal variation of the spatial patterns of water vapor flux anomaly. A strong southwesterly water vapor flux anomaly is directed toward the southern slopes of the Meghalaya Plateau and Himalayan Foothills in 0000–0600 LST. Taking into account that the mean water vapor flux in the monsoon season is southerly, the strong southwesterly water vapor flux anomaly in the nighttime makes a large amount of moisture directly reach the southern slopes of the Meghalaya Plateau and Himalayan Foothills without facing any other orographic obstacles (e.g., the Arakan Mountains), which results in the strong positive precipitation anomalies in these regions in 0000–0600 LST in this mode. After ~0600 LST, a cyclonic circulation anomaly centered in the northwestern region of the BOB develops and it weakens the water vapor flux heading toward the southern slopes of the Meghalaya

Plateau and Himalayan Foothills, which can be associated with the weakened precipitation anomalies in these regions in this time, as shown in Fig. 3.9. An ascending motion produced by this cyclonic circulation anomaly could be suggested as a driving mechanism for the strong positive precipitation anomaly in the northwestern region of the BOB in 0600–1200 LST. From ~1500 LST, the cyclonic circulation anomaly disappears, making precipitation in the northwestern region of the BOB reduced.

Fujinami et al. (2017) reported that precipitation around the Meghalaya Plateau in the monsoon season can be classified into easterly and westerly regimes of the intra-seasonal oscillation, determined by the low-level wind direction in the windward region of the plateau. The precipitation and wind patterns of the first and second modes in the monsoon season are very similar to those of the easterly and westerly regimes in Fujinami et al. (2017), respectively. The connection between the first two CSEOF modes and the two different regimes of the intra-seasonal oscillation deserves a further investigation.

In addition to the CSEOF analysis on the IMERG data in Bangladesh and surrounding region, the EOF analysis is also conducted. For both the pre-monsoon and monsoon seasons, the first two EOF modes explain slightly larger portions of the total variance of precipitation compared to the first two CSEOF modes (0.2–2.9 percentage point). The EOF loading vector for each mode is fixed with time, unlike the CSLV that varies within the nested period. The EOF loading vector pattern for each mode is very similar to the CSLV pattern for that mode in the time when the signal is maximized (not shown). Because the EOF analysis does not show any new aspect that is not shown by the CSEOF analysis, only the CSEOF analysis results are given in this study.



## 4 Development of a physically based raindrop-cloud droplet accretion parameterization and its evaluation through cloud and precipitation simulations

### 4.1 A new accretion parameterization

In this section, a new accretion parameterization is derived. The rate of change in the number concentration of raindrops through the accretion of cloud droplets is described using the SCE:

$$\begin{aligned} \frac{\partial f_r(m)}{\partial t} = & \int_0^m f_r(m-m')K(m-m',m')f_c(m')dm' \\ & - \int_0^\infty f_r(m)K(m,m')f_c(m')dm', \end{aligned} \quad (4.1)$$

where  $f_r(m)dm$  and  $f_c(m)dm$  are the number concentrations of raindrops and cloud droplets in the mass interval  $[m, m+dm]$ , respectively, and  $K$  is the collection kernel. Proper rearrangements and substitutions give a simple form of Eqs. (4.1) using radii of colliding raindrops and cloud droplets (e.g., Jin et al. 2019):

$$\left. \frac{\partial L_r}{\partial t} \right|_{\text{acc}} = \frac{4}{3} \pi \rho_w \int_0^\infty \int_0^\infty r^3 f_r(R)K(R,r)f_c(r)drdR, \quad (4.2)$$

where  $L_r$  is the mass content of rainwater,  $R$  and  $r$  are the radii of raindrops and cloud droplets, respectively, and  $\rho_w$  is the density of liquid water. The subscript “acc” refers to the accretion process.

In many bulk microphysics schemes, the size distributions of raindrops and cloud droplets are represented by a three-parameter gamma distribution function (e.g., Walko et al. 1995; Milbrandt and Yau 2005; Thompson et al. 2008; Morrison and Milbrandt 2015):

$$f_r(R) = N_{0,r} R^{\mu_r} \exp(-\lambda_r R), \quad (4.3a)$$

$$f_c(r) = N_{0,c} r^{\mu_c} \exp(-\lambda_c r), \quad (4.3b)$$

where  $N_{0,r}$  and  $N_{0,c}$  are the intercept parameters,  $\mu_r$  and  $\mu_c$  are the shape parameters, and  $\lambda_r$  and  $\lambda_c$  are the slope parameters. In a double-moment bulk microphysics scheme, the shape parameter should be preset or diagnosed if the other two parameters are prognosed.  $\mu_r$  can be set to any constant value or diagnosed using empirical relations (e.g., Cao et al. 2008), but it is set to 0, which yields a traditional exponential size distribution for raindrops, in this study.  $\mu_c$  is diagnosed by an empirical relation  $\mu_c = \min[15, \text{nint}(10^9/N_c + 2)]$  following Thompson et al. (2008), where  $N_c$  is the number concentration of cloud droplets ( $\text{m}^{-3}$ ) and  $\text{nint}(x)$  refers to the nearest integer of  $x$ .

The collection kernel  $K$  in Eqs. (4.2) is given by

$$K(R, r) = \pi(R + r)^2 |v_{t,r}(R) - v_{t,c}(r)| \eta, \quad (4.4)$$

where  $v_{t,r}$  and  $v_{t,c}$  are the terminal velocities of raindrops and cloud droplets, respectively

and  $\eta$  is the collection efficiency. The empirical relation of Beard (1976) is a widely-used representation of the terminal velocity of liquid water drops (e.g., Pinsky et al. 2001; Khain et al. 2011). Because the empirical relation consists of three different expressions for different size ranges and the expressions are complicated, simpler forms of terminal velocities for raindrops and cloud droplets can be obtained for direct use in a bulk microphysics scheme by nonlinear curve fitting using the terminal velocity relation of Beard (1976) as the reference. The terminal velocity relation for cloud droplets obtained using this method in LB17 and a newly obtained terminal velocity relation for raindrops are given as

$$v_{t,r} = v_{0,r} [1 - \exp(-\gamma_r R)], \quad (4.5)$$

$$v_{t,c} = v_{0,c} r^2, \quad (4.6)$$

respectively. Here, the values of  $v_{0,r}$ ,  $\gamma_r$ , and  $v_{0,c}$  are 9.770, 1097, and  $1.0973 \times 10^8$ , respectively, and  $v_{t,r}$  and  $v_{t,c}$  are in meters per second and  $R$  and  $r$  are in meters. The obtained terminal velocity relation of raindrops is quite different from the power-law relation that is commonly used in bulk microphysics schemes (Morrison et al. 2005; Lim and Hong 2010). The power-law relation has an advantage in its simplicity, but its estimation is only valid for a limited size range of raindrops, beyond which a serious deviation takes place (Seifert et al. 2014). If the raindrop terminal velocity is expressed by the asymptotic function, it does not deviate much from realistic values. Figure 4.1 shows the obtained terminal velocities of raindrops and cloud droplets. Both the terminal velocities agree well with the empirical relation of Beard (1976), except for the

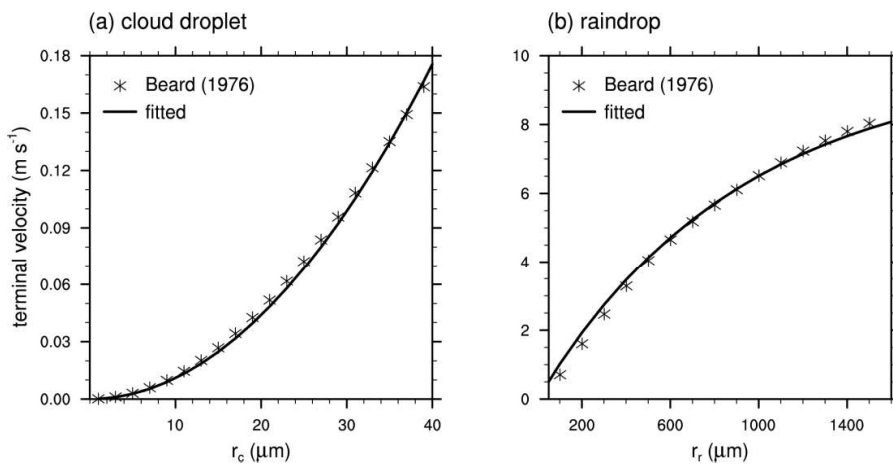


Figure 4.1 Terminal velocities of (a) cloud droplets (Lee and Baik 2017) and (b) raindrops. The star symbols indicate the terminal velocities from Beard (1976), and the solid lines are the fitted equations.

overestimation of terminal velocity of very small raindrops (bias of  $0.33 \text{ m s}^{-1}$  for a raindrop with radius of  $200 \text{ }\mu\text{m}$ ) and the underestimation of terminal velocity of very large raindrops (bias of  $0.15 \text{ m s}^{-1}$  for a raindrop with radius of  $1500 \text{ }\mu\text{m}$ ). In addition, the density factor  $(\rho_0/\rho)^{1/2}$ , where  $\rho_0$  is the reference air density and  $\rho$  is the air density, is multiplied to consider the increase of terminal velocity with the decrease of air density.

The collection efficiency in Eqs. (4.4) is given as the product of the collision efficiency and the coalescence efficiency. The coalescence efficiency between large drops and small droplets has not been studied well and has some uncertainty. Beard and Ochs (1995) showed that the estimated coalescence efficiency based on different laboratory experiments can vary much. However, in this study, the coalescence efficiency is assumed to be unity, following the extrapolation of a coalescence efficiency parameterization based on the direct numerical simulation (DNS) results by Straub et al. (2010). This seems justifiable because the coalescence efficiency approaches to 1 as the Weber number decreases in Straub et al. (2010); the Weber number is very small in the accretion regime. The assumption of the coalescence efficiency of 1 yields that the collection efficiency is identical to the collision efficiency.

Pinsky et al. (2001) performed a detailed study on the collision efficiency using a particle trajectory model and provided the tabulated collision efficiency between raindrops and cloud droplets of various sizes. A limitation of the collision efficiency of Pinsky et al. (2001) is that the maximum radius of raindrops considered is limited to  $300 \text{ }\mu\text{m}$ , because of the challenges associated with describing flow fields around particles for Reynolds numbers greater than 100. The collision efficiency between relatively larger raindrops ( $\sim 600 \text{ }\mu\text{m}$ ) and micron-size cloud droplets is provided by Beard and Grover

(1974). The collision efficiency of Beard and Grover (1974) is not as reliable as that of Pinsky et al. (2001) because the effects of the flow fields around collected drops on the motion of collecting drops are not considered in their study, but it gives a valid estimation for the collision between large raindrops and small cloud droplets. A careful inspection of the collision efficiency of Pinsky et al. (2001) for small raindrops and that of Beard and Grover (1974) for relatively large raindrops colliding with micron-size cloud droplets suggests that the collision efficiency is represented well by the following function:

$$\eta = b_0 [1 - \exp(-b_1 r)] [1 - \exp(-b_2 R - b_3 r)]. \quad (4.7)$$

A nonlinear fitting using a damped least-squares method to the combination of the two reference collision efficiencies gives the coefficients; the determined values of  $b_0$ ,  $b_1$ ,  $b_2$ , and  $b_3$  are 1, 246642 m<sup>-1</sup>, 3803 m<sup>-1</sup>, and 144650 m<sup>-1</sup>, respectively. Note that the collision efficiency of Pinsky et al. (2001) is considered with a greater weighting to obtain the fitted function because of the greater reliability of the data.

The fitted collision efficiency and its deviation from the reference collision efficiency of Pinsky et al. (2001) and Beard and Grover (1974) are shown in Fig. 4.2. Overall, the fitted collision efficiency agrees well with the reference collision efficiency. The collision efficiency for  $r < 4 \mu\text{m}$  is slightly overestimated, but the gamma size distribution of cloud droplets yields very small number of cloud droplets in this size range. Thus, the overestimation does not affect the accretion rate significantly except when the number of the very small droplets is unusually large. For a given size of small cloud droplets, the fitted collision efficiency continuously increases as the raindrop

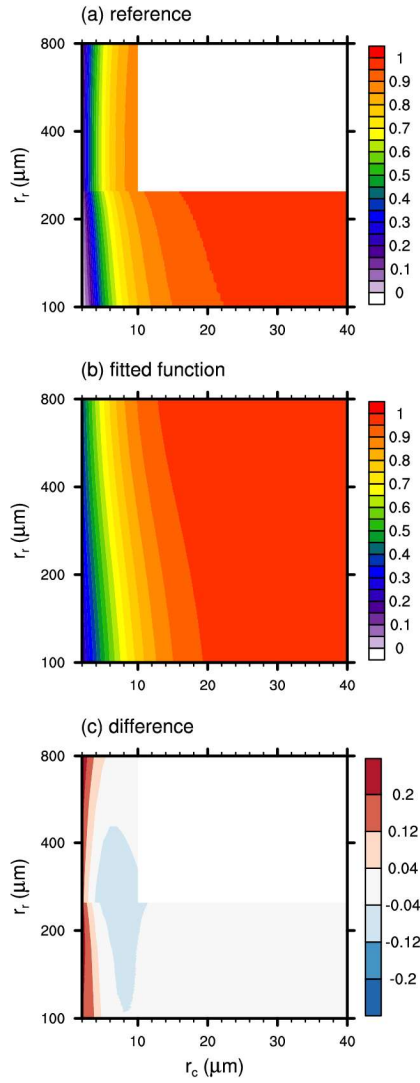


Figure 4.2 (a) The reference collision efficiency between raindrops and cloud droplets which is a combination of the collision efficiencies of Pinsky et al. (2001) and Beard and Grover (1974). (b) The fitted collision efficiency and (c) the fitted collision efficiency minus the reference collision efficiency.

size increases, following the tendency in the collision efficiency of Pinsky et al. (2001).

Using the above expressions for the size distributions, terminal velocities, and collision efficiency, the analytic expression of Eqs. (4.2) can be obtained. Here, the only problem is the absolute value in the collection kernel which makes the analytic integration in Eqs. (4.2) challenging. To overcome this problem, an approximation by Gaudet and Schmidt (2005) is employed, where the absolute value of the difference in terminal velocity is approximated as the difference itself. As in Jin et al. (2019), box model simulations using a bin-based direct SCE solver confirms that this approximation hardly changes the accretion rate. Then, the accretion rate given by the analytic expression of Eqs. (4.2) is

$$\left. \frac{\partial L_r}{\partial t} \right|_{\text{acc}} = \frac{4}{3} \pi^2 \rho_w \left( \frac{\rho_0}{\rho} \right)^{1/2} N_{0,r} N_{0,c} b_0 (v_{0,r} L_1 - v_{0,c} L_2), \quad (4.8)$$

where

$$\begin{aligned} L_1 = \sum_{i=0}^2 a_i \{ & [\Gamma_1(\lambda_r, \mu_r + 3 - i) - \Gamma_1(\lambda_r + \gamma_r, \mu_r + 3 - i)] \\ & \times [\Gamma_1(\lambda_c, \mu_c + 4 + i) - \Gamma_1(\lambda_c + b_1, \mu_c + 4 + i)] \\ & - [\Gamma_1(\lambda_r + b_2, \mu_r + 3 - i) - \Gamma_1(\lambda_r + b_2 + \gamma_r, \mu_r + 3 - i)] \\ & \times [\Gamma_1(\lambda_c + b_3, \mu_c + 4 + i) - \Gamma_1(\lambda_c + b_1 + b_3, \mu_c + 4 + i)] \}, \end{aligned} \quad (4.9a)$$

$$\begin{aligned} L_2 = \sum_{i=0}^2 a_i \{ & \Gamma_1(\lambda_r, \mu_r + 3 - i) \\ & \times [\Gamma_1(\lambda_c, \mu_c + 6 + i) - \Gamma_1(\lambda_c + b_1, \mu_c + 6 + i)] \\ & - [\Gamma_1(\lambda_r + b_2, \mu_r + 3 - i) \\ & \times [\Gamma_1(\lambda_c + b_3, \mu_c + 6 + i) - \Gamma_1(\lambda_c + b_1 + b_3, \mu_c + 6 + i)]] \}, \end{aligned} \quad (4.9b)$$



with  $a_i$  given as  $(a_0, a_1, a_2) = (1, 2, 1)$ .  $\Gamma_1(\lambda, s)$  is defined as

$$\Gamma_1(\lambda, s) = \frac{\Gamma(s)}{\lambda^s}, \quad (4.10)$$

where  $\Gamma$  is the gamma function and  $s > 0$ . The variation of the size distribution parameters that represents the variation of the cloud droplet and raindrop size distributions yields the variation of the accretion rates. Mass conservation yields the following relation:

$$\left. \frac{\partial L_c}{\partial t} \right|_{\text{acc}} = - \left. \frac{\partial L_r}{\partial t} \right|_{\text{acc}}, \quad (4.11)$$

where  $L_c$  is the mass content of cloud water.

The rate of change in the cloud droplet number concentration due to the accretion process is given by

$$\left. \frac{\partial N_c}{\partial t} \right|_{\text{acc}} = - \int_0^\infty \int_0^\infty f_r(R) K(R, r) f_c(r) dr dR. \quad (4.12)$$

Following the procedure of obtaining the analytic expression of the accretion rate Eqs. (4.8–4.9), one can show that Eqs. (4.12) is expressed as follows:

$$\left. \frac{\partial N_c}{\partial t} \right|_{\text{acc}} = -\pi \left( \frac{\rho_0}{\rho} \right)^{1/2} N_{0,r} N_{0,c} b_0 (v_{0,r} N_1 - v_{0,c} N_2), \quad (4.13)$$

where

$$\begin{aligned} N_1 = \sum_{i=0}^2 a_i \{ & [\Gamma_1(\lambda_r, \mu_r + 3 - i) - \Gamma_1(\lambda_r + \gamma_r, \mu_r + 3 - i)] \\ & \times [\Gamma_1(\lambda_c, \mu_c + 1 + i) - \Gamma_1(\lambda_c + b_1, \mu_c + 1 + i)] \\ & - [\Gamma_1(\lambda_r + b_2, \mu_r + 3 - i) - \Gamma_1(\lambda_r + b_2 + \gamma_r, \mu_r + 3 - i)] \\ & \times [\Gamma_1(\lambda_c + b_3, \mu_c + 1 + i) - \Gamma_1(\lambda_c + b_1 + b_3, \mu_c + 1 + i)] \}, \end{aligned} \quad (4.14a)$$

$$\begin{aligned} N_2 = \sum_{i=0}^2 a_i \{ & \Gamma_1(\lambda_r, \mu_r + 3 - i) \\ & \times [\Gamma_1(\lambda_c, \mu_c + 3 + i) - \Gamma_1(\lambda_c + b_1, \mu_c + 3 + i)] \\ & - \Gamma_1(\lambda_r + b_2, \mu_r + 3 - i) \\ & \times [\Gamma_1(\lambda_c + b_3, \mu_c + 3 + i) - \Gamma_1(\lambda_c + b_1 + b_3, \mu_c + 3 + i)] \}. \end{aligned} \quad (4.14b)$$

The raindrop number concentration is not affected by the accretion process.

Note that the existence of the terms  $v_{0,c} L_2$  in Eqs. (4.8) and  $v_{0,c} N_2$  in Eqs. (4.13) stems from the consideration of the cloud droplet terminal velocity in the collection kernel. The advantage of this consideration in the accretion rate estimation is relatively small compared to the advantages of considering the contribution of cloud droplets to the geometric sweep-out area or the individual drop size-dependent collection efficiency instead of the bulk collection efficiency. Also, the bias in the estimated accretion rate caused by ignoring the cloud droplet terminal velocity is small compared to that caused by the overestimation of the terminal velocity of very small raindrops in the fitted function, except for when the mean cloud droplet size is very large. For the cost-

efficiency in modeling,  $v_{0,c}L_2$  in Eqs. (4.8) and  $v_{0,c}N_2$  in Eqs. (4.13) can be neglected. In this study, however, the full equations are used for the evaluation of the developed parameterization.

## 4.2 Evaluation through cloud-resolving model simulations

The developed accretion parameterization is evaluated through idealized and real-case simulations using a cloud-resolving model. For this, the Weather Research and Forecasting (WRF) model version 3.9.1 (Skamarock et al. 2008) is used. The Thompson–Eidhammer microphysics scheme (Thompson and Eidhammer 2014) is selected as a microphysics scheme, and the developed accretion parameterization is implemented into the Thompson–Eidhammer microphysics scheme while the parameterizations of other microphysical processes are unchanged. The Thompson–Eidhammer microphysics scheme uses gamma distribution functions to represent the size distributions of cloud droplets and raindrops, as assumed in the new parameterization. The original parameterization of the accretion of cloud water by rainwater in the Thompson–Eidhammer microphysics scheme is based on the continuous collection equation that neglects the contribution of the size distribution and terminal velocity of cloud droplets to the accretion rate. In addition, the original parameterization mainly adopts the collision efficiency of Beard and Grover (1974) as a bulk collection efficiency which is determined by mean raindrop and cloud droplet radii. In contrast, the new parameterization considers the contribution of cloud droplets to the relative terminal velocity and geometric sweep-out area in the collection kernel (Eqs. 4.4) and uses the individual drop size-dependent collection efficiency instead of the bulk collection efficiency. Also, the collision

efficiency is fitted from a combination of the collision efficiency of Pinsky et al. (2001) and that of Beard and Grover (1974), which yields greater value compared to when only the collision efficiency of Beard and Grover (1974) is used. In the following subsections, simulations with the original accretion parameterization are also conducted and compared to those with the new accretion parameterization. Hereafter, the new and original parameterizations are called NP and OP, respectively.

#### **4.2.1 Idealized simulations**

Idealized 2D mixed-phase deep convective clouds are simulated using the WRF model. The horizontal domain size is 80 km with a grid spacing of 200 m, and the vertical domain size is 20 km with grid spacings ranging from ~180 m to ~230 m. At lateral boundaries, the open boundary condition is applied. The sponge layer is located from  $z = 15$  km to the domain top. The model is integrated for 120 min with a time step of 2 s.

A composite thermodynamic sounding averaged over June 2014 at Dhaka radiosonde station (23.76°N, 90.38°E), Bangladesh (Fig. 4.3) is used as the initial condition at every grid point to simulate deep convection. June belongs to the active South Asian monsoon period (June to September). The thermodynamic sounding exhibits a very humid state in the lower atmosphere, with a near-surface water vapor mixing ratio of ~20 g kg<sup>-1</sup>. For the thermodynamic sounding, the lifting condensation level (LCL) is 0.56 km, the level of free convection (LFC) is 1.75 km, and the equilibrium level (EL) is 13.84 km. The convective available potential energy (CAPE) is 1174 J kg<sup>-1</sup>. No basic-state wind is considered in the idealized simulations. The cloud is initiated using a warm-bubble method.

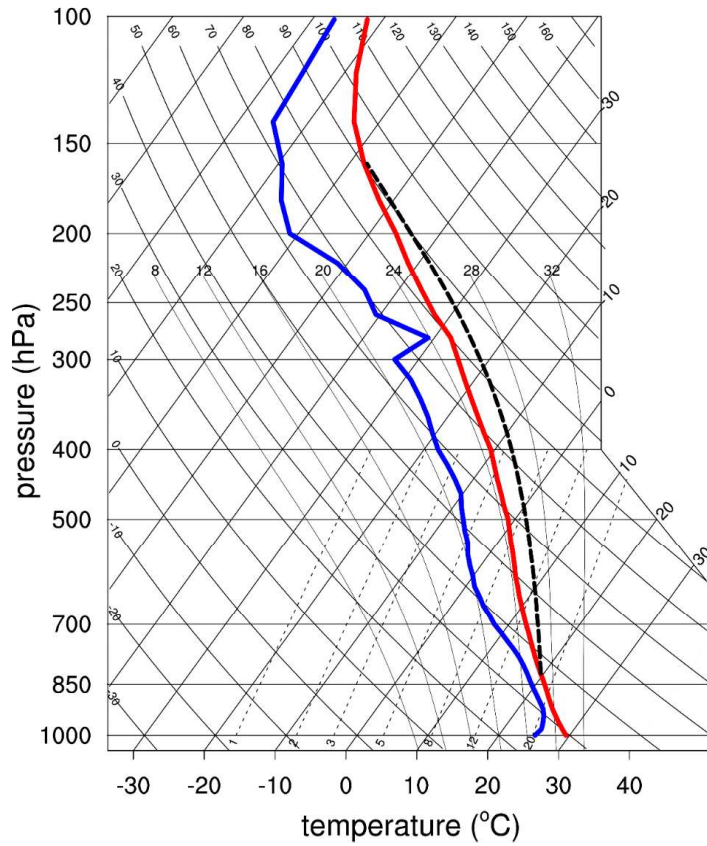


Figure 4.3 Composite of thermodynamic soundings at Dhaka radiosonde station in June 2014. The thick red and blue solid lines indicate the temperature and dew point temperature, respectively, and the thick black dashed line indicates the temperature of air parcel lifted moist-adiabatically from the level of free convection.

To examine the impacts of the new accretion parameterization on precipitation, the time series of domain-averaged accumulated surface precipitation amount and surface precipitation rate in NP and OP are compared (Fig. 4.4). In this subsection, the domain average is taken horizontally over 20 km (within  $\pm 10$  km from the domain center). The range of the domain average in the  $x$ -direction is chosen considering the maximum horizontal extent of the main clouds in the simulations. The surface precipitation (precipitation rate greater than  $0.1 \text{ mm h}^{-1}$ ) starts at 24 min in NP and 26 min in OP. The earlier onset of surface precipitation in NP (2 min earlier) is due to the relatively large accretion rate in NP, which will be shown later. The accumulated surface precipitation amount is consistently larger in NP than in OP until the end of the time integration (Fig. 4.4a). At  $t = 120$  min, the accumulated surface precipitation amount in NP is 12% larger than that in OP. The surface precipitation rate is larger in NP than in OP, except for  $t = 35\text{--}39$  min and  $54\text{--}58$  min (Fig. 4.4b). The first peak of the surface precipitation rate appears earlier in NP ( $t = 35$  min) than in OP ( $t = 36$  min), but its value is smaller in NP ( $5.8 \text{ mm h}^{-1}$ ) than in OP ( $8.6 \text{ mm h}^{-1}$ ).

Figure 4.5 shows the time- and domain-averaged vertical profiles of hydrometeor mixing ratios and mass-weighted mean radii of cloud droplets and raindrops. The simulated cloud is vertically well developed with a maximum updraft velocity of  $12.5 \text{ m s}^{-1}$ , and the cloud top reaches  $z = 12.5$  km in NP. Due to effective conversion of cloud water into rainwater, the rainwater mixing ratio is much larger than the cloud water mixing ratio at  $z \sim 1.5\text{--}6.2$  km (Fig. 4.5a). From  $z = 5.0$  km, a little below the freezing-level height ( $z = 5.6$  km), a large amount of snow exists up to the cloud top, and graupel also exists from  $z = 4.0$  km to the cloud top in NP. Compared to OP, NP exhibits a larger

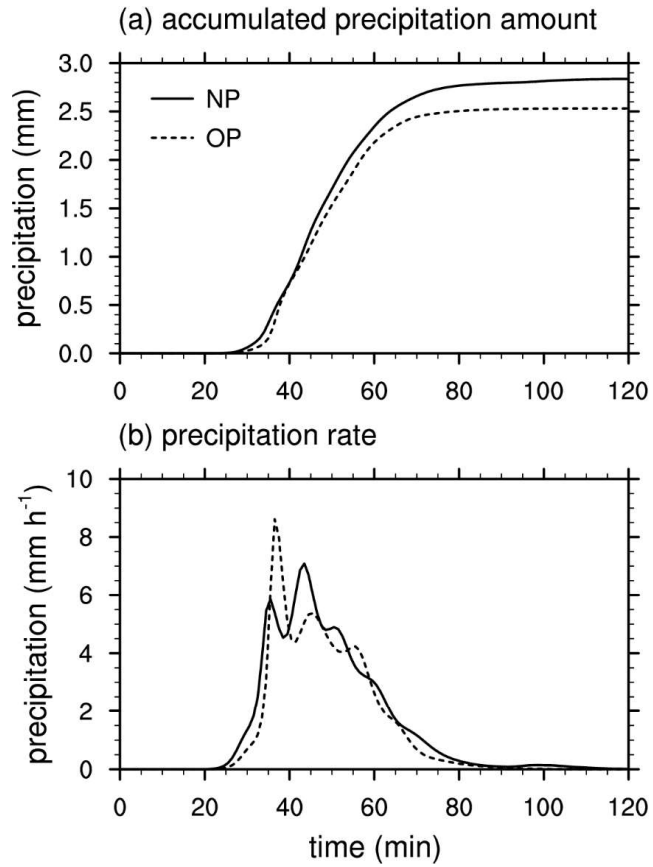


Figure 4.4 Time series of domain-averaged (a) accumulated surface precipitation amount and (b) surface precipitation rate in the idealized simulations with the new and original accretion parameterizations.

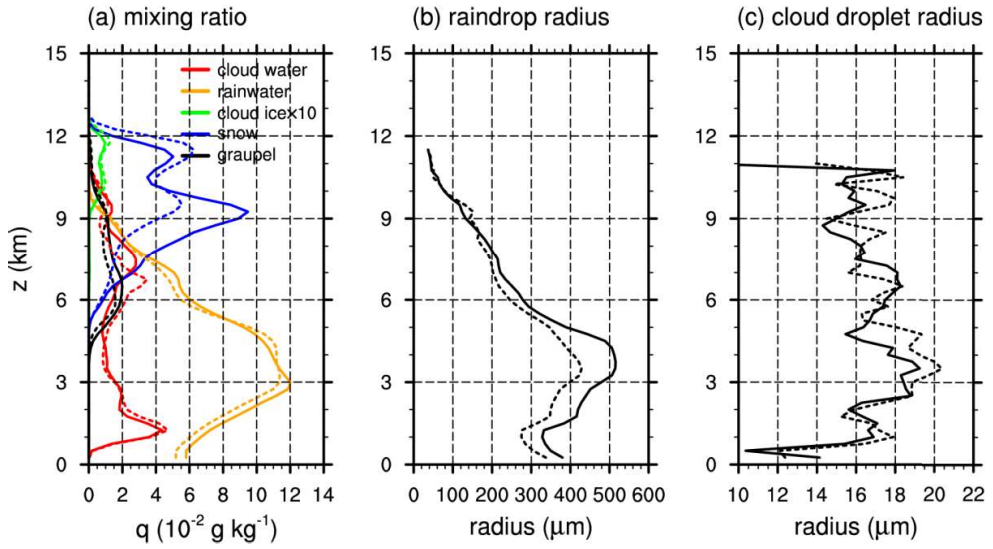


Figure 4.5 Time- and domain-averaged vertical profiles of (a) hydrometeor mixing ratios and mass-weighted mean radii of (b) raindrops and (c) cloud droplets in the idealized simulations with the new (solid lines) and original (dashed lines) parameterizations.



rainwater mixing ratio at most levels except for  $z = 3.6\text{--}5.3$  km, while it predicts a smaller cloud water mixing ratio at  $z = 0.3\text{--}2.6$  km and  $z = 4.4\text{--}7.0$  km. The snow mixing ratio in NP is much larger than that in OP at  $z = 6.5\text{--}10$  km, about 94% on average. NP also shows a greater graupel mixing ratio up to  $z = 9.2$  km. However, the contribution of the melting process to the production of rainwater mass is relatively small compared to that of the accretion process in these simulations. One of the most prominent differences between NP and OP is shown in the mass-weighted mean radius of raindrops (Fig. 4.5b). The mean raindrop radius in NP is larger than that in OP up to  $z = 8.5$  km. Especially at  $z = 2.0\text{--}5.0$  km, NP exhibits 22% larger mean raindrop radius on average compared to OP. The faster sedimentation of larger-sized raindrops in NP acts as a greater sink of rainwater mass. The smaller rainwater mixing ratio in NP at  $z = 3.6\text{--}5.3$  km does not indicate that the production processes of rainwater such as the accretion process are relatively weak in NP, but results from the stronger sedimentation process in NP. The time-averaged downward mass flux of rainwater at  $z = 3.6\text{--}5.3$  km is larger in NP than in OP (not shown). In contrast, the mean cloud droplet radius in NP is smaller than that in OP at most levels below  $z = 5.2$  km where the rainwater mixing ratio is large (Fig. 4.5c). The overall larger mean raindrop radius and smaller mean cloud droplet radius in NP still appear when they are averaged only over  $t \leq 40$  min during which no ice hydrometeors are present (not shown).

To understand the roles of microphysical processes in the above findings, the time series of domain-averaged accretion and autoconversion rates are shown in Fig. 4.6. Here, the domain average is taken not only horizontally as in Fig. 4.4 but also vertically over  $z = 0\text{--}15$  km;  $z = 15$  km is the bottom height of the sponge layer. The accretion process

arises at  $t = 13$  min in both simulations (Fig. 4.6a). Since then, NP predicts 56% larger accretion rate on average until  $t = 20$  min, compared to OP; this difference looks smaller than its actual value because the accretion rate increases steeply during this time. The difference in the accretion rates becomes smaller and again increases, and the accretion rate in NP remains larger than that in OP until  $t = 52$  min. An opposite tendency is predicted when it comes to the autoconversion rates (Fig. 4.6b). As a larger amount of cloud water mass is converted into rainwater through the accretion process in NP, the cloud water mass to be converted into rainwater through the autoconversion process decreases. The sum of the accretion and autoconversion rates is the total rainwater production rate via the warm-rain microphysical processes. Up to  $t = 32$  min, the summed rate for NP is not so different from the summed rate for OP; almost the same amount of rainwater mass is produced during this period because the difference in the autoconversion rate between NP and OP largely cancels out the difference in the accretion rate between NP and OP (Fig. 4.6c). The difference in the sum of the two rates that arises after  $t = 32$  min suggests that there is more cloud water supply in NP possibly driven by other microphysical and dynamical processes, which will be investigated further in this subsection.

The ratio of the accretion rate to the autoconversion rate (acc/auto ratio) is over 10 in NP during  $t = 21$ – $52$  min, the relatively convective period (Fig. 4.6d). In this study, the acc/auto ratio is calculated for every time step as the ratio between the accretion and autoconversion rates, and it does not mean the ratio between the accumulated amounts of rainwater produced by the accretion and autoconversion process. Given a similar value of liquid water path (see Fig. 4.7a), NP predicts a much higher acc/auto ratio compared

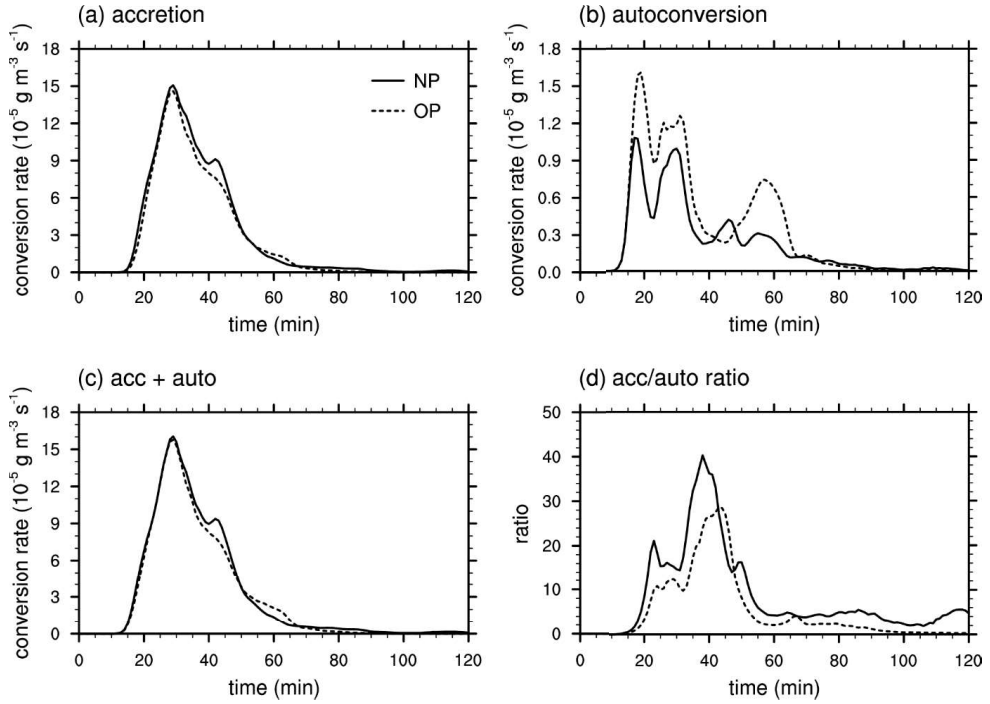


Figure 4.6 Time series of domain-averaged (a) accretion rate, (b) autoconversion rate, (c) the sum of accretion and autoconversion rates, and (d) the ratio between accretion and autoconversion rates in the idealized simulations with the new and original parameterizations.

to OP. The accretion process increases the mean size of raindrops by its own nature. The autoconversion process, however, generally decreases the mean size of raindrops because small-sized raindrops are produced as a result of the process. Therefore, the higher acc/auto ratio in NP is responsible for the larger mean raindrop radius shown in Fig. 4.5b. The increased mean raindrop size results in faster sedimentation. The earlier onset of the precipitation in NP (Fig. 4.4b) can be explained by the larger mean raindrop size in NP caused by the higher acc/auto ratio at the early period.

Figure 4.7 shows the time series of domain-averaged liquid and ice water paths. Here, the liquid water path is the sum of cloud water and rainwater paths, and the ice water path is the sum of cloud ice, snow, and graupel water paths. The two simulations exhibit almost the same values of the liquid water path until  $t \sim 30$  min; the microphysical processes other than the accretion and autoconversion processes do not make any big difference in the liquid water path between the two simulations during this period (Fig. 4.7a). Although slight differences appear after that, the liquid water path in NP remains close to that in OP for the whole period. On the other hand, the ice water path is very different between NP and OP (Fig. 4.7b). Because of the greater mass conversion of cloud water into rain after  $t = 32$  min in NP (Fig. 4.6c), the cloud water mass to be converted into ice hydrometeor through riming decreases in NP, resulting in a slower increase in the ice water path. However, after  $t = 75$  min, NP predicts the noticeably larger (79% on average) ice water path compared to OP. The difference in the ice water path could be induced by the difference in the latent heat release between NP and OP.

Figure 4.8 shows the time- and domain-averaged vertical profiles of latent heating rates and updraft velocity. The condensation and evaporation play important roles at the

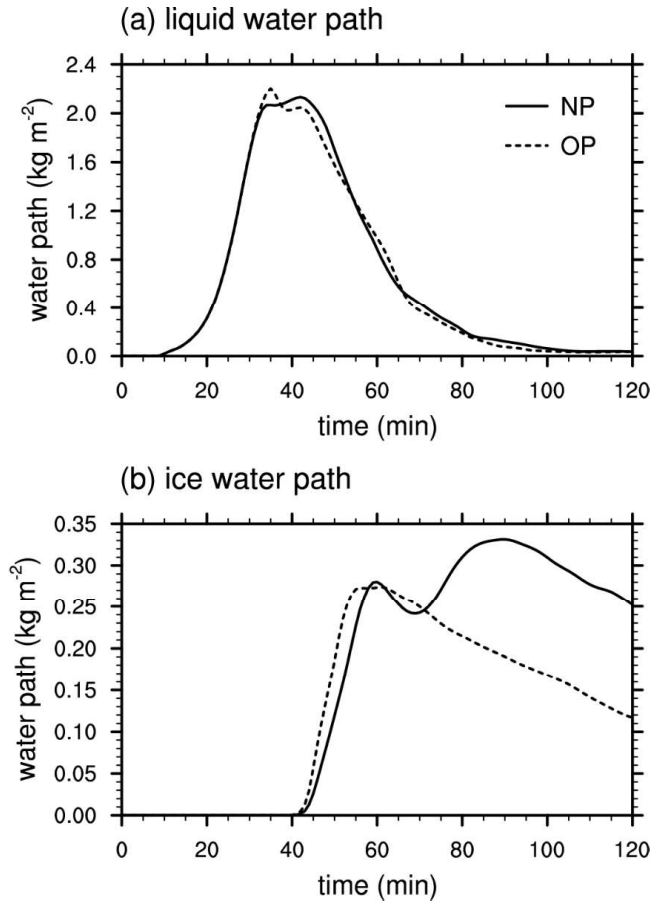


Figure 4.7 Time series of domain-averaged (a) liquid water path and (b) ice water path in the idealized simulations with the new and original parameterizations.

low and middle levels, and the deposition and sublimation contribute most to the heating rates at the high levels (Fig. 4.8a). NP exhibits stronger net latent heating by condensation and evaporation at  $z = 1.6\text{--}4.6$  km (Fig. 4.8b), and this is largely due to weaker evaporation cooling there in NP compared to OP (not shown). The large mean raindrop size in NP yields smaller total surface area of raindrops, which weakens the evaporation. Faster sedimentation in NP due to the larger mean raindrop size reduces the time for raindrops to be evaporated, further weakening the evaporation. The stronger latent heating in NP may enhance the convection. The updraft velocity in NP is overall greater than that in OP up to  $z = 8.9$  km (Fig. 4.8c). The greater updraft velocity in NP transports more water vapor from lower levels to produce more liquid condensates and transports more cloud water to middle and upper levels which can be converted into ice hydrometeors via freezing and riming processes. These may be responsible for the greater rainwater production rate in NP after  $t = 32$  min (Fig. 4.6c) and the greater production rates of the ice hydrometeors in NP (Fig. 4.7b). The greater amount of ice hydrometeors produced in NP can further affect the thermodynamic fields through deposition, sublimation, and riming processes.

To further examine the differences between the two parameterizations, the normalized accretion rates as a function of internal time scale  $\tau$  obtained in the idealized simulations are plotted (Fig. 4.9). The normalized accretion rate is equivalent to the universal function used in Seifert and Beheng (2001, 2006), which is the accretion rate divided by the product of the rainwater content, cloud water content, and a constant. The internal time scale  $\tau$  is the rainwater content divided by the liquid water content, which increases and approaches 1 as the cloud water mass is converted into the rainwater mass.

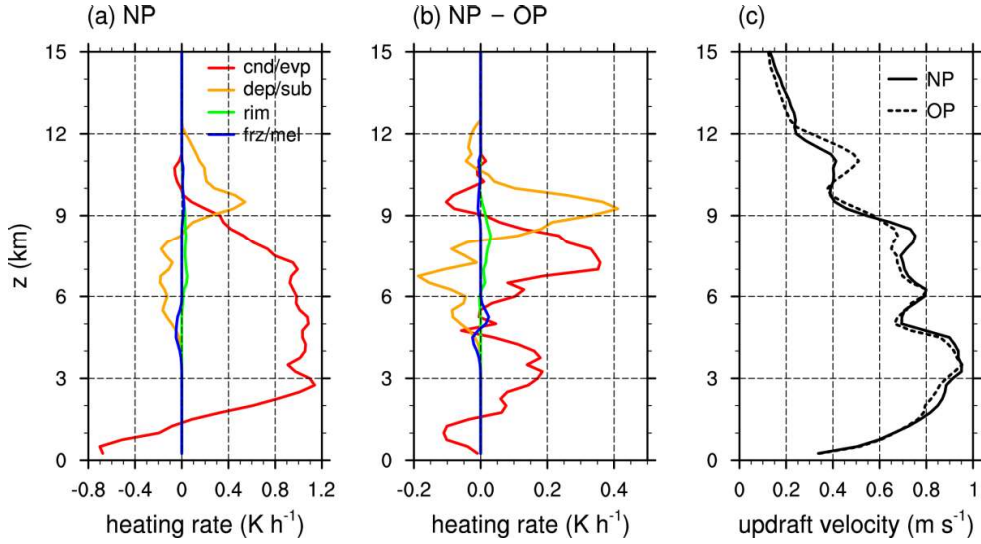


Figure 4.8 Time- and domain-averaged vertical profiles of (a) the heating rates due to condensation/evaporation, deposition/sublimation, riming, and freezing/melting in the idealized simulation with the new parameterization and (b) the differences in the heating rates between the new and original parameterizations. (c) Time- and domain-averaged vertical profiles of updraft velocity ( $w > 0.1 \text{ m s}^{-1}$ ) in the idealized simulations with the new and original parameterizations.

It is noted that in Seifert and Beheng (2001, 2006), the normalized accretion rate is parameterized as a function of  $\tau$  only. The normalized accretion rates in  $t \leq 40$  min and  $t > 40$  min which roughly correspond to the liquid-only phase and mixed phase, respectively (see Fig. 4.7), are marked by different colors.

OP exhibits a dense streak of normalized accretion rates which does not vary much (Fig. 4.9b). Because OP is based on the continuous collection equation where the effects of the differences in the cloud droplet size distribution are not considered, the accretion rate tends to depend mostly on the rainwater and cloud water contents. In NP, however, the normalized accretion rates vary largely with  $\tau$ , and even for the same  $\tau$ , they are widely distributed (Fig. 4.9a). Additionally, the normalized accretion rates in NP show larger values for the liquid-only phase compared to the mixed phase, while those in OP are not distinguishable for the liquid-only phase and the mixed phase. The fact that the normalized accretion rates have various values for the same  $\tau$  suggests that the accretion rate strongly depends on some parameters other than the rainwater and cloud water contents, such as the raindrop and cloud droplet number concentrations, and it may not be appropriate to parameterize the accretion rate with the mass contents only. The relatively rapid increase in the normalized accretion rate with  $\tau$  in NP reflects the relatively rapid increase in the mean raindrop size due to the high acc/auto ratio in NP.

#### **4.2.2 Real-case simulations**

Real-case simulations are performed to evaluate the new accretion parameterization. Heavy rainfall over Bangladesh from 17 to 23 June 2014 is simulated. During this period, a synoptic trough that was at first located over the west side of the



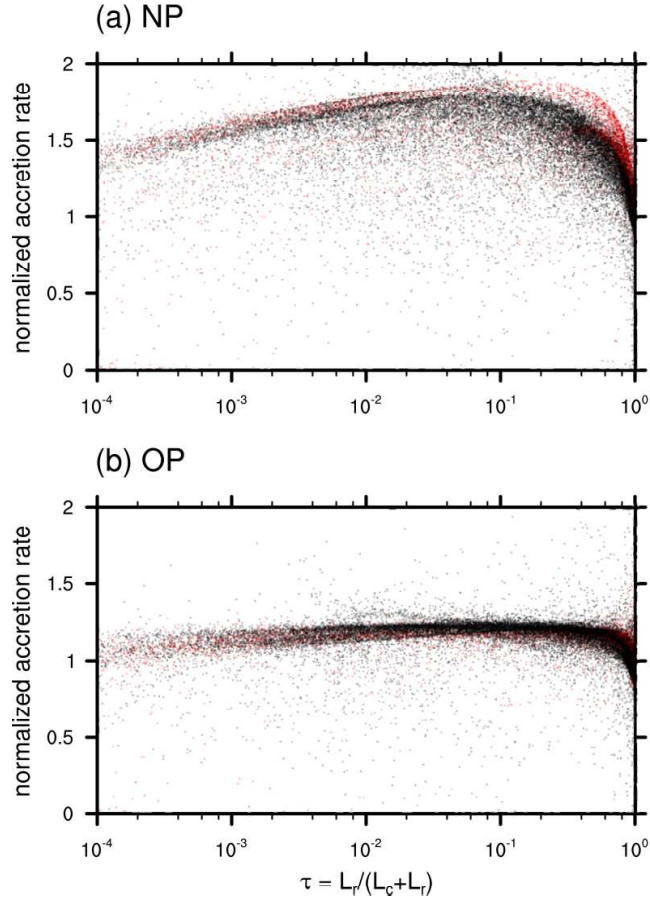


Figure 4.9 Normalized accretion rates as a function of internal time scale  $\tau$  in the idealized simulations with the (a) new and (b) original parameterizations. The red dots correspond to the idealized simulation results for  $t \leq 40$  min, and the black dots correspond to those for  $t > 40$  min.

Bay of Bengal moved northeastward. Monsoonal southwesterly winds transported a large amount of moisture from the Bay of Bengal to Bangladesh, especially to southeastern region which received the heaviest precipitation (see Fig. 4.11c). According to the 35 meteorological stations operated by the Bangladesh Meteorological Department, the maximum 7-day accumulated precipitation amount was 831 mm which was observed at Sandwip (22.48°N, 91.43°E). The precipitation amount for the first two days were small, 9% of the total, while that for the last four days accounts for 77% of the total.

The WRF model with the Thompson–Eidhammer microphysics scheme (Thompson and Eidhammer 2014) used in the idealized simulations is again used to simulate the heavy rainfall case but with additional physics parameterizations and different domain configuration. For the physical parameterizations, the Yonsei University (YSU) planetary boundary layer scheme (Hong et al. 2006), the Betts-Miller-Janjic (BMJ) cumulus parameterization scheme (Janjic 1994), the unified Noah land surface model (Tewari et al. 2004), the Rapid Radiative Transfer Model (RRTM) longwave radiation scheme (Mlawer et al. 1997), and the Dudhia shortwave radiation scheme (Dudhia 1989) are used. Figure 4.10 shows two-way nested domains and terrain height. The horizontal grid spacings for domains 1, 2, and 3 are 27, 9, and 3 km, respectively. The cumulus parameterization scheme is applied to domains 1 and 2. The numbers of horizontal grids for domains 1, 2, and 3 are  $225 \times 210$ ,  $225 \times 210$ , and  $354 \times 390$ , respectively. The model top height is 50 hPa (~20 km). There are 42 stretched vertical layers, with a grid spacing of ~70 m in the lowest model layer. The 1-hourly  $0.25^\circ \times 0.25^\circ$  resolution ERA5 reanalysis data (Copernicus Climate Change Service 2017) are used for initial and boundary conditions. The model is integrated for 7 days and 12 hours

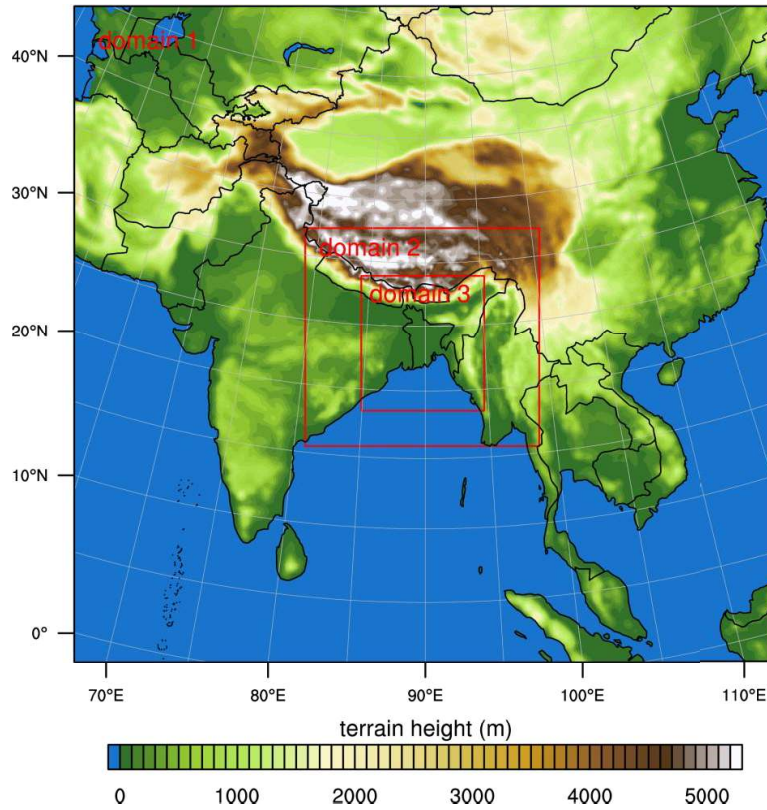


Figure 4.10 Three nested model domains for the real-case simulations and terrain height.

starting from 1200 LST 16 June 2014, and the simulation results from 0000 LST 17 to 0000 LST 24 in the innermost domain are used for analysis.

The simulated and observed 7-day accumulated precipitation amounts are shown in Fig. 4.11. The spatial distribution of the accumulated precipitation amount is well simulated in NP, despite some underestimation. NP well predicts the large amount of precipitation over the southeastern region of Bangladesh. For the western region of Bangladesh, neither of the simulations manages to produce the observed amount of precipitation, but the prediction of NP is much closer to the observation than that of OP where the precipitation amount is more underestimated. Interestingly, OP largely overestimates (44%) the precipitation amount at Sylhet (24.90°N, 91.88°E) in the northeastern region of the country, while it is relatively well predicted by NP (overestimation by 10%).

Using the simulated and observed accumulated precipitation amounts at the location of each meteorological station, Brier scores are calculated (Fig. 4.12). For almost all precipitation thresholds, NP gives lower Brier scores than OP, which indicates better prediction of precipitation. The difference in Brier scores is pronounced for thresholds smaller than 200 mm and thresholds of 470–630 mm, owing to the better performance of NP in the western and the southeastern regions, respectively.

Figure 4.13 presents the time- and domain-averaged vertical profiles of hydrometeor mixing ratios and mass-weighted mean radii of raindrops and cloud droplets. Differences in the hydrometeor mixing ratio between the two accretion parameterizations are relatively small compared to those shown in the idealized simulations, possibly due to the long simulation period and the complicated dynamical environment of the real-case

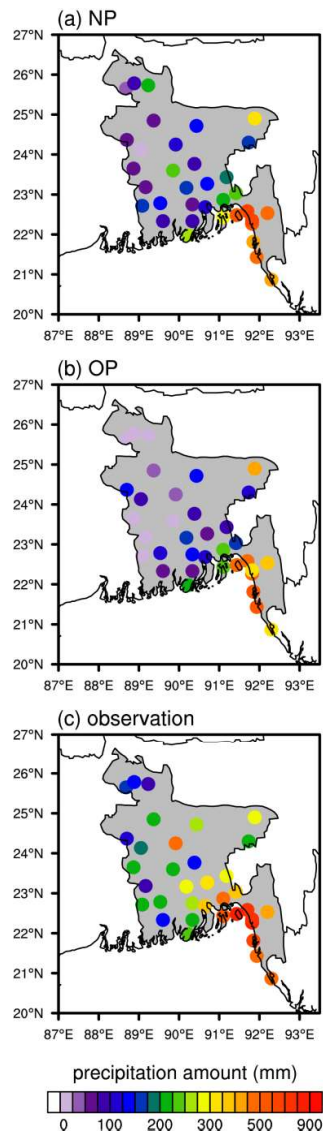


Figure 4.11 Spatial distributions of 7-day accumulated precipitation amount simulated with (a) NP and (b) OP and (c) observed at meteorological stations. The simulation results are interpolated to the locations of the meteorological stations in (a) and (b).

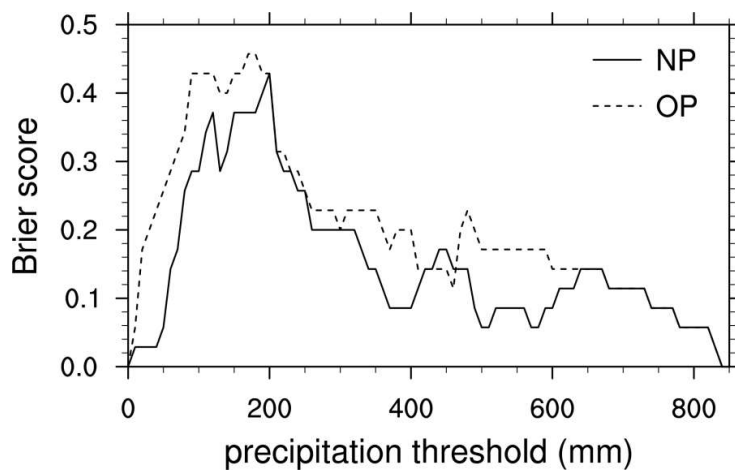


Figure 4.12 Brier scores calculated using the simulated and observed 7-day accumulated precipitation amounts at the location of each meteorological station.

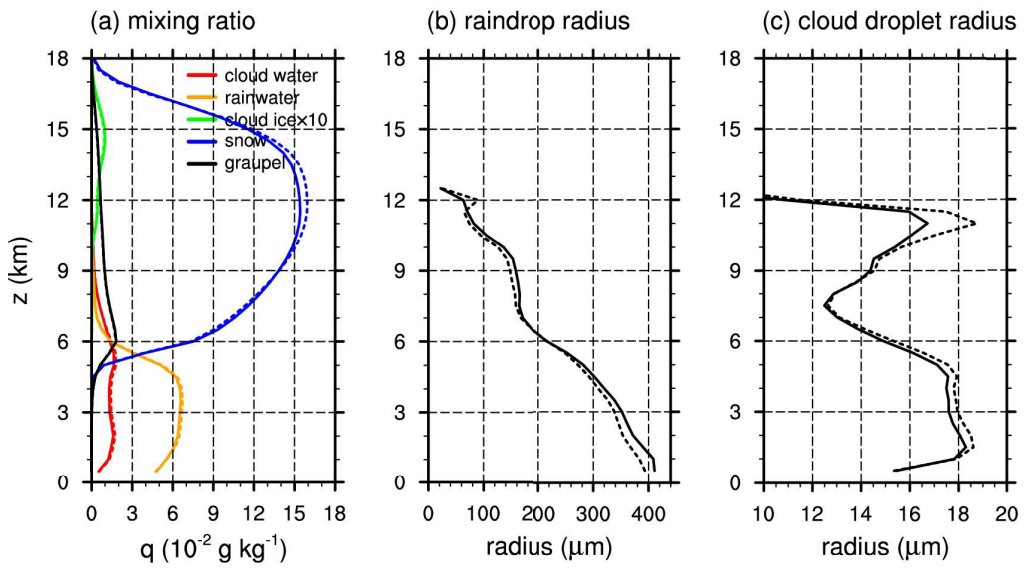


Figure 4.13 As in Fig. 4.5, but for the real-case simulations.

simulations. Among the hydrometeors, snow accounts for a large portion of clouds, indicating active ice microphysical processes. NP predicts a slightly larger snow mixing ratio at relatively low levels ( $z \sim 5\text{--}9$  km) and a smaller snow mixing ratio at relatively high levels ( $z \sim 9\text{--}16$  km), compared to OP. Mixing ratios of cloud water and rainwater are slightly smaller in NP than in OP, which can be attributed to the more active accretion process and the faster raindrop sedimentation in NP, respectively. Differences in the mean radii of raindrops and cloud droplets between NP and OP are evident. For  $z \leq 5$  km, NP predicts 4% larger mean raindrop radius and 2% smaller mean cloud droplet radius. The larger (smaller) mean raindrop (cloud droplet) radius in NP is consistent with the result of the idealized simulations.

The effects of NP on the accretion and autoconversion rates are also very similar to those shown in the idealized simulations. Figure 4.14 shows the time series of domain-averaged accretion and autoconversion rates, where the domain average is taken both horizontally (the innermost domain) and vertically ( $z = 0\text{--}18$  km). The time series in Fig. 4.14, also in Fig. 4.15, are plotted from 0000 LST 17 to 0000 LST 24 June 2014. In general, NP predicts a larger accretion rate and a smaller autoconversion rate than OP. The sum of the accretion and autoconversion rates shows little difference between NP and OP until 19 June when the precipitation rate was small, while the difference becomes large after that. The acc/auto ratio in NP is much higher than that in OP for the whole period, which is responsible for the larger mean raindrop radius in NP. The effects of NP on the liquid and ice water paths seem to be more complicated than those on the microphysical conversion rates (Fig. 4.15). Notable differences in the water paths are found from 20 June. For 21–22 June, the two rainiest days in the simulation period, the



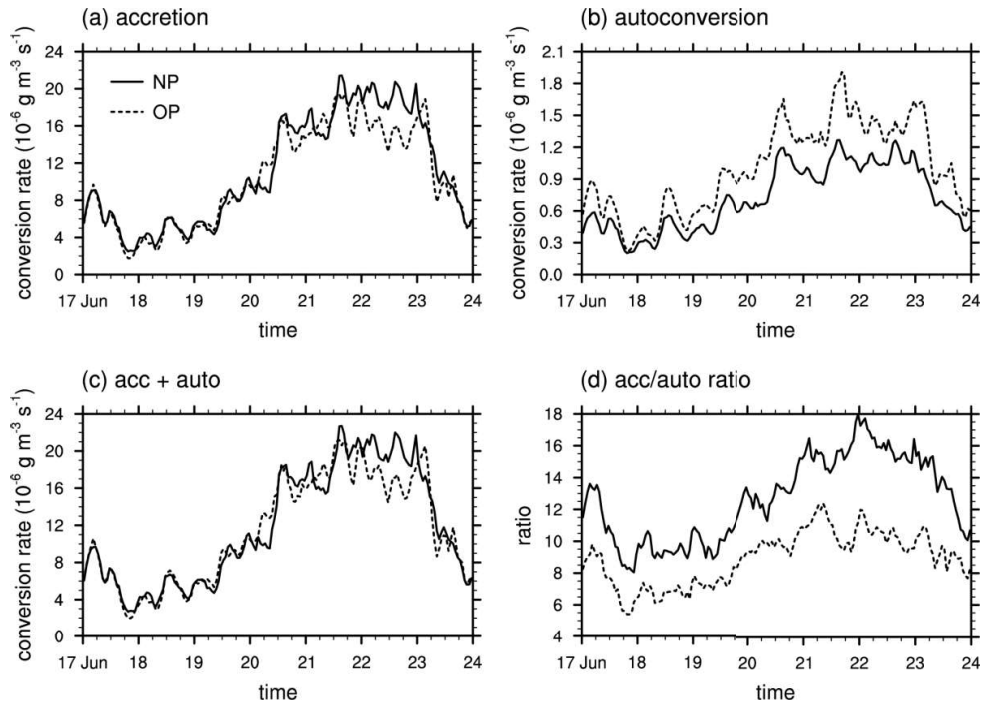


Figure 4.14 As in Fig. 4.6, but for the real-case simulations.

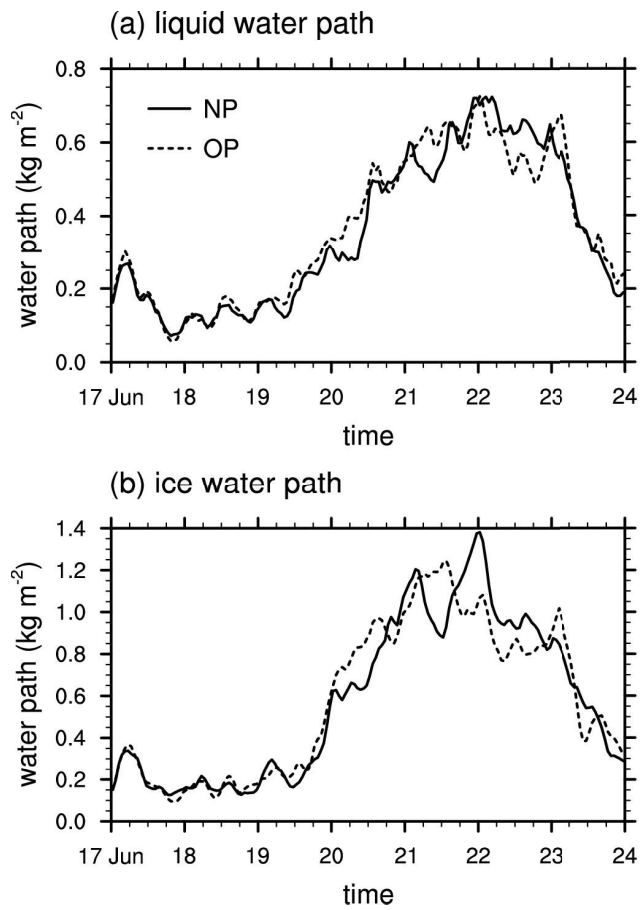


Figure 4.15 As in Fig. 4.7, but for the real-case simulations.

Liquid and ice water paths in NP are 4% and 8% larger than those in OP, respectively. The increases in the liquid and ice water paths lead to the increase in precipitation amount during this period, which results in the better precipitation prediction in NP.

The time- and domain-averaged vertical profiles of latent heating rates are shown in Fig. 4.16. Although the differences in the latent heating rates between NP and OP for the real-case simulations are relatively small compared to those for the idealized simulations, important features of the differences such as stronger net latent heating via condensation and evaporation at low levels in NP that are shown in the idealized simulations are also found in the real-case simulations. The stronger latent heating in NP may to some extent have contributed to the larger precipitation amount. It is noted that the differences in the latent heating rates between NP and OP averaged over a 1-day period from 1800 LST 21 June when the difference in the accretion rate is largest are about seven times those averaged over the whole 7-day period.

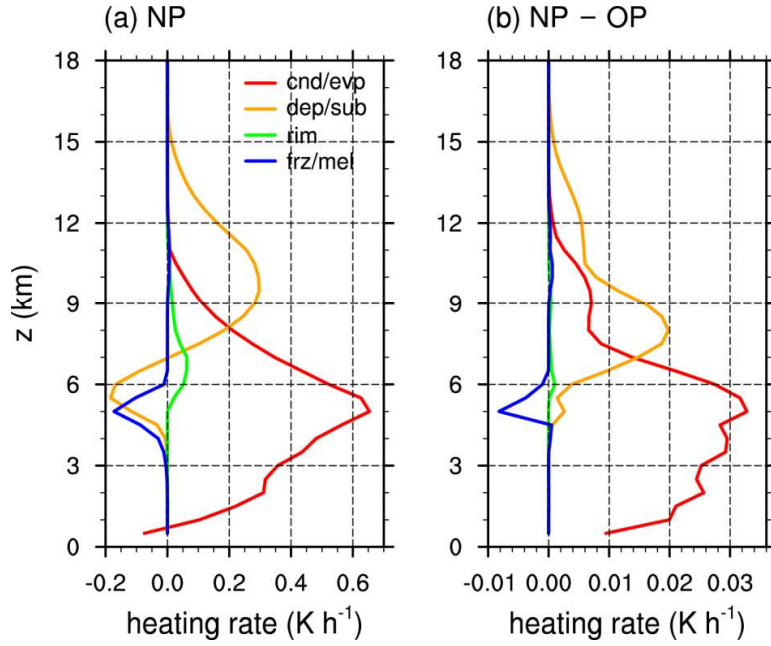


Figure 4.16 Time- and domain-averaged vertical profiles of (a) the heating rates due to condensation/evaporation, deposition/sublimation, riming, and freezing/melting in the real-case simulation with the new parameterization and (b) the differences in the heating rates between the new and original parameterizations.

# **5 Dynamical, thermodynamical, and cloud microphysical processes associated with extremely heavy precipitation in the Meghalaya Plateau region**

## **5.1 Case description and simulation setup**

### **5.1.1 Case description**

A monsoonal heavy precipitation event occurred over and around MP on 18–19 August 2015. The maximum observed 1-day precipitation amount on 19 August 2015 was 745 mm at Mawsynram station, and most of the precipitation was concentrated in the late night to early morning. To examine the synoptic condition during this event, the ERA5 reanalysis data (Hersbach et al. 2020) are used. Figure 5.1 shows the synoptic fields at 900 hPa and 500 hPa at 0900 and 2100 UTC 18. At 0900 UTC 18, the initial stage of the heavy precipitation event, a monsoonal trough exists in the northeastern part of India and an anticyclonic circulation is centered at the southeastern part of the Bay of Bengal at the 900-hPa level (Fig. 5.1a). The resultant southwesterly flow transports the warm and moist air along the east coast of India toward the inland area of Bangladesh and MP. After 12 hours, when the precipitation became extreme, the monsoonal trough moves eastward, and the anticyclonic circulation over the Bay of Bengal moves eastward, resulting in the enhancement of the southwesterly flow between them (Fig. 5.1b). The inland area of Bangladesh exhibits higher equivalent potential temperature than 12 hours prior, which indicates the abundant supply of warm and moist air to MP at low levels. At

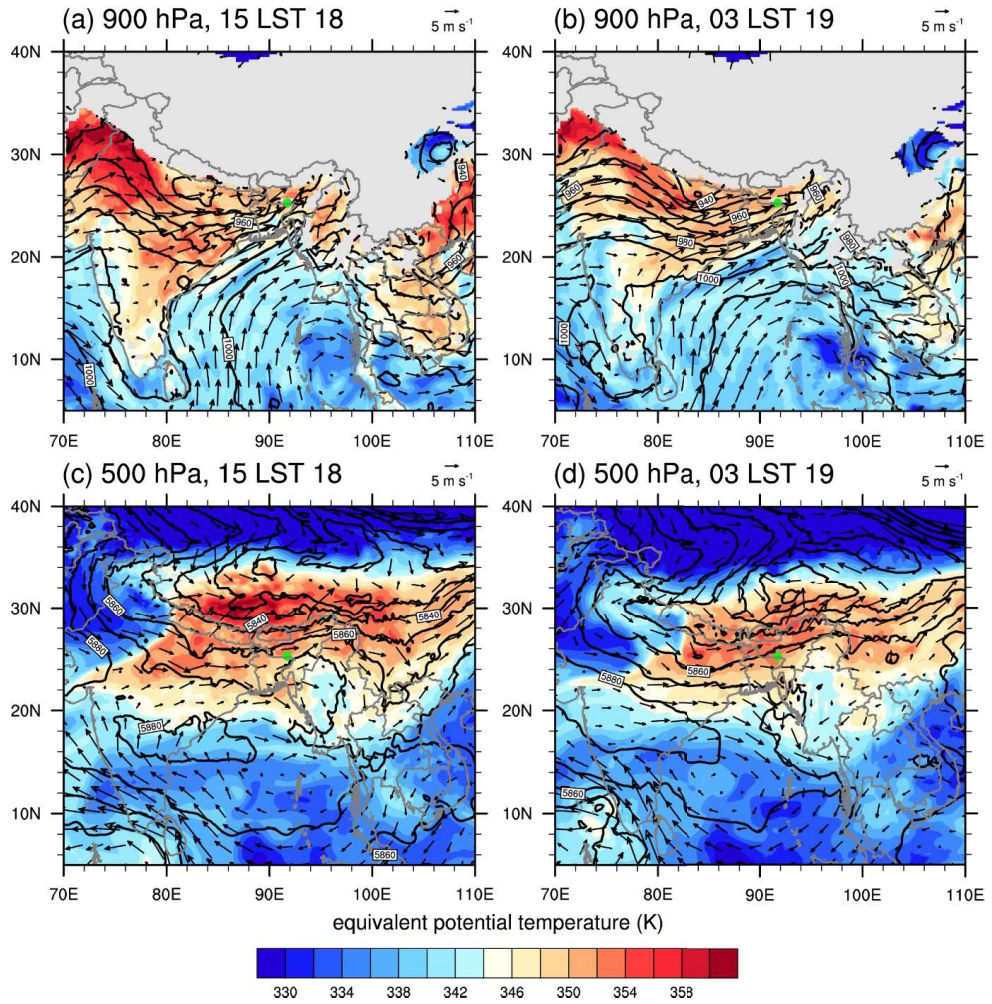


Figure 5.1 900-hPa equivalent potential temperature (shaded), horizontal wind vector (arrows), and geopotential height (m, black solid lines) fields at (a) 1500 LST 18 and (b) 0300 LST 19 from the ERA5 reanalysis data. Subfigures (c) and (d) are analogous to (a) and (b) but at 500 hPa. The green dot denotes Cherrapunji.

upper levels, however, the westerly flow over and around MP is relatively weak compared to the southwesterly flow at 900 hPa (Figs. 5.1c and d).

### 5.1.2 Model description and simulation design

To simulate this heavy precipitation event, the Weather Research and Forecasting (WRF) model version 4.2 (Skamarock et al. 2019) is used. For the initial and boundary conditions, the ERA5 reanalysis data (Hersbach et al. 2020) with  $0.25^\circ$  horizontal resolution and 1-hr temporal resolution are used. The WRF model is integrated over 36 hr from 2100 UTC 17 (0300 LST 18) August 2015, and the simulation data from 0900 UTC 18 (1500 LST 18) to 0900 UTC 19 (1500 LST 19) August 2015 are used for analysis, to take into account the model spin-up time. Note that the local standard time of Bangladesh is used hereafter because of the strong diurnal variation of precipitation in this region (e.g. Ohsawa et al. 2001; Terao et al. 2006).

In this study, three different simulations are performed. The model domain configuration is presented in Fig. 5.2. The control (CNTL) simulation and the simulation without MP (noMP) use four nested domains from domains 1 to 4. The horizontal grid spacings of domains 1, 2, 3, and 4 are 27 km ( $181 \times 166$  grid points), 9 km ( $271 \times 271$ ), 3 km ( $331 \times 376$ ), and 1 km ( $481 \times 421$ ), respectively. 42 vertical layers, which are stretched with height, are used for all domains. The time steps for domains 1, 2, 3, and 4 are 20, 6.66, 2.22, and 0.74 s, respectively. The terrain height of domain 4 presented in Fig. 5.3 clearly shows the difference between the CNTL and noMP simulations. The terrain height of MP in the noMP simulation is reduced to 13 m which is the average height of the upwind region. This flattening process is applied to all domains,

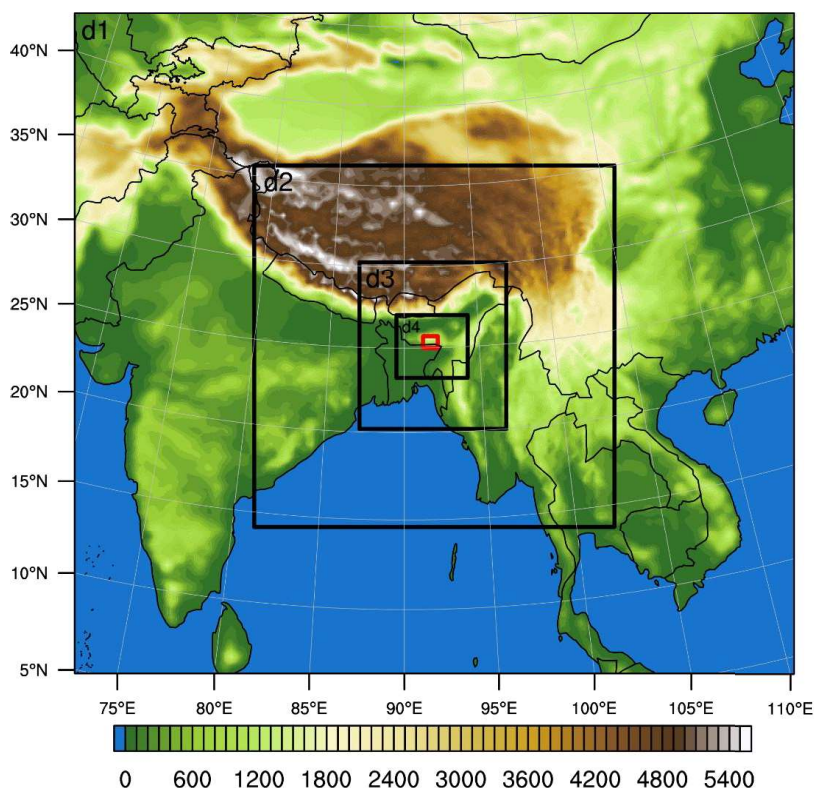


Figure 5.2 Four nested domains in the CNTL and noMP simulations and one additional domain in the HRES simulation with terrain height (m, shaded). d1, d2, d3, and d4 indicate domains 1, 2, 3, and 4, respectively. Domain 5 of the HRES simulation is indicated by red box.



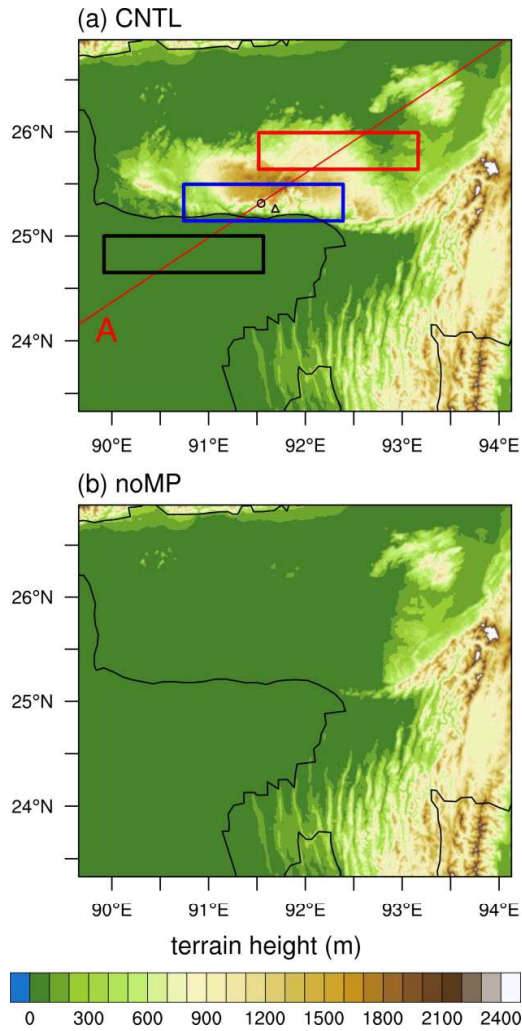


Figure 5.3 Terrain height in the innermost domain (domain 4) of the (a) CNTL and (b) noMP simulations. Black, blue, and red boxes represent the upwind, upslope, and downwind regions, respectively. Black hollow circle and triangle indicate Mawsynram (25.30°N, 91.58°E) and Cherrapunji (25.25°N, 91.73°E), respectively. Red line (Line A) represents the reference line used for analysis.

but with a relaxation process near the lateral boundaries in order to avoid abrupt changes in terrain height. The relaxation zone lies within  $\sim 20$  km from the lateral boundaries, with a greater decrease in terrain height according to the distance from boundaries. Figure 5.3a also shows a reference line (red line, Line A hereafter) that passes through Mawsynram (black circle) and the upwind, upslope, and downwind regions (black, blue, and red boxes, respectively) that are determined based on the low-level wind direction and the movement of precipitation systems in this event.

A simulation with a higher horizontal resolution (HRES) than the CNTL simulation is performed to examine the effects of local topography on the heavy precipitation, focusing on the southern slope of MP. In the HRES simulation, one more nested domain with a horizontal grid spacing of  $1/3$  km is added as domain 5 (red box in Fig. 5.2). Domain 5 consists of  $301 \times 241$  grid points, and the time step is 0.25 s.

The physical parameterizations chosen for the simulations in this study are as follows: the Yonsei University (YSU) planetary boundary layer scheme (Hong et al. 2006), the Dudhia shortwave radiation scheme (Dudhia 1989), the Rapid Radiative Transfer Model (RRTM) longwave radiation scheme (Mlawer et al. 1997), the unified Noah land surface model (Tewari et al. 2004), and the Kain-Fritsch cumulus parameterization scheme (Kain 2004). The cumulus parameterization scheme is not applied to domains 3, 4, and 5. The Thompson–Eidhammer cloud microphysics scheme (Thompson and Eidhammer 2014) is used with the cloud droplet autoconversion and raindrop–cloud droplet accretion parameterizations replaced by those developed in Lee and Baik (2017) and Chapter 4, respectively.

## 5.2 Results

### 5.2.1 Validation and precipitation characteristics

The numerical simulation of this event successfully reproduces the observed spatial distribution of accumulated precipitation. Figure 5.4 shows the comparison of 24-hr (0900 LST 18–0900 LST 19) accumulated precipitation amount in the CNTL simulation and the rain gauge observation. The rain gauge data in Bangladesh and India were provided by the Bangladesh Meteorological Department and the India Meteorological Department, respectively. The observed spatial pattern of precipitation that shows the largest amount of accumulated precipitation in the southern slope of MP and relatively small amount of accumulated precipitation in the other part of MP is reproduced in the CNTL simulation (Fig. 5.4a). The simulated precipitation in the southwest of MP, however, cannot be properly evaluated because of the lack of rain gauge stations in this region of Bangladesh. The amounts of accumulated precipitation at Cherrapunji and Mawsynram, the two stations that experienced the most extreme precipitation, are underestimated by 108 and 475 mm, respectively. The deviation of simulated precipitation amount from the observation at these stations are largely reduced in the HRES simulation that better resolves the local topography, which will be shown in section 5.2.4. The correlation coefficient between the observed and simulated 24-hr accumulated precipitation amount is 0.78, which is high enough to assume that the simulations of this event in this study are valid.

To examine the temporal evolution of precipitation, the time series of precipitation rate over the upwind, upslope, and downwind regions in the CNTL and noMP simulations are presented in Fig. 5.5. In the upwind region (Fig. 5.5a), the

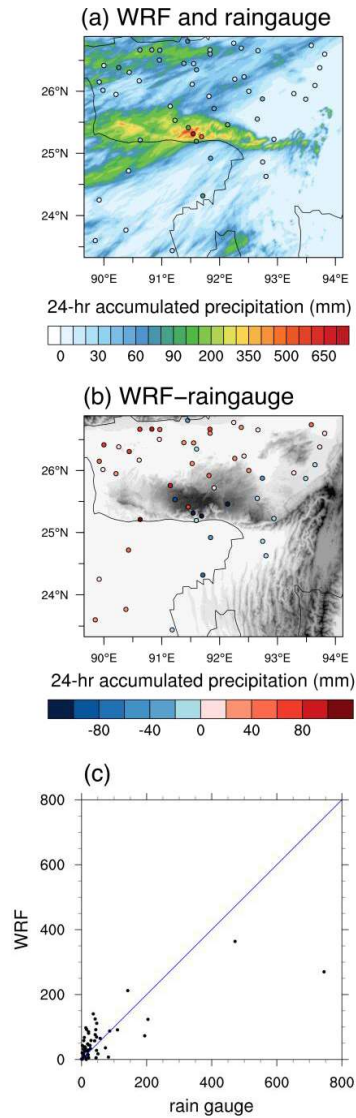


Figure 5.4 24-hr accumulated precipitation amount from the rain gauge observation (circles) and the CNTL simulation (shaded), and (b) their difference. (c) Scatter plot of the rain gauge observation and CNTL simulation for the 24-hr accumulated precipitation amount.

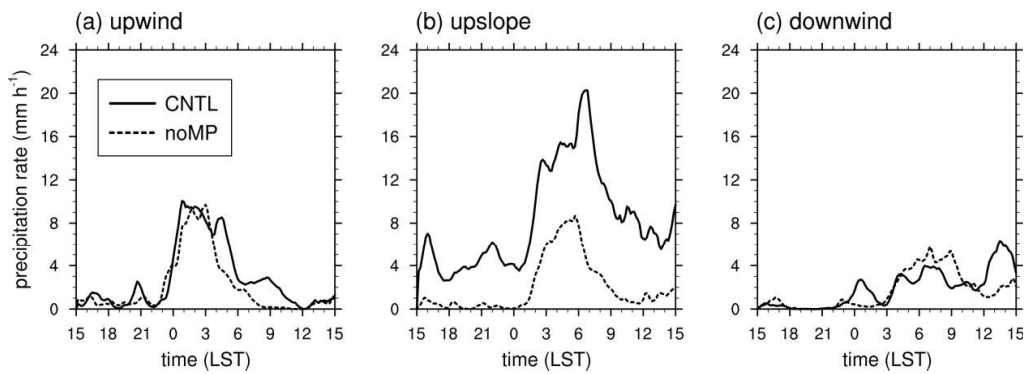


Figure 5.5 Time series of area-averaged precipitation rate for the (a) upwind, (b) upslope, and (c) downwind regions in the CNTL (solid) and noMP (dashed) simulations.

precipitation rate in the CNTL simulation is very small until 2210 LST 18 ( $\sim 0.8 \text{ mm h}^{-1}$  on average), and then it increases abruptly and reaches its peak at 0050 LST 19 ( $8.3 \text{ mm h}^{-1}$ ). In this region, the noMP simulation also shows a similar time series of precipitation rate. In the upslope region, the CNTL simulation shows moderate precipitation rates ( $4.2 \text{ mm h}^{-1}$  on average) until 0030 LST 19 when the precipitation rate starts to increase rapidly. This means that the precipitation systems are newly developed over the upslope region because the upwind region receives only little precipitation in the afternoon and evening. The start of the rapid increase in precipitation rate is delayed by 2 hr and 20 min in the upslope region, and this increase corresponds to the arrival of the precipitation systems that were pre-developed upwind of MP. The peak value in the upslope region in the CNTL simulation ( $20.3 \text{ mm h}^{-1}$ ) is more than twice that in the noMP simulation ( $8.7 \text{ mm h}^{-1}$ ), indicating that the advected precipitation systems are further intensified over the southern slope of MP. The precipitation rate in the upslope region in the CNTL simulation shows a second abrupt increase at 0530 LST 19, which does not appear in the noMP simulation. This implies that a new process that intensifies the precipitation is involved, which will be explained in section 5.2.3. In the downwind region (Fig. 5.5c), the overall precipitation rate is relatively small in both simulations.

The analysis period is divided into two phases, before/after the abrupt increase in precipitation rate. The 9-hr accumulated precipitation amount and 900-hPa wind fields of Phase 1 (1500 LST 18–0000 LST 19, P1 hereafter) and Phase 2 (0000–0900 LST 19, P2 hereafter) are shown in Fig. 5.6. P1 shows concentrated precipitation in the southern slope of MP where the prevailing southwesterlies go through orographic lifting. The upwind region receives only little precipitation in this period. P2 shows a much larger

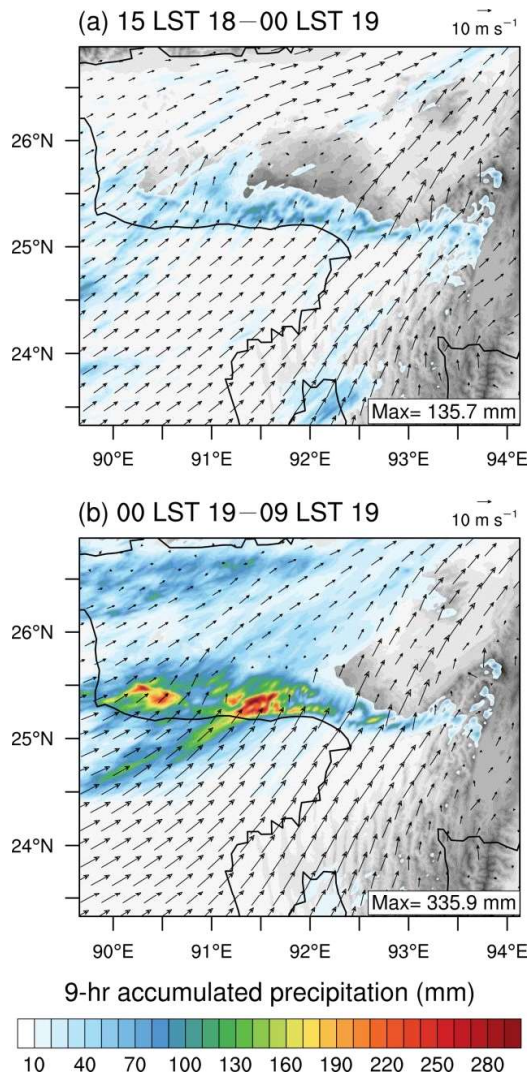


Figure 5.6 9-hr accumulated precipitation amount (shaded in color) and 900-hPa level wind vector (arrows) fields with terrain height (shaded in black) during (a) 1500 LST 18–0000 LST 19 and (b) 0000–0900 LST 19 August 2015.

amount of precipitation in the southern slope of MP and stronger southwesterlies compared to P1. In P2, some parts of the upwind region receive considerable amount of precipitation and they are elongated in the low-level wind direction, indicating the path of the pre-developed precipitation systems toward MP.

From the above results, P1 can be characterized by the period when the precipitation is initiated by MP, while P2 can be characterized by the period when the precipitation is intensified over the slope of MP. 75% of the total accumulated precipitation amount in the upslope region occurs in P2, implying that the intensification process may contribute more to the accumulated precipitation amount than the initiation process.

### **5.2.2 Dynamical and thermodynamical characteristics**

In this subsection, the dynamical and thermodynamical processes associated with this extreme precipitation case are examined. The development of nocturnal LLJ heading toward MP has been attributed to the heavy precipitation in this region in many previous studies (e.g. Terao et al. 2006; Sato 2013). Figure 5.7 shows the evolution of the vertical profiles of horizontal wind speed along the direction of Line A and equivalent potential temperature, averaged over the upwind region. All wind profiles have peaks below  $z = 1$  km (Fig. 5.7a). This vertical maximum of low-level wind speed is  $9.5 \text{ m s}^{-1}$  at 1800 LST 18 and increases up to  $17.3 \text{ m s}^{-1}$  at 0600 LST 19, and then decreases. The acceleration of low-level winds in the late night indicates the development of nocturnal LLJ, which is typically found in this region during the monsoon season (Terao et al. 2006; Sato 2013; Fujinami et al. 2017).



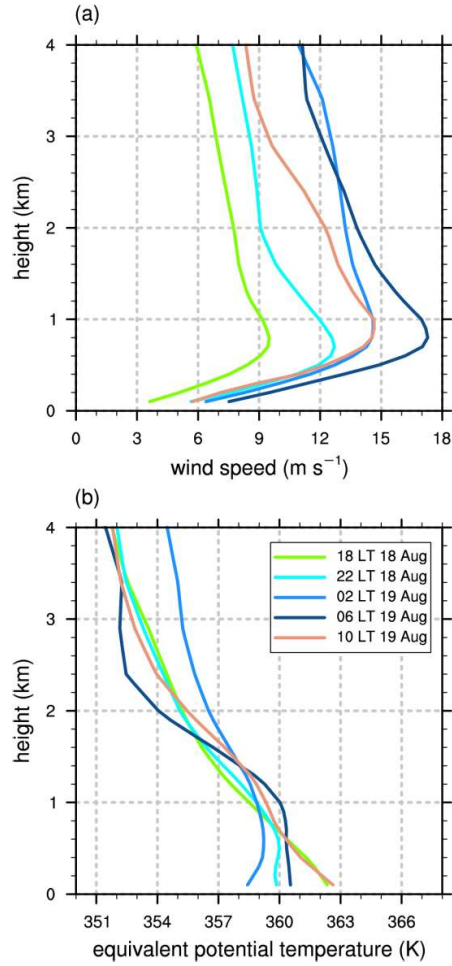


Figure 5.7 Vertical profiles of the area-averaged (a) wind speed component along the direction of Line A in Fig. 5.3a and (b) equivalent potential temperature in the upwind region.

The development of the nocturnal LLJ is mainly associated with synoptic forcing and the diurnal variation of convective instability. During this event, synoptic low-level southwesterlies toward MP blow between the trough over the northeastern part of India and the high pressure system over the Bay of Bengal (Figs. 5.1a and b). In the daytime (1800 LST 18 and 1000 LST 19), the atmosphere below  $z = 1$  km in the upwind region is conditionally unstable due to the surface heating, while it is slightly stable or almost neutral in the nighttime and early morning (2200 LST 18, 0200 LST 19, and 0600 LST 19) (Fig. 5.7b). As argued by Blackadar (1957), the relatively strong vertical mixing in the deep planetary boundary layer during the daytime reduces the vertical maximum of horizontal wind speed at the low level. During the nighttime, however, the vertical mixing is weakened and thus LLJ becomes stronger than in the daytime.

Because the precipitation in MP is largely affected by the water vapor transported by LLJ, it is important to examine how much water vapor has been transported. Figure 5.8b shows the time series of water vapor flux along the direction of Line A at 900 hPa averaged over the upwind region. The time series of water vapor flux is similar to that of horizontal wind speed (Fig. 5.8a). This indicates that the variability of water vapor flux is mainly modulated by the horizontal wind speed, not by the mixing ratio of water vapor. The water vapor flux increases almost monotonically from 1640 LST 18 to 0530 LST 19. This increasing trend of water vapor flux is similar to the trend of precipitation rate in the upslope region (Fig. 5.5b) with a 1–2-hr delay. This suggests that the water vapor flux over the upwind region is a main factor that affects the precipitation rate in the upslope region.

Figure 5.9 shows the vertical cross sections of wind vector and water vapor flux at

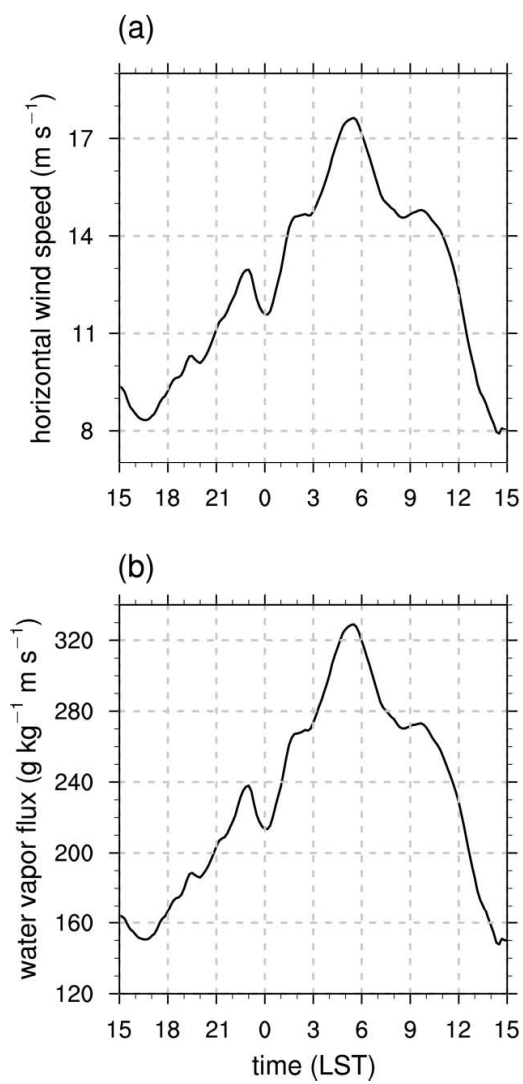


Figure 5.8 Time series of (a) horizontal wind speed and (b) water vapor flux at 900 hPa along the direction of Line A averaged over the upwind region.

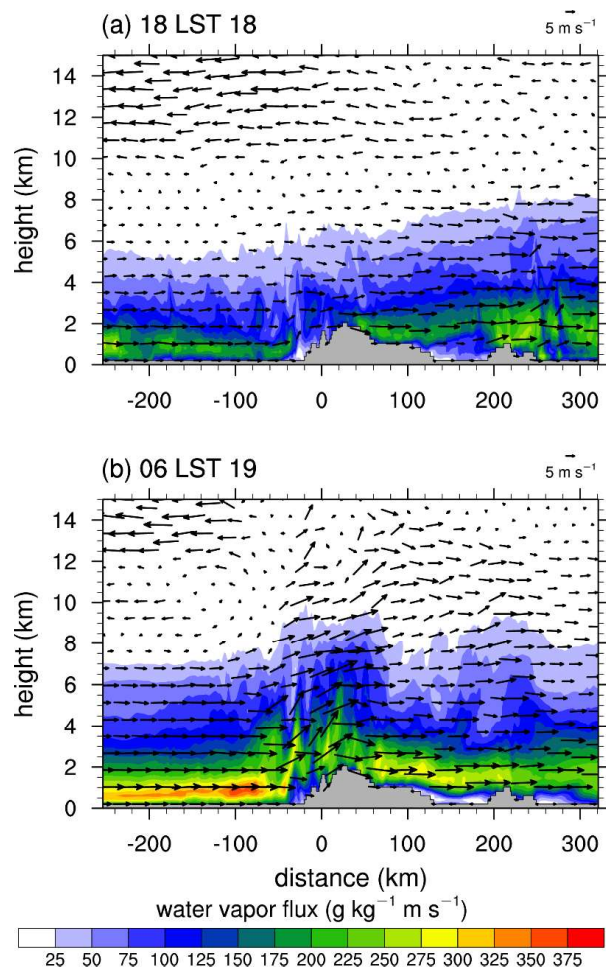


Figure 5.9 Vertical cross-sections of water vapor flux (shaded) and wind vectors along Line A at 1800 LST 18 and 0600 LST 19 August 2015.

1800 LST 18 and 0600 LST 19 along Line A (Fig. 5.3a). At 1800 LST 18, the layer with water vapor flux (greater than  $25 \text{ g kg}^{-1} \text{ m s}^{-1}$ ) appears up to  $z \sim 5 \text{ km}$  in the upwind region ( $x < -20 \text{ km}$ ). The water vapor flux is especially large at low levels ( $z < 2 \text{ km}$ ) in the upwind region, but it is small over the upslope of MP. At 0600 LST 19, the layer with water vapor flux (greater than  $25 \text{ g kg}^{-1} \text{ m s}^{-1}$ ) is thickened up to  $z \sim 7 \text{ km}$  in the upwind region, and the water vapor flux within  $z < 2 \text{ km}$  is increased about 1.5 times due to strong LLJ. When this LLJ reaches the upslope of MP, it is largely deflected upward and strengthened to some extent. As a result, a large amount of water vapor is transported upward. More water vapor can condense into cloud droplets releasing more latent heat, hence promoting deep convection. Another notable feature at this time is the upper-level wind direction. At 1800 LST 18, the winds at  $z > \sim 10 \text{ km}$  over MP blow to the southwest, consistent with those over the upwind region. At 0600 LST 19, however, winds blow to the northeast at all levels over MP, forming divergence at  $z > \sim 7 \text{ km}$  where the winds over the upwind region blow to the southwest or are relatively weak. It seems that the intensified LLJ rising over the steep upslope of MP contributes to the change in the upper-level wind direction over MP.

Figure 5.10 shows the vertical cross-sections of vertical velocity. At 2100 LST 18 when the low-level jet is weak, shallow and weak updrafts appear over the upslope region (Fig. 5.10a). At 0200 LST 19, deep and strong updrafts appear over the upwind region and approach MP (Fig. 5.10b). The strong vertical wind shear over the upwind region (Fig. 5.9) tilts the updrafts to the left (southwest). At 0600 LST 19, the updrafts approaching MP merge and become stronger over the upslope region (Fig. 5.10c). At this time, the updrafts develop relatively upright over the upslope region where the

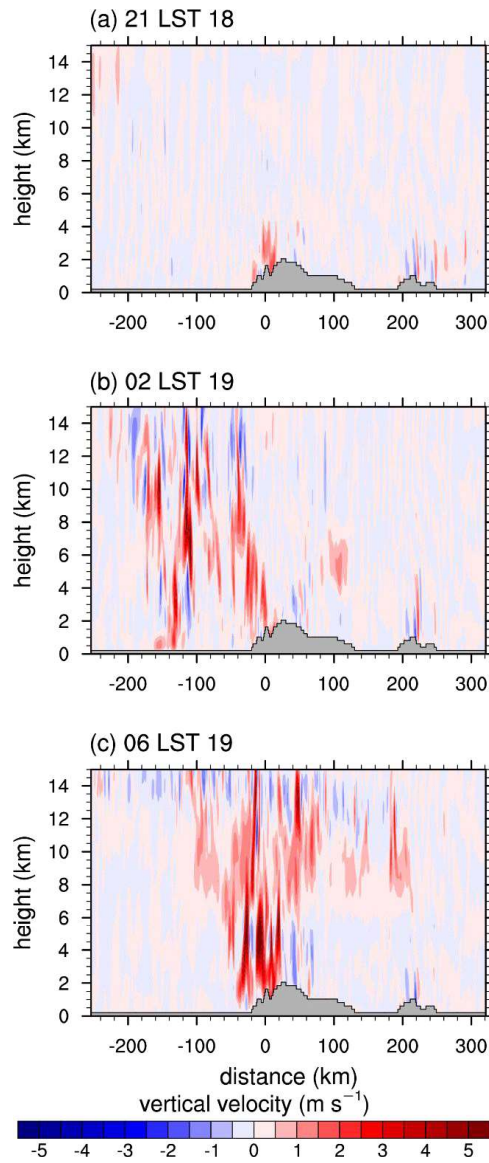


Figure 5.10 Vertical cross-sections of vertical velocity along Line A at (a) 2100 LST 18, (b) 0200 LST 19, and (c) 0600 LST 19 August 2015.

vertical wind shear is weak (Fig. 5.9b). The horizontal scale of the merged system is larger than that of individual updrafts. The merged system is expanded to the right (northeast) at upper levels, mainly due to the upper-level divergence and resultant horizontal spread of upper-level clouds.

### 5.2.3 Cloud microphysical characteristics

In this subsection, the cloud microphysical processes involved in this extreme precipitation case are examined. Figure 5.11 shows the time series of liquid water path (LWP) and ice water path (IWP) over the upwind, upslope, and downwind regions in the CNTL and noMP simulations. Before ~0000 LST 19, in the upwind region, there is almost no LWP and IWP in both simulations. In the upslope region, LWP in the CNTL simulation is  $\sim 1.5 \text{ kg m}^{-2}$  while that in the noMP simulation is still nearly zero. IWP is nearly zero in both simulations. These indicate that the moderate precipitation initiated over the upslope region in P1 is produced almost solely by warm microphysical processes. After ~0000 LST 19, in the upwind region, LWP and IWP increase abruptly in both simulations. Both warm and cold microphysical processes are involved in the precipitation systems in the upwind region. Unlike in P1, the cold microphysical processes contribute to the precipitation in P2. MP enhances both warm and cold microphysical processes. In the downwind region, due to the intense precipitation over the upslope region, LWP and IWP are relatively small.

For a detailed analysis of the cloud microphysical characteristics, vertical profiles of hydrometeors and conversion rates related to rainwater production averaged over the upslope region are shown in Figs. 5.12 and 5.13, respectively. At 2100 LST 18, the

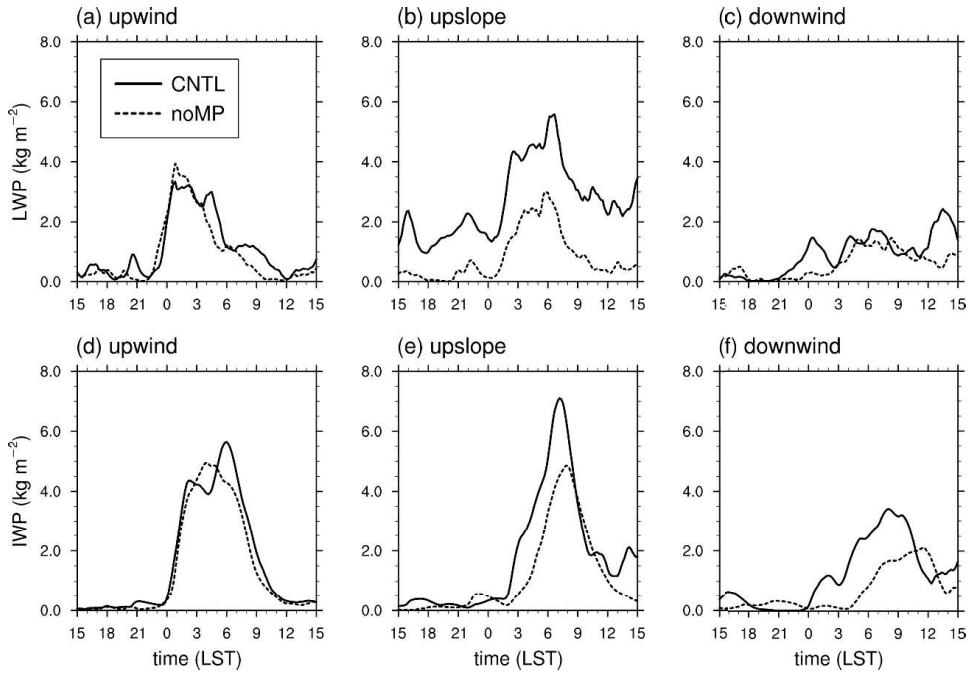


Figure 5.11 Time series of LWP (top row) and IWP (bottom row) averaged over the upwind (first column), upslope (second column) and downwind (third column) regions in the CNTL (solid) and noMP (dashed) simulations.



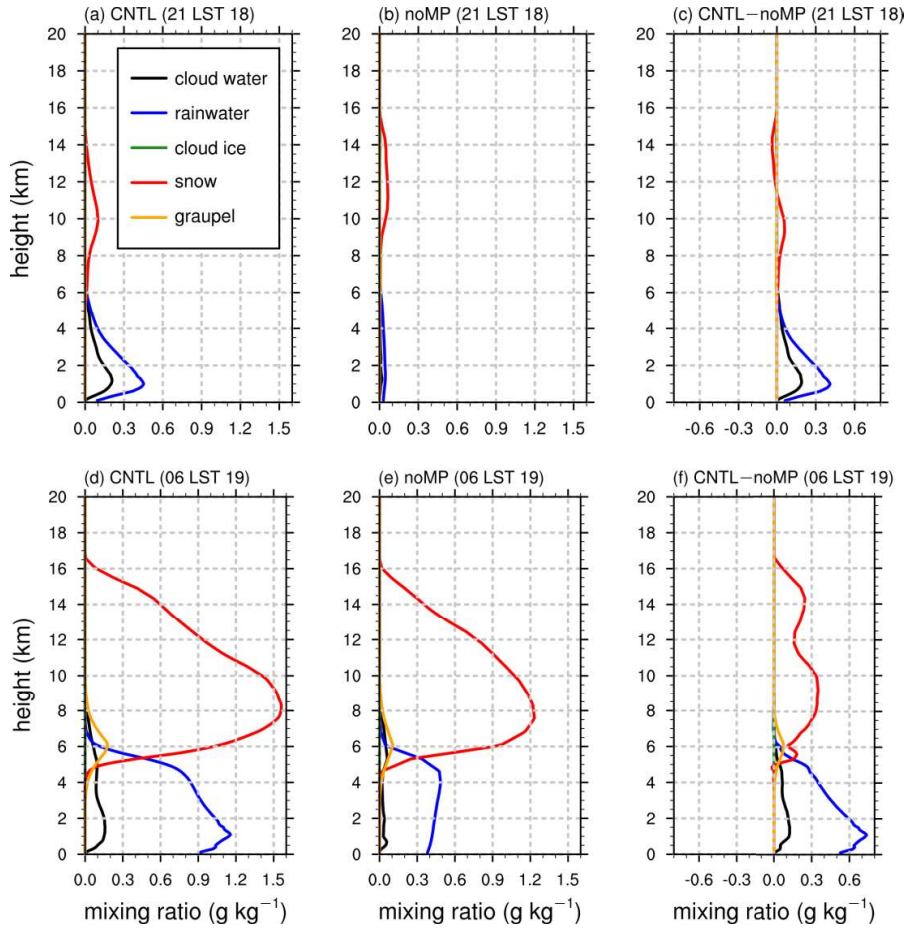


Figure 5.12 Vertical profiles of hydrometeors averaged over the upslope region at 2100 LST 18 (top row) and 0600 LST 19 (bottom row) August 2015 in the CNTL (first column) and noMP (second column) simulations and their differences (third column).

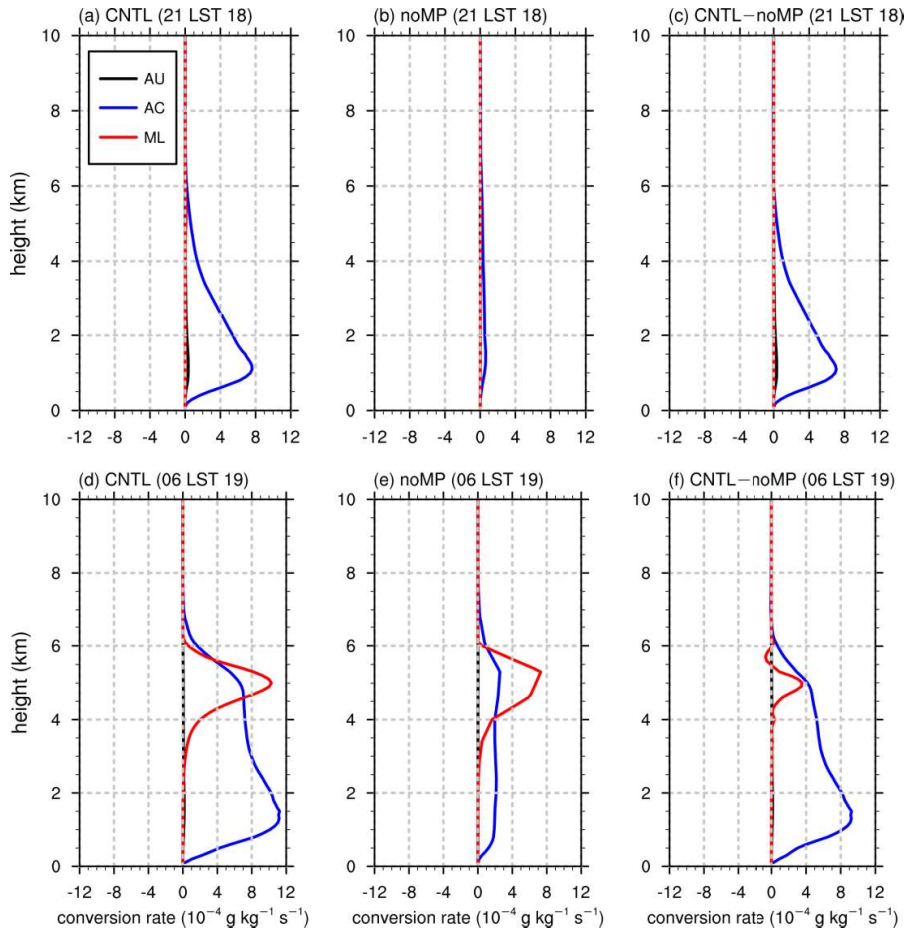


Figure 5.13 Vertical profiles of microphysical conversion rates related to rainwater production (AU: autoconversion, AC: accretion, ML: melting) averaged over the upslope region at 2100 LST 18 (top row) and 0600 LST 19 (bottom row) August 2015 in the CNTL (first column) and noMP (second column) simulations and their differences (third column).

cloud water, rainwater, and snow are the main hydrometeors in the CNTL simulation, accounting for 25%, 56%, and 19% of the total hydrometeor mixing ratio, respectively (Fig. 5.12a). The cloud water and rainwater exist at  $z < \sim 6$  km and their mixing ratios both peak at  $z \sim 1$  km. In contrast, the snow appears at  $z > \sim 6$  km and its mixing ratio peaks at  $z \sim 10$  km, leaving little chance of mixed-phase microphysical processes such as riming. In the noMP simulation, there are only little amounts of cloud water and rainwater, but snow exists at a similar amount as in the CNTL simulation (Fig. 5.12b). The differences in cloud water and rainwater mixing ratios between the CNTL and noMP simulations are greatest at  $z \sim 1$  km. These differences are mainly attributed to the accretion rate. The accretion rate is dominant and peaks at  $z \sim 1$  km in the CNTL simulation, while the conversion processes rarely occur in the noMP simulation (Figs. 5.13a and b). The active accretion process in the CNTL simulation is mainly attributed to the strong updrafts over the upslope region (Fig. 5.10a) that supply a large amount of cloud droplets to be collected by raindrops and acts as the key factor for the initiation of precipitation in P1.

At 0600 LST 19, in the CNTL simulation, snow and rainwater mixing ratios increase substantially and a small amount of graupel appears at  $z = \sim 4\text{--}8$  km (Fig. 5.12d). The noMP simulation also shows a large amount of hydrometeors (Fig. 5.12e) because many of the precipitation systems are not generated over the upslope but previously developed upwind of MP and advected toward the upslope (Fig. 5.5a). Compared to the noMP simulation, the CNTL simulation shows much larger snow and rainwater mixing ratios (Fig. 5.12f). This indicates that the heavier precipitation in the CNTL simulation is caused by the enhancement of both warm and cold microphysical processes. The

difference in vertical profiles of conversion rates shows that the accretion process and the melting process are more active in the CNTL simulation than in the noMP simulation (Fig. 5.13f). The increment of accretion rate is much larger than that of melting rate. The larger vertical velocities in the merged and intensified updrafts over the upslope region as well as the enhanced melting of ice hydrometeors that produces large-sized raindrops enhance the accretion process. The increment of melting rate in the upslope region is relatively small because a large amount of snow produced at upper levels are advected to upwind and downwind regions due to the upper-level divergence. Therefore, the heavier precipitation in the CNTL simulation than in noMP simulation in P2 is mainly attributed to the more active accretion process and partly attributed to the more active melting process.

Figure 5.14 shows the vertical cross-sections of liquid and ice hydrometeor mixing ratios. It is seen that the precipitation over the upslope region at 2100 LST 18 in P1 is produced almost solely by warm microphysical processes (Fig. 5.14a). At 0200 LST 19, a number of precipitation systems with both liquid and ice hydrometeors are generated over the upwind region and move to the northeast in both CNTL and noMP simulations (Figs. 5.14c and d). The precipitation systems slow down over the southern slope of MP and merge together as shown in the CNTL simulation at 0600 LST 19 (Fig. 5.14e). The merged system is led by the ice-phase clouds at upper levels. Due to the upper-level divergence, the ice hydrometeors at the upper level in the CNTL simulation are transported far to the downwind region, which is not accompanied by the liquid hydrometeors below. Because the noMP simulation does not show either the merging of

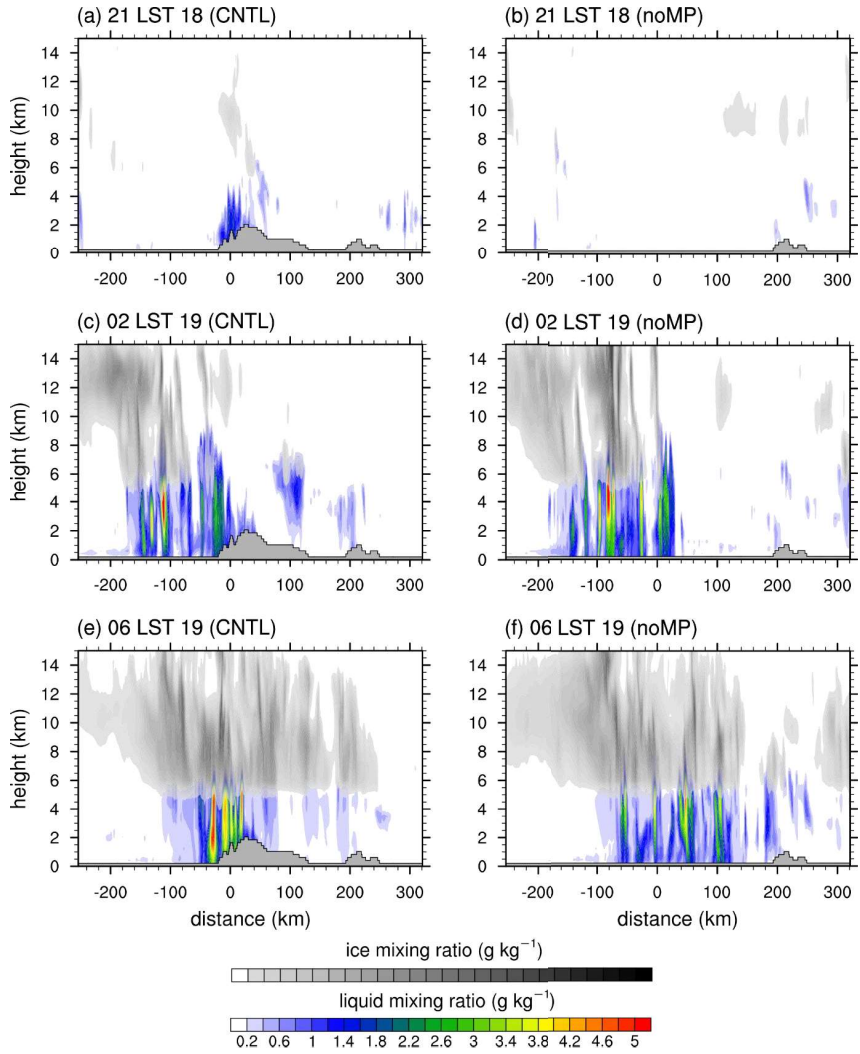


Figure 5.14 Vertical cross-sections of the liquid and ice hydrometeor mixing ratios at 2100 LST 18 (top row), 0200 LST 19 (middle row), and 0600 LST 19 (bottom row) August 2015 in the CNTL (left column) and noMP (right column) simulations.

precipitation systems or the leading of upper-level clouds, the existence of MP is attributed to these features in the CNTL simulation.

#### **5.2.4 Local topographic effect on precipitation**

Many valleys and ridges in the southern slope of MP create complex terrain with steep slopes (Fig. 5.15a). The steep slopes are closely related to the formation of orographic wind flows, which can be related to precipitation. In this subsection, by comparing the HRES simulation with the CNTL simulation, the effects of local topography on precipitation are investigated. The HRES simulation with the finer horizontal resolution better represent the local topography than the CNTL simulation. The difference in terrain height between the HRES and CNTL simulations (Fig. 5.15b) shows that the effects of the increase in horizontal resolution are pronounced in the valley regions. The terrain height in the HRES simulation is lower inside the valleys and higher at the valley slope, which means that the slope of the HRES simulation is steeper than that of the CNTL simulation.

The heavy precipitation is mainly simulated over the ridges branching out southward and the slopes near these ridges (Fig. 5.15c). The 24-hr accumulated precipitation amount in the HRES simulation is overall greater compared to that in the CNTL simulation except around the western region of Mawsynram (Fig. 5.15d). This reduces the deviation of the simulated precipitation amount from the rain gauge observation seen in the CNTL simulation. The 24-hr accumulated precipitation amounts in the rain gauge observation, CNTL simulation, and HRES simulation are 472, 364, and 521 mm, respectively, for Cherrapunji, and 745, 270, and 350 mm, respectively, for

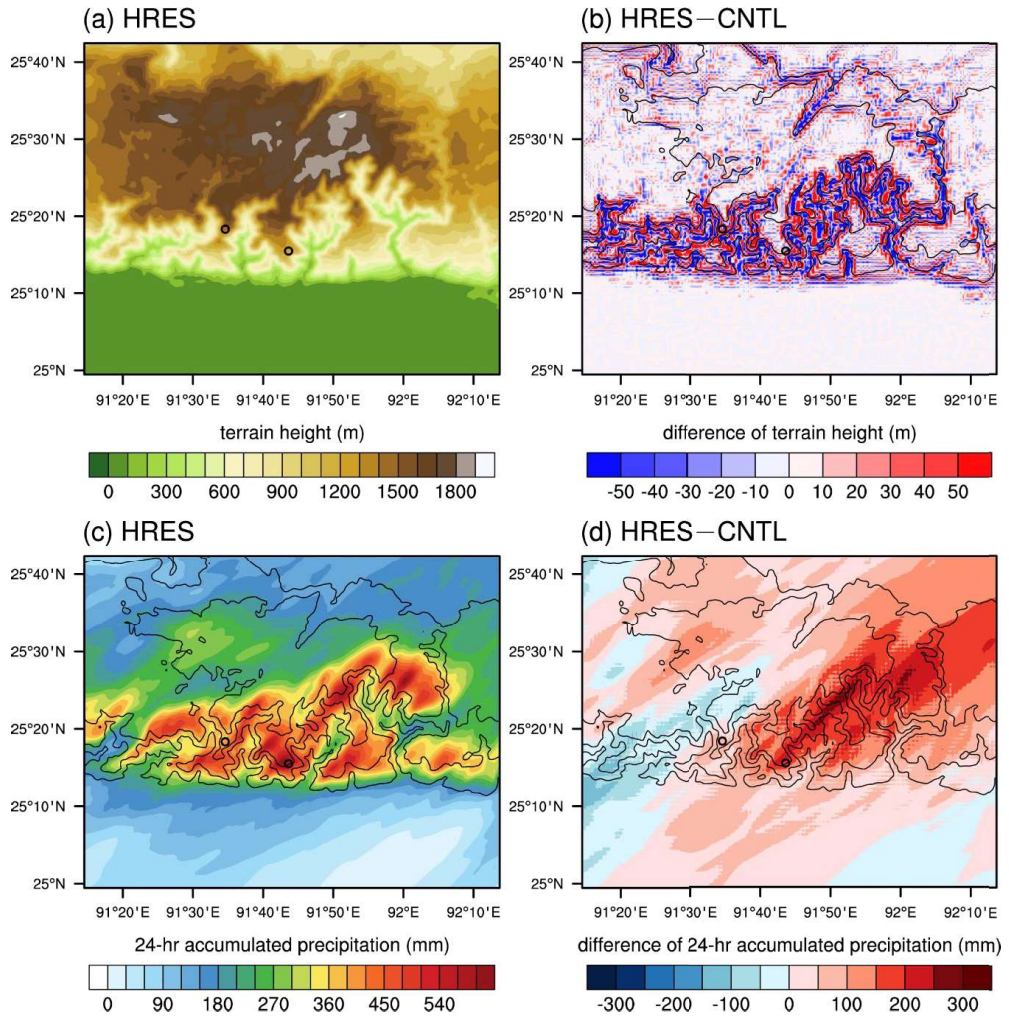


Figure 5.15 (a) Terrain height in the HRES simulation and (b) the difference between the HRES and CNTL simulations. (c) 24-hr accumulated precipitation amount in the HRES simulation and (d) the difference between the HRES and CNTL simulations. Terrain height is contoured at 400-m intervals in (b), (c), and (d).

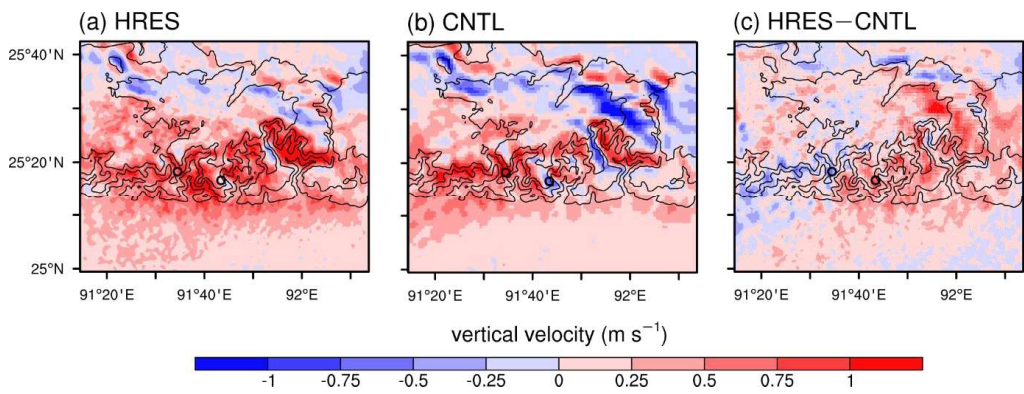


Figure 5.16 Horizontal distributions of vertical velocity at  $z = 3$  km averaged over P2 (0000–0900 LST 19) in the (a) HRES and (b) CNTL simulations and (c) their difference. Terrain height is contoured at  $400$  m intervals.



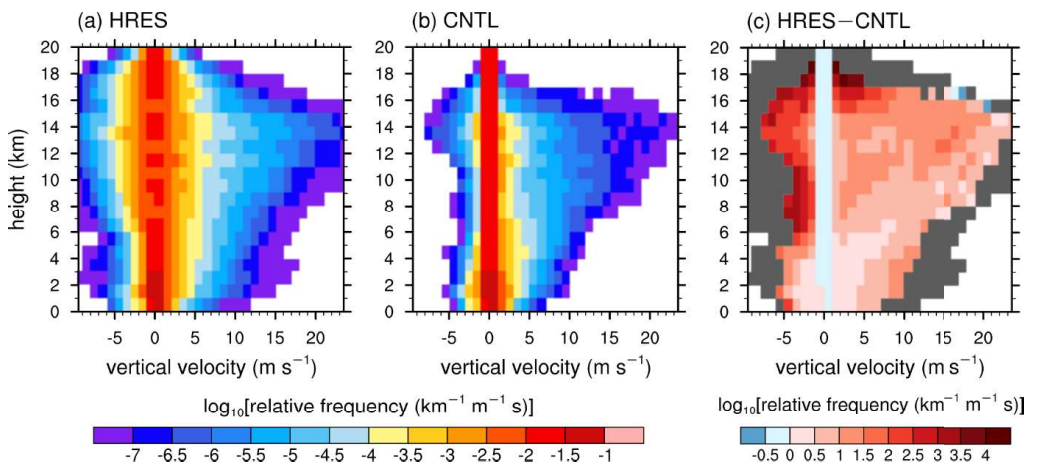


Figure 5.17 Contoured frequency by altitude diagrams (CFADs) of vertical velocity in the (a) HRES and (b) CNTL simulations and (c) their difference. Bins with HRES values only are indicated by grey color in (c)

Mawsynram. The largest increase is seen along the steep slope at the northeast of Cherrapunji where the difference in terrain height is large. This implies that the steepness of the terrain largely affects the precipitation intensity.

The steeper slope can intensify orographic updrafts and downdrafts. The intensified orographic flows may be the cause of the increased precipitation in the HRES simulation. Figure 5.16 shows the vertical velocity at  $z = 3$  km averaged over P2. Note that the vertical velocity at  $z = 3$  km in P1 does not show significant differences between the HRES and CNTL simulations (not shown). The overall spatial patterns look similar in both simulations. The updrafts appear on the upslope area of valleys, while the downdrafts appear on the downslope area of valleys in both simulations. However, there are differences in the magnitude of vertical velocities between the two simulations. The CFADs of vertical velocity show that strong updrafts are more frequent and the weak vertical velocities less than  $1 \text{ m s}^{-1}$  are less frequent in the HRES simulation (Fig. 5.17). This means that the variability of vertical velocity is high in the HRES simulation. In the spatial distribution (Fig. 5.16), only the updrafts are intensified, while the downdrafts are weakened. This results in an overall increase of vertical velocity around Cherrapunji. The regions with the overall increase in vertical velocity are well-matched with the regions with increased precipitation (Figs. 5.15d and 5.16c). This implies that the intensification of vertical velocity by steeper slopes in the HRES simulation is closely related to the increased precipitation.

### **5.3 Sensitivities to physical parameterization schemes and ensemble prediction**

Simulating and predicting extreme precipitation in the MP region is challenging because of the complex topography and its interactions with various physical processes. Therefore, sensitivities of simulated precipitation to various physical parameterization schemes deserve an investigation. The heavy precipitation event investigated in the previous subsection is again used for the sensitivity test.

For microphysics sensitivity experiments, the Milbrandt-Yau (MY) (Milbrandt and Yau, 2005), Morrison (Morrison et al. 2009), National Severe Storms Laboratory (NSSL) (Gilmore et al. 2004), predicted particle properties (P3) (Morrison and Milbrandt 2015), Thompson-Eidhammer (TE) (Thompson and Eidhammer 2014), and WRF double moment 6-class (WDM6) (Lim and Hong 2010) schemes are used. All those microphysics schemes predict mixing ratio and number concentration of cloud droplets and raindrops, but there are differences for ice particles. For example, both the TE and WDM6 schemes predict only mixing ratio of ice particles, but the MY and NSSL schemes predict both mixing ratio and number concentration of ice particles. The NSSL scheme considers graupel volume for the prediction of graupel density. The P3 scheme represents ice particles by several physical properties which evolve freely with time. For microphysics sensitivity experiments, each microphysics scheme together with the YSU PBL scheme (Hong et al. 2006) and the Dudhia shortwave (Dudhia 1989)/RRTM longwave (Mlawer et al. 1997) radiation schemes is used. Ensemble average (MP\_EN) for the six simulations with the different microphysics schemes is calculated. Sensitivities of simulated precipitation to four PBL schemes, namely, Asymmetric Convective Model

version 2 (ACM2) (Pleim 2007), Mellor-Yamada-Janjic (MYJ) (Janjic 1994), University of Washington (UW) (Bretherton and Park 2009), and YSU schemes are examined. For PBL sensitivity experiments, the TE microphysics scheme and the Dudhia shortwave/RRTM longwave radiation schemes are common. Ensemble average for the four simulations with the different PBL schemes (PBL\_EN) is calculated. Three radiation schemes, the CAM shortwave/longwave (Collins et al. 2004), Dudhia shortwave/RRTM longwave, and RRTMG shortwave/longwave (Iacono et al. 2008) radiation schemes, are used. Both the TE microphysics and YSU PBL schemes are common in radiation sensitivity experiments. Ensemble average for the radiation schemes is indicated by RAD\_EN. Ensemble average for the total 11 simulations (ALL\_EN) is also calculated. The developed raindrop–cloud droplet accretion (Chapter 4) and cloud droplet autoconversion (Lee and Baik, 2017) parameterizations are also implemented in the TE scheme, denoted by the ITE (improved TE) scheme. The result of the simulation with the ITE microphysics scheme, the YSU PBL scheme, and the Dudhia shortwave/RRTM longwave radiation schemes is compared with the results of other simulations. It is noted that the simulation with the TE microphysics scheme together with the YSU PBL scheme and the Dudhia shortwave/RRTM longwave radiation schemes is denoted by the CNTL simulation.

Figure 5.18 shows the spatial distribution of simulated 24-hr accumulated precipitation amount from the simulation with the six different microphysics schemes, their ensemble (MP\_EN), and the simulation with the ITE for 19 August 2015 in the innermost domain with a horizontal resolution of 1 km, focusing on the extreme precipitated area in the MP. All microphysics schemes simulate the spatial distribution of

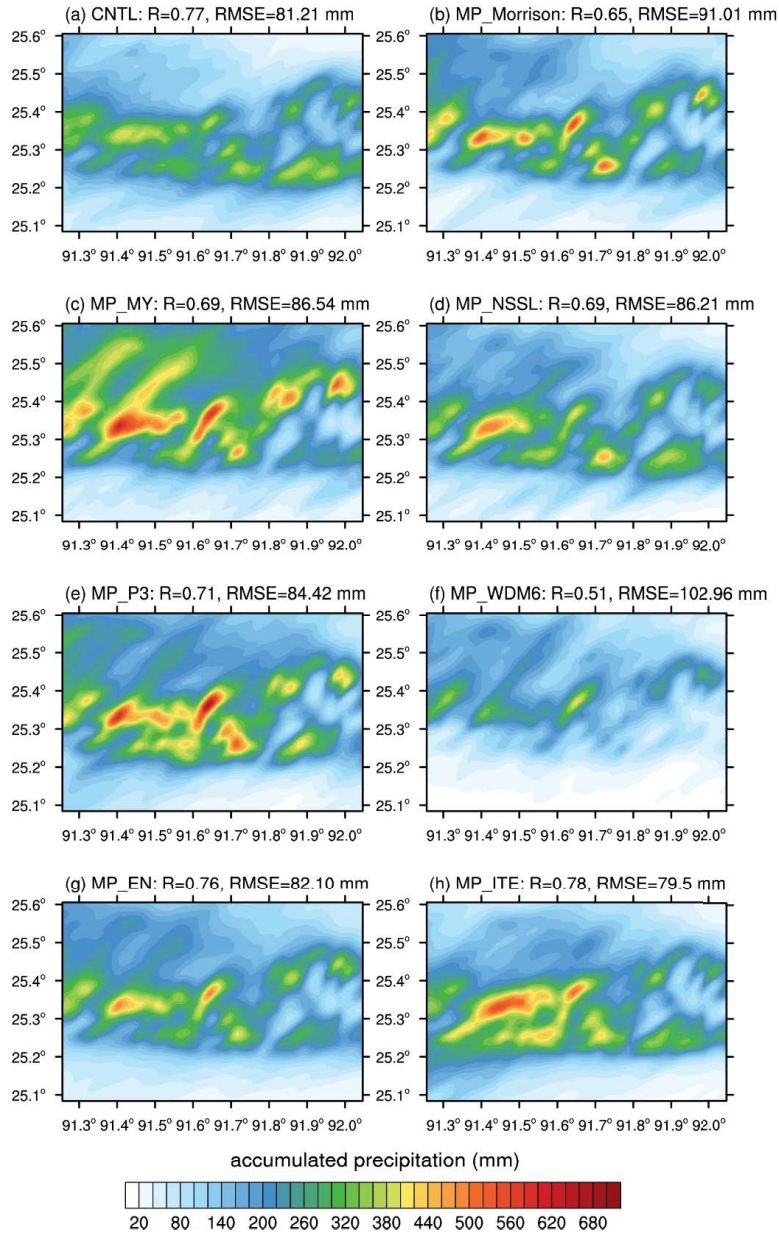


Figure 5.18 Spatial distribution of 24-hr accumulated precipitation amount in the simulations with different microphysics schemes: (a) CNTL, (b) MP\_Morrison, (c) MP\_MY, (d) MP\_NSSL, (e) MP\_P3, (f) MP\_WDM6, (g) is the ensemble average (MP\_EN), and (h) MP\_ITE, focusing on the southern slope of MP.

precipitation reasonably well, but precipitation intensity differs depending on which microphysics scheme is employed. Considering MP\_Morrison as a reference, a large amount of precipitation in the southern region of MP and a small amount of precipitation on the valley floor (Fig. 5.18b). This type of features is also evident in other simulations. MP\_ITE, MP\_MY, and MP\_P3 simulate more precipitation amount in the steep slope area, and CNTL and MP\_NSSL simulate a moderate amount of precipitation in that area. In contrast, MP\_WDM6 simulates a small amount of precipitation in the steep slope area. MP\_ITE shows the highest correlation ( $R = 0.78$ ) and the smallest RMSE (79.50 mm), and MP\_WDM6 shows the lowest correlation ( $R = 0.51$ ) and the largest RMSE (102.96 mm). The amounts of accumulated precipitation at Cherrapunji (471 mm) and Mawsynram (745 mm), the two locations that experienced the most extreme precipitation, are underestimated in all 11 simulations, but MP\_P3 simulates the closest precipitation amounts (311 mm at Mawsynram and 460 mm at Cherrapunji) among the simulation with the different microphysics schemes. MP\_EN shows a reasonably well simulated precipitation distribution with a relatively high correlation of 0.76 and a relatively low RMSE of 82.10 mm.

Figure 5.19 shows 24-hr accumulation precipitation distribution in the simulations with the different PBL schemes and their ensemble average. It is revealed that precipitation distribution and intensity are more sensitive to the PBL schemes than to the microphysical schemes. PBL\_MYJ simulates intense precipitation distribution in the southern slope of MP and a precipitation amount of 367 mm at Cherrapunji, while PBL\_ACM2 cannot capture intense precipitation in the southern slope of MP and simulates the smallest amount of precipitation at Cherrapunji (173 mm). The precipitation

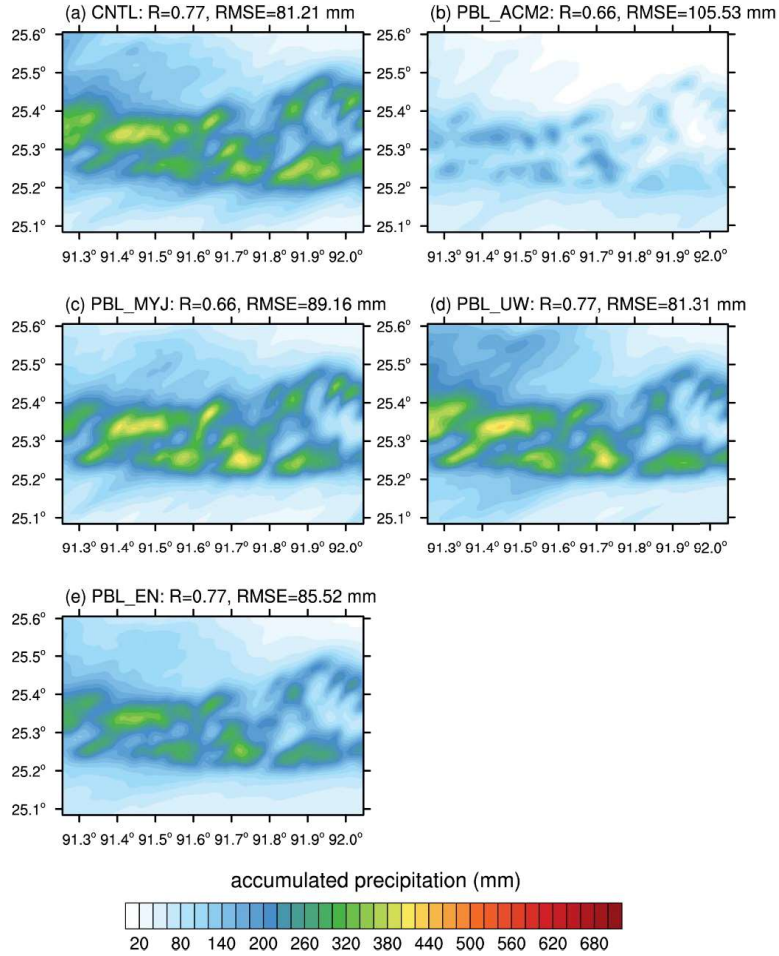


Figure 5.19 Same as Fig. 5.18 but for simulations with different PBL schemes: (a) CNTL, (b) PBL\_ACM2, (c) PBL\_MYJ, and (d) PBL\_UW. (e) is the ensemble average (PBL\_EN).



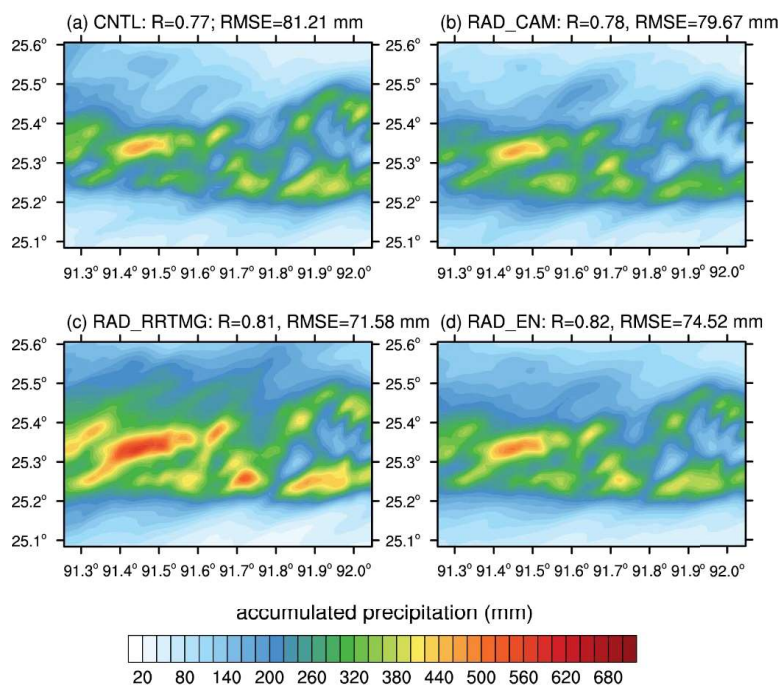


Figure 5.20 Same as Fig. 5.18 but for the simulations with different radiation schemes: (a) CNTL, (b) RAD\_CAM, and (c) RAD\_RRTMG. (e) is the ensemble average (RAD\_EN).

distribution and intensity in PBL\_YSU and PBL\_UW are similar to each other. The reduction of precipitation intensity in PBL\_YSU is seen compared to PBL\_MYJ. Both PBL\_UW and PBL\_YSU show better statistical scores. PBL\_EN shows intermediate statistical scores in this event.

Sensitivities to radiation schemes and the ensemble prediction are also examined (Fig. 5.20). RAD\_RRTMG shows the closest precipitation amount at Cherrapunji (449 mm) and Mawsynram (315 mm) compared to CNTL and RAD\_CAM. Moreover, RAD\_RRTMG exhibits a higher correlation and a lower RMSE compared to CNTL and RAD\_CAM. In CNTL and RAD\_CAM, intense precipitation is mainly distributed in a limited area in the western region of Mawsynram, but in RAD\_RRTMG, intense precipitation is distributed in a wider area in this region. RAD\_EN shows the highest correlation ( $R = 0.82$ ).

Figure 5.21 shows the spatial distribution of 24-hr accumulated precipitation amount for ensemble average of all 11 simulations. It is seen that intense precipitation is mainly concentrated in the mountain ridge areas. ALL\_EN shows a good performance, which is represented as a satisfactorily higher correlation ( $R = 0.79$ ) and lower RMSE (80.34 mm) than most of the individual ensemble members.

The results from the sensitivity experiments and ensemble prediction indicate that the simulation with the improved microphysics scheme that includes the stochastic autoconversion and accretion processes (MP\_ITE) considerably improves precipitation prediction. In fact, the performance of MP\_ITE is similar to ALL\_EN. The results also indicate a potential for ensemble prediction. Along with these finding, further studies for many precipitation cases are needed to better predict precipitation in the MP region.

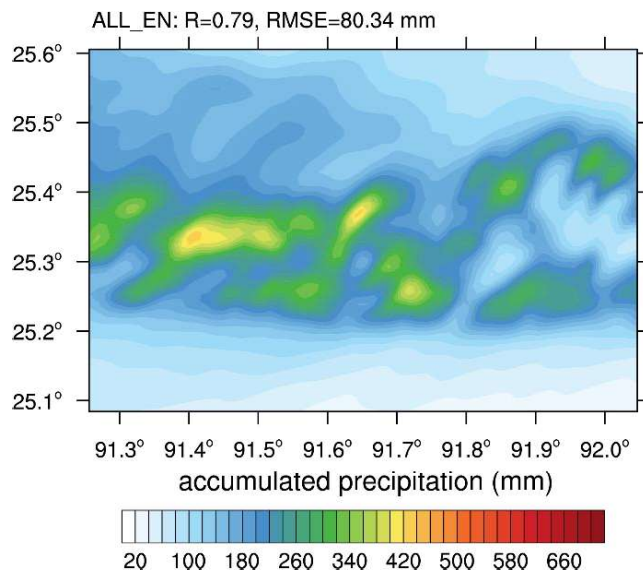


Figure 5.21 Same as Fig. 5.18 but for ensemble average of all 11 simulations.

## **6 Summary and conclusions**

### **6.1 Spatiotemporal variations of precipitation in Bangladesh revealed by nationwide rain gauge data**

This study examined observed spatial and temporal variations of precipitation in Bangladesh. For this, the rain gauge data in 3-h intervals at 35 stations for the period 2003–2016 and the reanalysis data were used. The annual precipitation amount is 2263 mm, and its spatial variation is large. The pre-monsoon and monsoon seasons have 17% and 73% of the annual precipitation amount, respectively. In the northern region of Bangladesh, the precipitation peaks in the late night to early morning in both the pre-monsoon and monsoon seasons. This is associated with the large horizontal convergence of low-level water vapor flux. On the other hand, in the southwestern region of the country, the precipitation peaks in the early evening in the pre-monsoon season and peaks in the afternoon in the monsoon season. The early evening maximum of precipitation in the pre-monsoon season is associated with the large convective instability in the late afternoon.

It was speculated that the Himalaya Mountains and the Meghalaya Plateau play roles in enhancing nighttime precipitation in the northern region of the country. However, we could not present the detailed processes and mechanisms only with the rain gauge data and the reanalysis data. Numerical studies with high-resolution cloud-resolving models will help to find involved processes and mechanisms. Bangladesh is affected by tropical cyclones which bring heavy rains in the country. It would be interesting to

examine to what extent tropical cyclones take part in the amount and spatial distribution of precipitation.

## **6.2 Evaluation and CSEOF analysis of IMERG data for precipitation studies in Bangladesh and surrounding regions**

This study evaluates the applicability of a satellite retrieval-based precipitation dataset, IMERG, to research on precipitation in Bangladesh and surrounding regions. The IMERG data successfully reproduce the observed seasonal variation of precipitation. The diurnal variation of precipitation is also generally well reproduced by the IMERG data, except for the overestimation of the degree of diurnal variability in the pre-monsoon season. Large underestimations of precipitation are found at Sylhet in the pre-monsoon and monsoon seasons, where the observed precipitation amounts are large and the IMERG data underestimate them. Because the correlation between 3-hourly precipitation amounts in the IMERG data and those in the rain gauge data is not very high ( $R = 0.51$ – $0.60$ ) and underestimations of heavy precipitation and overestimations of light precipitation are frequent, the use of the IMERG data for studying short-term individual precipitation events in Bangladesh and surrounding regions should be done with extra care. On the other hand, the IMERG data well reproduce the observed patterns of spatial and temporal distributions of precipitation averaged over a relatively long period, which encourages the use of the IMERG data for studying general precipitation characteristics in this region.

The IMERG data are used in the CSEOF analysis to examine important features of the diurnal variations of pre-monsoonal and monsoonal precipitation in Bangladesh and surrounding regions and their relationship with the low-level water vapor flux. The first mode of pre-monsoonal precipitation is characterized by enhanced precipitation in the northern region of Bangladesh and the Meghalaya Plateau region in the late night to early morning, which is related to the enhancement of the southerly component of moisture transport from the BOB to the southern slope of the Meghalaya Plateau. The second mode represents a north–south difference in precipitation which also becomes large in the late night to early morning, and this is linked with the diurnal variation of southwesterly moisture transport over Bangladesh.

For precipitation in the monsoon season, the first and second CSEOF modes show contrasting CSLV patterns. The first mode shows enhanced precipitation in the northern region of the BOB in 0600–1500 LST, which is related to the strengthening of westerly moisture transport over the BOB toward the Arakan Mountains in this time. In contrast, the second mode shows enhanced precipitation in the southern slopes of the Meghalaya Plateau and Himalayan Foothills in 0000–0600 LST, which is related to the southwesterly moisture transport being neither blocked nor deflected by the Arakan Mountains.

### **6.3 Development of a physically based raindrop-cloud droplet accretion parameterization and its evaluation through cloud and precipitation simulations**

Based on the stochastic collection equation, the accretion of cloud water by rainwater is newly parameterized for use in bulk microphysics schemes. The new

accretion parameterization employs the collection efficiency of each raindrop–cloud droplet pair, which allows a strong variability of accretion rate depending on the cloud droplet and raindrop size distributions even for given cloud water and rainwater mass contents. In the idealized and real-case simulations using a cloud-resolving model, NP generally yields larger accretion rates and smaller autoconversion rates compared to OP, resulting in the high acc/auto ratio. The relatively large mean raindrop size in NP caused by the high acc/auto ratio affects the sedimentation and evaporation processes of raindrops. Stronger net latent heating by condensation and evaporation processes is found in NP, which may contribute to enhancement of the cloud development and precipitation. In the simulations of a real precipitation event over Bangladesh, NP predicts the accumulated precipitation amount and its spatial distribution that are closer to the observation.

The relatively complicated calculation for the accretion process in NP compared to that in OP accompanies the increase in the computational cost but only to a small degree. For the idealized simulations in subsection 4.2.1 in which the cloud microphysics scheme is the only physics parameterization used, the simulation with NP costs total computation time  $\sim 2\%$  longer than that of the simulation with OP. In the real-case simulations where the contribution of the cloud microphysics scheme to the total computational load is relatively small, the computation time is reduced further.

Although the new parameterization provides a more rigorous estimation of the accretion rate, there still are some uncertainties. The assumption that the coalescence efficiency is 1 is one of them. If the coalescence efficiency for the accretion regime in reality is much smaller than 1, the acc/auto ratio and the mean raindrop radius predicted

by NP may have been overestimated. It is found that when the coalescence efficiency is assumed to be 0.75, the idealized simulation with NP still yields higher acc/auto ratio for a long time and overall greater raindrop radius than the idealized simulation with OP in which the coalescence efficiency is assumed to be 1, though differences in these variables between NP and OP are much reduced compared to those presented in subsection 4.2.1. This implies that examining reliable coalescence efficiency through physically rigorous and reproducible experiments may be needed to further improve the accuracy of the accretion rate estimation.

The clouds simulated in this study to examine the effects of NP are mainly deep convective clouds with high liquid water path where the role of the accretion process is important (Michibata and Takemura 2015). To see how these effects are different in shallow convective clouds with no ice microphysical processes involved, marine stratocumulus clouds are additionally simulated. The overall higher acc/auto ratio, larger mean raindrop radius, and smaller mean cloud droplet radius in NP than in OP are again predicted in these simulations, but the differences between those in NP and OP are not as big as the differences found in the deep convective cloud simulations, possibly because the importance of the accretion process relative to the autoconversion process is smaller compared to those in the deep convective cloud simulations (not shown).

The derivation of the accretion parameterization in this study shares many of the assumptions and methods with that of the autoconversion parameterization by LB17. Since the accretion and autoconversion processes are the two main processes that produce rainwater in warm clouds, coupling of the two parameterizations may improve the warm rain prediction, due to the elaborate methods used in the two parameterizations and a



good consistency between them. It is expected that some of the effects of NP found in this study would be cancelled out and some would be amplified. For example, the LB17 parameterization predicts higher acc/auto ratio compared to many other autoconversion parameterizations (e.g., Berry and Reinhardt 1974; Liu and Daum 2004; Seifert and Beheng 2006), and it will be worthwhile to examine how the high acc/auto ratio in NP will change when coupled with the LB17 parameterization. The combined effects of the two warm-rain collection parameterizations will be evaluated through simulations of various types of clouds and precipitation in further research. Furthermore, the parameterizations of the accretion processes involved with ice hydrometeors which share the methods with NP in this study (e.g., Jin et al. 2019) can be also combined to better represent the collection processes in mixed-phase clouds.

#### **6.4 Dynamical, thermodynamical, and cloud microphysical processes associated with extremely heavy precipitation in the Meghalaya Plateau region**

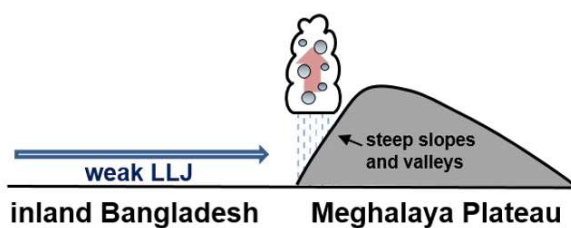
In this study, dynamical, thermodynamical, and cloud microphysical characteristics associated with the 18–19 August 2015 extremely heavy precipitation case in MP region are examined through high-resolution WRF model simulations. Three different simulations (CNTL, noMP, and HRES) are performed. The results of the CNTL and noMP simulations show that MP both initiates and intensifies precipitation. The schematic diagram in the Fig. 6.1 shows the overall processes associated with the extremely heavy precipitation event in MP. When LLJ is not fully developed and the water vapor transport is weak (P1), the orographic lifting induced by MP initiates

precipitation. Liquid hydrometeors and the associated warm cloud microphysical processes are dominant. The accretion process mainly contributes to the heavy precipitation in P1. When the nocturnal LLJ is fully developed and the water vapor transport is strong (P2), a number of precipitation systems are developed upwind of MP. The precipitation systems merge and intensifies in the upslope region. The stronger updrafts in P2 than in P1 results in the larger accretion rate which is the main contributor to the heavy precipitation over the upslope region. In addition, the melting of ice hydrometeors also contributes to the precipitation in P2. The local topographic effects on the extreme precipitation are investigated by comparing the results of the HRES simulation to those of the CNTL simulation. The increase in horizontal resolution makes the southern slope of MP steeper, resulting in intensified updrafts and weakened downdrafts. The region of increased vertical velocity (the northwest of Cherrapunji) is well-matched with the region of increased precipitation. The increase in simulated precipitation in the HRES simulation reduces the deviation from the rain gauge observation seen in the CNTL simulation, implying the importance of very high horizontal resolutions in the simulations of extremely heavy precipitation case in MP.

Furthermore, the sensitivities of the simulation of this extreme precipitation event to different physics parameterization schemes and the performance of the multiphysics ensemble are investigated. The simulations with different cloud microphysics schemes show similar spatial distribution patterns of precipitation but different precipitation intensities. The precipitation distribution and intensity are more sensitive to PBL schemes than radiation schemes. The multiphysics ensemble gives a satisfactorily better performance compared to most of the individual ensemble members. The performance of

(a)

P1



(b)

P2

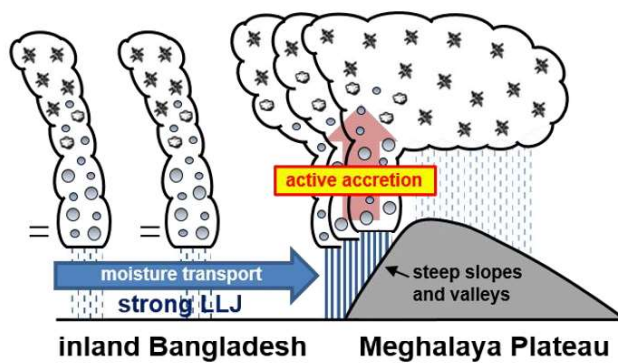


Figure 6.1 The schematic diagram for processes associated with extremely heavy precipitation in MP during (a) P1 and (b) P2.

the improved microphysics scheme that includes the stochastic autoconversion and accretion processes is similar to that of the multiphysics ensemble, improving precipitation prediction considerably.

## References

- Ahmed, M. K., M. S., Alam, A. H. M. Yousuf, and M. M. Islam, 2017: A long-term trend in precipitation of different spatial regions of Bangladesh and its teleconnections with El Niño/Southern Oscillation and Indian Ocean Dipole. *Theor. Appl. Climatol.*, **129**, 473–486.
- Ahmed, R., and S. Karmakar, 1993: Arrival and withdrawal dates of the summer monsoon in Bangladesh. *Int. J. Climatol.*, **13**, 727–740.
- Ahmed, R., and I.-K. Kim, 2003: Patterns of daily rainfall in Bangladesh during the summer monsoon season: Case studies at three stations. *Phys. Geogr.*, **24**, 295–318.
- Bari, S. H., M. M. Hussain, and N. Husna, 2017: Rainfall variability and seasonality in northern Bangladesh. *Theor. Appl. Climatol.*, **129**, 995–1001.
- Basher, M. A., M. A. Stiller-Reeve, A. K. M. S. Islam, and S. Bremer, 2018: Assessing climatic trends of extreme rainfall indices over northeast Bangladesh. *Theor. Appl. Climatol.*, **134**, 441–452.
- Beard, K. V., 1976: Terminal velocity and shape of cloud and precipitation drops aloft. *J. Atmos. Sci.*, **33**, 851–864.
- Beard, K. V., and S. N. Grover, 1974: Numerical collision efficiencies for small raindrops colliding with micron size particles. *J. Atmos. Sci.*, **31**, 543–550.
- Beard, K. V., and H. T. Ochs, 1995: Collisions between small precipitation drops. Part II: Formulas for coalescence, temporary coalescence, and satellites. *J. Atmos. Sci.*, **52**, 3977–3996.

- Berry, E. X., and R. L. Reinhardt, 1974: An analysis of cloud drop growth by collection: Part II. Single initial distributions. *J. Atmos. Sci.*, **31**, 1825–1831.
- Blackadar, A. K., 1957 : Boundary layer wind maxima and their significance for the growth of nocturnal inversions. *Bull. Amer. Meteor. Soc.*, **38**, 283–290.
- Bretherton, C. S., and S. Park, 2009: A new moist turbulence parameterization in the Community Atmosphere Model. *J. Climate*, **22**, 3422–3448.
- Cao, Q., G. Zhang, E. Brandes, T. Schuur, A. Ryzhkov, and K. Ikeda, 2008: Analysis of video disdrometer and polarimetric radar data to characterize rain microphysics in Oklahoma. *J. Appl. Meteor. Climatol.*, **47**, 2238–2255.
- Chowdhury, A. F. M. K., K. K. Kar, S. Shahid, R. Chowdhury, and M. M. Rashid, 2019: Evaluation of spatio-temporal rainfall variability and performance of a stochastic rainfall model in Bangladesh. *Int. J. Climatol.*, **39**, 4256–4273.
- Collins, W. D., and Coauthors, 2004: Description of the NCAR Community Atmosphere Model (CAM3.0). NCAR Tech. Note NCAR/TN-464+STR, 226 pp.
- Copernicus Climate Change Service (C3S) (2017) ERA5: Fifth generation of ECMWF atmospheric reanalysis of the global climate. Copernicus Climate Change Service Climate Data Store (CDS), accessed December 2019. <https://cds.climate.copernicus.eu/cdsapp#!/home>
- Dai, A., X. Lin, and K.-L. Hsu, 2007: The frequency, intensity, and diurnal cycle of precipitation in surface and satellite observations over low- and mid-latitudes. *Climate Dyn.*, **29**, 727–744.
- Dudhia, J., 1989: Numerical study of convection observed during the Winter Monsoon Experiment using a mesoscale two-dimensional model. *J. Atmos. Sci.*, **46**, 3077–

3107.

- Dziekan P., and H. Pawlowska, 2017: Stochastic coalescence in Lagrangian cloud microphysics. *Atmos. Chem. Phys.*, **17**, 13509–13520.
- Endo, N., J. Matsumoto, T. Hayashi, T. Terao, F. Murata, M. Kiguchi, Y. Yamane, and M. S. Alam, 2015: Trends in precipitation characteristics in Bangladesh from 1950 to 2008. *SOLA.*, **11**, 113–117.
- Fujinami, H., T. Sato, H. Kanamori, and F. Murata, 2017: Contrasting features of monsoon precipitation around the Meghalaya Plateau under westerly and easterly regimes. *J. Geophys. Res. Atmos.*, **122**, 9591–9610.
- Fujinami, H., D. Hatsuzuka, T. Yasunari, T. Hayashi, T. Terao, F. Murata, M. Kiguchi, Y. Yamane, J. Matsumoto, M. N. Islam, and A. Habib, 2011: Characteristic intraseasonal oscillation of rainfall and its effect on interannual variability over Bangladesh during boreal summer. *Int. J. Climatol.*, **31**, 1192–1204.
- Gaudet, B. J., and J. M. Schmidt, 2005: Assessment of hydrometeor collection rates from exact and approximate equations. Part I: A new approximate scheme. *J. Atmos. Sci.*, **62**, 143–159.
- Gilmore, M. S., J. M. Straka, and E. N. Rasmussen, 2004: Precipitation uncertainty due to variation in precipitation particle parameters within a simple microphysics scheme. *Mon. Wea. Rev.*, **132**, 2610–2627.
- Goswami, B. N., and R. S. A. Mohan, 2001: Intraseasonal oscillations and interannual variability of the Indian summer monsoon. *J. Climate*, **14**, 1180–1198.

- Goswami, B. B., P. Mukhopadhyay, R. Mahanta, and B. N. Gowami, 2010: Multiscale interaction with topography and extreme rainfall events in the northeast Indian region. *J. Geophys. Res.*, **115**, D12114.
- Habib, S. M. A., T. Sato, and D. Hatsuzuka, 2019: Decreasing number of propagating mesoscale convective systems in Bangladesh and surrounding area during 1998–2015. *Atmos. Sci. Lett.*, **20**, e879.
- Hersbach, H., and D. Dee., 2016: ERA5 reanalysis is in production. *ECMWF Newsletter*, No. 147, ECMWF Reading, United Kingdom, 7.
- Hersbach, H., B. Bell, P. Berrisford, S. Hirahara, A. Horányi, J. Muñoz-Sabater, J. Nicolas, C. Peubey, R. Radu, D. Schepers, A. Simmons, C. Soci, S. Abdalla, X. Abellan, G. Balsamo, P. Bechtold, G. Biavati, J. Bidlot, M. Bonavita, G. Chiara, P. Dahlgren, D. Dee, M. Diamantakis, R. Dragani, J. Flemming, R. Forbes, M. Fuentes, A. Geer, L. Haimberger, S. Healy, R.J. Hogan, E. Hólm, M. Janisková, S. Keeley, P. Laloyaux, P. Lopez, C. Lupu, G. Radnoti, P. Rosnay, I. Rozum, F. Vamborg, S. Villaume, and J.-N. Thépaut, 2020: The ERA5 global reanalysis. *Quart. J. Roy. Meteor. Soc.*, **146**, 1999–2049.
- He, X., F. Vejen, S. Stisen, T. O. Sonnenborg, and K. H. Jensen, 2011: An operational weather radar-based quantitative precipitation estimation and its application in catchment water resources modeling. *Vadose Zone J.*, **10**, 8–24.
- Hong, S.-Y., Y. Noh, and J. Dudhia, 2006: A new vertical diffusion package with an explicit treatment of entrainment processes. *Mon. Wea. Rev.*, **134**, 2318–2341.



- Hou, A. Y., R. K. Kakar, S. Neeck, A. A. Azarbarzin, C. D. Kummerow, M. Kojima, R. Oki, K. Nakamura, and T. Iguchi, 2014: The Global Precipitation Measurement mission. *Bull. Amer. Meteor. Soc.*, **95**, 701–722.
- Houze, R. A., Jr. 2014: *Cloud Dynamics, 2nd edition*, Academic Press, 432 pp.
- Huffman, G. J., D. T. Bolvin, D. Braithwaite, K. Hsu, R. Joyce, C. Kidd, E. J. Nelkin, S. Sorooshian, J. Tan, and P. Xie, 2019: *NASA global precipitation measurement (GPM) integrated multi-satellite retrievals for GPM (IMERG)*. Greenbelt, MD, USA: Algorithm Theoretical Basis Document (ATBD), NASA/GSFC.
- Huffman, G. J., D. T. Bolvin, E. J. Nelkin, and J. Tan, 2020: *Integrated Multi-satellite Retrievals for GPM (IMERG) technical documentation*. NASA/GSFC.
- Iacono, M. J., J. S. Delamere, E. J. Mlawer, M. W. Shephard, S. A. Clough, and W. D. Collins, 2008: Radiative forcing by long-lived greenhouse gases: Calculations with the AER radiative transfer models. *J. Geophys. Res.*, **113**, D13103.
- Islam, M. A., 2018: Statistical comparison of satellite-retrieved precipitation products with rain gauge observations over Bangladesh. *Int. J. Remote Sens.*, **39**, 2906–2936.
- Islam, M. N., and H. Uyeda, 2007: Use of TRMM in determining the climatic characteristics of rainfall over Bangladesh. *Remote Sens. Environ.* **108**, 264–276.
- Islam, M. N., and H. Uyeda, 2008: Vertical variations of rain intensity in different rainy periods in and around Bangladesh derived from TRMM observations. *Int. J. Climatol.*, **28**, 273–279.

- Islam, M. N., T. Terao, H. Uyeda, T. Hayashi, and K. Kikuchi, 2005: Spatial and temporal variations of precipitation in and around Bangladesh. *J. Meteor. Soc. Japan*, **83**, 21–39.
- Janjic, Z. I., 1994: The step-mountain eta coordinate model: Further developments of the convection, viscous sublayer, and turbulence closure schemes. *Mon. Wea. Rev.*, **122**, 927–945.
- Jin, H.-G., H. Lee, and J.-J. Baik, 2019: A new parameterization of the accretion of cloud water by graupel and its evaluation through cloud and precipitation simulations. *J. Atmos. Sci.*, **76**, 381–400.
- Johnson, J. S., Z. Cui, L. A., Lee, J. P. Gosling, A. M. Blyth, and K. S. Carslaw, 2015: Evaluating uncertainty in convective cloud microphysics using statistical emulation. *J. Adv. Model. Earth Syst.*, **7**, 162–187.
- Kain, J. S., 2004: The Kain–Fritsch convective parameterization: An update. *J. Appl. Meteor.*, **43**, 170–181.
- Kataoka, A., and T. Satomura, 2005: Numerical simulation on the diurnal variation of precipitation over northeastern Bangladesh: A case study of an active period 14–21 June 1995. *SOLA.*, **1**, 205–208.
- Kessler, E., 1969: On the distribution and continuity of water substance in atmospheric circulations. *Meteor. Monogr.*, **32**, Amer. Meteor. Soc.,
- Khain, A., D. Rosenfeld, A. Pokrovsky, U. Blahak, and A. Ryzhkov, 2011: The role of CCN in precipitation and hail in a mid-latitude storm as seen in simulations using a spectral (bin) microphysics model in a 2D dynamic frame. *Atmos. Res.*, **99**, 129–146.

- Khairoutdinov, M., and Y. Kogan, 2000: A new cloud physics parameterization in a large-eddy simulation model of marine stratocumulus. *Mon. Wea. Rev.*, **128**, 229–243.
- Kidd, C., A. Becker, G. J. Huffman, C. L. Muller, P. Joe, G. Skofronick-Jackson, and D. B Kirschbaum, 2017: So, how much of the Earth's surface is covered by rain gauges? *Bull. Amer. Meteor. Soc.*, **98**, 69–78.
- Kim, K.-Y., 2017: *Cyclostationary EOF Analysis: Theory and Applications*. Seoul National University Press, 432 pp.
- Kim, K.-Y., and B.-S. Kim, 2020: The effect of regional warming on the East Asian summer monsoon. *Climate Dyn.*, **54**, 3259–3277.
- Kim, K.-Y., and G. R. North, 1997: EOFs of harmonizable cyclostationary processes. *J. Atmos. Sci.*, **54**, 2416–2427.
- Kim, K.-Y., B. Hamlington, and H. Na, 2015: Theoretical foundation of cyclostationary EOF analysis for geophysical and climatic variables: Concepts and examples. *Earth-Sci. Rev.*, **150**, 201–218.
- Kim, K.-Y., J.-W. Roh, D.-K. Lee, and J.-G. Jhun, 2010: Physical mechanisms of the seasonal, subseasonal, and high-frequency variability in the seasonal cycle of summer precipitation in Korea. *J. Geophys. Res.*, **115**, D14110.
- Koenker, R., and G. Bassett Jr., 1978: Regression quantiles. *Econometrica*, **46**, 33–50.
- Kripalani, R. H., S. Inamdar, and N. A. Sontakke, 1996: Rainfall variability over Bangladesh and Nepal: Comparison and connections with fractures over India. *Int. J. Climatol.*, **16**, 689–703.
- Kullgren, K., and K.-Y. Kim, 2006: Physical mechanisms of the Australian summer

- monsoon: 1. Seasonal cycle. *J. Geophys. Res.*, **111**, D20104.
- Lee, H., and J.-J. Baik, 2017: A physically based autoconversion parameterization. *J. Atmos. Sci.*, **74**, 1599–1616.
- Lim, K.-S. S., and S.-Y. Hong, 2010: Development of an effective double-moment cloud microphysics scheme with prognostic cloud condensation nuclei (CCN) for weather and climate models. *Mon. Wea. Rev.*, **138**, 1587–1612.
- Li, C. F., and M. Yanai, 1996: The onset and interannual variability of the Asian summer monsoon in relation to land–sea thermal contrast. *J. Climate*, **9**, 358–375.
- Liu, Y., and P. H. Daum, 2004: Parameterization of the autoconversion. Part I: Analytical formulation of the Kessler-type parameterizations. *J. Atmos. Sci.*, **61**, 1539–1548.
- Long, A. B., 1974: Solutions to the droplet collection equation for polynomial kernels. *J. Atmos. Sci.*, **31**, 1040–1052.
- Michibata, T., and T. Takemura, 2015: Evaluation of autoconversion schemes in a single model framework with satellite observations. *J. Geophys. Res. Atmos.*, **120**, 9570–9590.
- Milbrandt, J. A., and M. K. Yau, 2005: A multimoment bulk microphysics parameterization. Part II: A proposed three-moment closure and scheme description. *J. Atmos. Sci.*, **62**, 3065–3081.
- Mlawer, E. J., S. J. Taubman, P. D. Brown, M. J. Iacono, and S. A. Clough, 1997: Radiative transfer for inhomogeneous atmospheres: RRTM, a validated correlated-k model for the longwave. *J. Geophys. Res.*, **102**, 16663–16682.
- Mohsenipour, M., S. Shahid, G. F. Ziarh, and Z. M. Yaseen, 2020: Changes in monsoon rainfall distribution of Bangladesh using quantile regression model *Theor. Appl.*

- Climatol.*, **142**, 1329–1342.
- Morrison, H., and W. W. Grabowski, 2007: Comparison of bulk and bin warm-rain microphysics models using a kinematic framework. *J. Atmos. Sci.*, **64**, 2839–2861.
- Morrison, H., and J. A. Milbrandt, 2015: Parameterization of cloud microphysics based on the prediction of bulk ice particle properties. Part I: Scheme description and idealized tests. *J. Atmos. Sci.*, **72**, 287–311.
- Morrison, H., J. A. Curry, and V. I. Khvorostyanov, 2005: A new double-moment microphysics parameterization for application in cloud and climate models. Part I: Description. *J. Atmos. Sci.*, **62**, 1665–1677.
- Morrison, H., G. Thompson, and V. Tatarskii, 2009: Impact of cloud microphysics on the development of trailing stratiform precipitation in a simulated squall line: Comparison of one- and two-moment schemes. *Mon. Wea. Rev.*, **137**, 991–1007.
- Murata, F., T. Terao, H. Fujinami, T. Hayashi, H. Asada, J. Matsumoto, and H. J. Syiemlieh, 2017: Dominant synoptic disturbance in the extreme rainfall at Cherrapunji, Northeast India, based on 104 years of rainfall data (1902-2005). *J. Climate*, **30**, 8237–8251.
- Murata, F., T. Terao, T. Hayashi, H. Asada, and J. Matsumoto, 2008: Relationship between atmospheric conditions at Dhaka, Bangladesh, and rainfall at Cherrapunjee, India. *Nat. Hazards*, **44**, 399–410.
- Nair, S., G. Srinivasan, and R. Nemani, 2009: Evaluation of multi-satellite TRMM derived rainfall estimates over a western state of India. *J. Meteor. Soc. Japan*, **87**, 927–939.
- Naumann, A. K., and A. Seifert, 2016: Evolution of the shape of the raindrop size

- distribution in simulated shallow cumulus. *J. Atmos. Sci.*, **73**, 2279–2297.
- Ohsawa, T., T. Hayashi, Y. Mitsuta, and J. Matsumoto, 2000: Intraseasonal variation of monsoon activities associated with the rainfall over Bangladesh during the 1995 summer monsoon season. *J. Geophys. Res.*, **105**, 29445–29459.
- Ohsawa, T., H. Ueda, T. Hayashi, A. Watanabe, and J. Matsumoto, 2001: Diurnal variations of connective activity and rainfall in tropical Asia. *J. Meteor. Soc. Japan*, **79**, 333–352.
- Orr, A., C. Listowski, M. Coultet, E. Collier, W. Immerzeel, P. Deb, and D. Bannister, 2017: Sensitivity of simulated summer monsoonal precipitation in Langtang Valley, Himalaya, to cloud microphysics schemes in WRF. *J. Geophys. Res.*, **122**, 6298–6318.
- Paukert, M., J. Fan, P. J. Rasch, H. Morrison, J. A. Milbrandt, J., Shpund, and A. Khain, 2019: Three-moment representation of rain in a bulk microphysics model. *J. Adv. Model. Earth Syst.*, **11**, 257–277.
- Pinsky, M., A. Khain, and M. Shapiro, 2001: Collision efficiency of drops in a wide range of Reynolds numbers: Effects of pressure on spectrum evolution. *J. Atmos. Sci.*, **58**, 742–764.
- Pleim, J. E., 2007: A combined local and nonlocal closure model for the atmospheric boundary layer. Part I: Model description and testing. *J. Appl. Meteor. Climatol.*, **46**, 1383–1395.
- Prasad, B., 1970: Diurnal variation of rainfall in India. *Indian J. Meteor. Geophys.*, **25**, 245–250.

- Rahman, M. A., L. Yunsheng, and N. Sultana, 2017: Analysis and prediction of rainfall trends over Bangladesh using Mann–Kendall, Spearman’s rho tests and ARIMA model. *Meteor. Atmos. Phys.*, **129**, 409–424.
- Roh, J.-W., K.-Y. Kim, and J.-G. Jhun, 2012: Decadal changes in the physical mechanisms of the seasonal cycle of summertime precipitation variability in Korea. *J. Geophys. Res.*, **117**, D07115.
- Romatschke, U., and R. A. Houze Jr., 2011: Characteristics of precipitating convective systems in the premonsoon season of South Asia. *J. Hydrometeor.*, **12**, 157–180.
- Romatschke, U., S. Medina, and R. A. Jr. Houze, 2010: Regional, seasonal, and diurnal variations in extreme convection in the South Asian region. *J. Climate*, **23**, 419–439.
- Sato, T., 2013: Mechanism of orographic precipitation around the Meghalaya Plateau associated with intraseasonal oscillation and the diurnal cycle. *Mon. Wea. Rev.* **141**, 2451–2466.
- Schneider, U., P. Finger, A. Meyer-Christoffer, M. Ziese, and A. Becker, 2018: *Global precipitation analysis products of the GPCC*. GPCC internet publication, DWD.
- Seifert, A., and K. D. Beheng, 2001: A double-moment parameterization for simulating autoconversion, accretion and selfcollection. *Atmos. Res.*, **59**, 265–281.
- Seifert, A., and K. D. Beheng, 2006: A two-moment cloud microphysics parameterization for mixed-phase clouds. Part 1: Model description. *Meteor. Atmos. Phys.*, **92**, 45–66.
- Seifert, A., U. Blahak, and R. Buhr, 2014: On the analytic approximation of bulk collision rates of non-spherical hydrometeors. *Geosci. Model Dev.*, **7**, 463–478.

- Shahid, S., and O. S. Khairulmaini, 2009: Spatio-temporal variability of rainfall over Bangladesh during the time period 1969-2003. *Asia-Pac. J. Atmos. Sci.*, **45**, 375–389.
- Skamarock, W. C., J. B. Klemp, J. Dudhia, D. O. Gill, D. M. Barker, M. G. Duda, X.-Y. Huang, W. Wang, and J. G. Powers, 2008: *A description of the advanced research WRF version 3*. NCAR Technical Note, NCAR/TN-475+STR, NCAR.
- Skamarock, W. C., J. B. Klemp, J. Dudhia, D. O. Gill, L. Zhiquan, J. Berner, W. Wang, J. G. Powers, M. G. Duda, D. M. Barker, and X.-Y. Huang, 2019: *A description of the Advanced Research WRF model version 4*. NCAR Technical Note, NCAR/TN-475+STR. NCAR
- Straub, W., K. D. Beheng, A. Seifert, J. Schlottke, and B. Weigand, 2010: Numerical investigation of collision-induced breakup of raindrops. Part II: Parameterizations of coalescence efficiencies and fragment size distributions. *J. Atmos. Sci.*, **67**, 576–588.
- Tan, J., G. J. Huffman, D. T. Bolvin, and E. J. Nelkin, 2019: Diurnal cycle of IMERG V06 precipitation. *Geophys. Res. Lett.*, **46**, 13584–13592.
- Tang, G., Y. Ma, D. Long, L. Zhong, and Y. Hong, 2016: Evaluation of GPM Day-1 IMERG and TMPA Version-7 legacy products over Mainland China at multiple spatiotemporal scales. *J. Hydrol.*, **533**, 152–167.
- Tanoue, M., K. Ichiyanaagi, K. Yoshimura, M. Kiguchi, T. Terao, and T. Hayashi, 2018: Seasonal variation in isotopic composition and the origin of precipitation over Bangladesh. *Prog. Earth Planet. Sci.*, **5**, 77.



- Tarek, M. H., A. Hassan, J. Bhattacharjee, S. H. Choudhury, and A. B. M. Badruzzaman, 2017: Assessment of TRMM data for precipitation measurement in Bangladesh. *Meteor. Appl.*, **24**, 349–359.
- Terao, T., M. N. Islam, T. Hayashi, and T. Oka, 2006: Nocturnal jet and its effects on early morning rainfall peak over northeastern Bangladesh during the summer monsoon season. *Geophys. Res. Lett.*, **33**, L18806.
- Tewari, M., F. Chen, W. Wang, J. Dudhia, M. LeMone, K. Mitchell, M. Ek, G. Gayno, J. Wegiel, and R. Cuenca, 2004: Implementation and verification of the unified Noah land surface model in the WRF model. *20th Conf. on Weather Analysis and Forecasting/16th Conf. on Numerical Weather Prediction*, Seattle, WA, Amer. Meteor. Soc., 14.2a.
- Thompson, G., and T. Eidhammer, 2014: A study of aerosol impacts on clouds and precipitation development in a large winter cyclone. *J. Atmos. Sci.*, **71**, 3636–3658.
- Thompson, G., P. R. Field, R. M. Rasmussen, and W. D. Hall, 2008: Explicit forecasts of winter precipitation using an improved bulk microphysics scheme. Part II: Implementation of a new snow parameterization. *Mon. Wea. Rev.*, **136**, 5095–5115.
- Tripoli, G. J., and W. R. Cotton, 1980: A numerical investigation of several factors contributing to the observed variable intensity of deep convection over South Florida. *J. Appl. Meteor.*, **19**, 1037–1063.
- Walko, R. L., W. R. Cotton, M. P. Meyers, and J. Y. Harrington, 1995: New RAMS cloud microphysics parameterization. Part I: The single-moment scheme. *Atmos. Res.*, **38**, 29–62.

- Wood, R., 2005: Drizzle in stratiform boundary layer clouds. Part II: Microphysical aspects. *J. Atmos. Sci.*, **62**, 3034–3050.
- Wu, P., B. Xi, X. Dong, and Z. Zhang, 2018: Evaluation of autoconversion and accretion enhancement factors in general circulation model warm-rain parameterizations using ground-based measurements over the Azores. *Atmos. Chem. Phys.*, **18**, 17405–17420.
- Wu, C.-H., H.-H. Hsu, and M.-D. Chou, 2014: Effect of the Arakan Mountains in the northwestern Indochina Peninsula on the late May Asian monsoon transition. *J. Geophys. Res. Atmos.*, **119**, 10769–10779.
- Yamane, Y., and T. Hayashi, 2006: Evaluation of environmental conditions for the formation of severe local storms across the Indian subcontinent. *Geophys. Res. Lett.*, **33**, L17806.
- Yang, G. Y., and J. Slingo, 2001: The diurnal cycle in the tropics. *Mon. Wea. Rev.*, **129**, 784–801.
- Yong, B., D. Liu, J. J. Gourley, Y. Tian, G. J. Huffman, L. Ren, and Y. Hong, 2015: Global view of real-time TRMM multisatellite precipitation analysis: Implications for its successor Global Precipitation Measurement. *Bull. Amer. Meteor. Soc.*, **96**, 283–296.
- Yuan, W., J. Li, H. Chen, and R. Yu, 2012: Intercomparison of summer rainfall diurnal features between station rain gauge data and TRMM 3B42 product over central eastern China. *Int. J. Climatol.*, **32**, 1690–1696.
- Zhou, T., R. Yu, H. Chen, A. Dai, and Y. Pan, 2008: Summer precipitation frequency, intensity, and diurnal cycle over China: a comparison of satellite data with rain

gauge observations. *J. Climate*, **21**, 3997–4010.

## 초 록

방글라데시는 남아시아 몬순의 영향을 크게 받는 지역이다. 이 지역은 잦은 홍수에 의한 피해가 크기 때문에, 전국적인 강수 기후에 대한 연구가 필요하다. 본 연구에서는 2003년부터 2016년까지 35개 관측소의 우량계 관측 자료를 이용해 방글라데시 강수의 시공간 분포를 조사하였다. 방글라데시의 연 강수량은 2263 mm이며, 공간적으로 큰 변동성을 보인다. 연 강수량은 방글라데시 남동 해안 지역과 메갈라야 고원 근방 지역에서 크며, 중서부 지역에서는 적다. 계절별로는, pre-monsoon 기간(3-5월)과 monsoon 기간(6-9월)의 강수량이 각각 연 강수량의 17%, 73%를 차지한다. 강수의 일 변동 양상은 방글라데시 내에서도 지역에 따라 다르게 나타난다. 방글라데시 북부 지역에서는 pre-monsoon, monsoon 기간 모두에서 일 최대 강수가 늦은 밤과 이른 아침에 나타난다. 이는 이 시간대에 나타나는 하층 수증기 속의 강한 수렴과 관련된다. 야간에 하층 풍속이 증가하여 히말라야 산맥과 메갈라야 고원으로의 수증기 수송이 강화되고, 이것이 야간 강수 증가에 영향을 미친 것으로 보인다. 방글라데시 남서부 지역에서는 일 최대 강수가 pre-monsoon 기간에는 오후의 강한 대류 불안정에 의해 이른 저녁에 나타나고, monsoon 기간에는 이른 오후에 나타난다. 방글라데시 남동부 지역에서는 pre-monsoon 기간 강수의 일 변동성이 다른 지역에 비해 약하며, monsoon 기간에는 늦은 밤과 이른 아침에 일 최대 강수가 나타난다.

방글라데시 및 주변 지역과 같이 지상 우량계가 충분히 많지 않은 지역에서는 높은 시공간 해상도를 갖는 위성 관측 기반 강수 자료를 활용하는 것이 강수 연구에 큰 도움이 될 수 있다. 본 연구에서는 방글라데시와 주변 지역 강수 연구에서 IMERG(Integrated Multi-satellite Retrievals for Global Precipitation Measurement) 자료의 활용 가능성을 평가하고, 이 자료와 CSEOF(cyclostationary empirical

orthogonal function) 분석 방법을 이용하여 이 지역 강수의 중요한 일 변동 특징을 조사하였다. IMERG 자료는 pre-monsoon 기간 강수의 일 변동성을 과대추정하나, 전체적으로는 강수의 일 변동 양상을 잘 나타낸다. IMERG 자료는 강수의 공간 분포 역시, 방글라데시 북동부 지역 내 급격한 공간 변동성을 재현하지 못하는 것을 제외하면 전체적으로 잘 나타낸다. 이는 방글라데시 및 주변 지역 강수 특징을 연구하는 데 있어 IMERG 자료가 유용할 수 있음을 보여준다. 다음으로 CSEOF 분석을 통해 이 지역 pre-monsoon과 monsoon 기간 강수의 중요한 일 변동 특징을 밝혔다. Pre-monsoon 기간 강수의 특징은 방글라데시 북부 지역과 메갈라야 고원 지역에서 늦은 밤과 이른 아침에 강수가 강화되는 것이며, 이는 남풍에 의한 벵골만으로부터의 수증기 수송, 그리고 남서풍에 의한 수증기 수송과 관련되어 있다. Monsoon 기간 강수의 경우 첫번째, 두번째 CSEOF 모드가 대조적으로 나타난다. 첫번째 CSEOF 모드에서는 0600–1500 LST에 벵골만 북부에서 강수가 강화되는 모습이 나타나는데, 이는 서풍에 의한 벵골만에서 아라칸 산맥으로의 강한 수증기 수송과 연관된다. 두번째 CSEOF 모드에서는 0000–0600 LST에 메갈라야 고원과 히말라야 산맥의 남쪽 경사면에서 강수가 강화되는 모습이 나타나며, 이는 이 시간대에 나타나는 남서풍이 아라칸 산맥에 의해 가로막히거나 굴절되지 않고 메갈라야 고원 및 히말라야 산맥 남쪽 경사면에 수증기를 활발히 수송하기 때문이다.

Bulk 구름 미세물리 방안의 결착 과정은 확률 포착 방정식을 이용해 모수화할 수 있다. 본 연구에서는 빗방울과 구름 물방울 크기에 따라 달라지는 포착 효율을 확률 포착 방정식에 적용하여 빗방울 및 구름 물방울 크기 분포에 따른 결착률의 큰 변동성을 고려할 수 있는 새 결착 과정 모수화를 개발하였다. 새 결착 과정 모수화(NP)를 평가하기 위해 NP를 구름 분해 모형에 적용하여 연속 포착 방정식에 기반한 기존의 결착 과정 모수화(OP)를 대신하도록 하였다. 이상화된 깊은 대류

구름에 대한 수치 실험에서 NP는 OP에 비해 결착률을 전체적으로 크게 예측하고, 이로 인해 자동변환율은 낮게 나타나며, 결착률-자동변환율 비가 높아져 빗방울의 평균 크기가 증가한다. 빗방울의 평균 크기의 증가는 빗방울 낙하 속도의 증가로 이어져 지표 강수의 시작 시간이 앞당겨지며, 빗방울의 증발 냉각이 약화된다. 한편, 주어진 우수함량과 구름 수함량에 대해 NP의 결착률은 OP에 비해 상대적으로 넓은 분포를 보이는데, 이는 결착 과정을 모수화하는 데 있어 질량 함량만이 아니라 다른 미세물리 변수에 대한 결착률의 변동성을 적절히 고려해야 한다는 것을 보여준다. 방글라데시의 실제 강수 사례에 대한 수치 실험도 수행하였다. 여기서 나타난 결착 과정 모수화 간 차이는 이상화된 깊은 대류 구름 실험에서 나타난 것과 유사한 양상을 보이나, 모수화 간 차이의 정도는 작게 나타난다. 누적 강수량의 공간 분포는 NP를 사용했을 때 관측과 보다 유사하게 나타난다.

인도 북동부에 위치한 메갈라야 고원(MP)은 세계에서 가장 비가 많이 오는 지역 중 하나이다. 2015년 8월 18-19일, MP의 남쪽 경사면에는 매우 강한 강수가 내렸으며, 일 최대 강수량은 Mawsynram에서 745 mm에 달했다. 본 연구에서는 고해상도 수치 실험을 통해 이 극한 강수 사례와 관련된 역학 과정과 구름 미세물리 과정을 알아보았다. 수평 격자 해상도가 1 km인 실험(CNTL)은 관측된 누적 강수의 공간 분포를 잘 재현한다. 온난다습한 공기를 MP로 수송하는 하층 제트가 상대적으로 약했던 18일 1500 LST-19일 0000 LST(P1)에 MP의 오르막 지역에는 지형성 상승에 의해 이 지역에서 생성된 강수가 내리며, 이 강수는 MP를 제거한 실험(noMP)에서는 거의 나타나지 않는다. P1의 강수에는 온난 미세물리 과정이 지배적인 역할을 한다. 한편, 하층 제트가 강화된 19일 0000-0900 LST(P2)에는 noMP 실험에서도 중간 정도의 강수량이 MP의 오르막 지역에 나타나며, CNTL 실험에서는 이 지역에 훨씬 많은 강수량이 나타난다. 이 시기에는 MP의 풍상측에서 깊은 대류계가 여럿 발달하여 MP 쪽으로 이동한다. 이 대류계들은

MP의 오르막 지역에서 합쳐져 더욱 강해진다. MP의 급경사면에서 하층의 강한 상승류에 의해 결착 과정이 상당히 강화되며, 이는 강한 강수로 이어진다. 수평 격자 해상도가 1/3 km인 실험(HRES)에서는 MP의 오르막 지역의 강수가 CNTL 실험에 비해 더 강하게 나타난다. 높아진 수평 해상도에 의해 이 지역의 경사면들이 더 가파르게 표현되고, 이로 인해 상승 기류가 보다 강화된다. HRES 실험에서는 모의된 강수량과 관측된 강수량의 차이가 CNTL 실험에 비해 작게 나타나며, 이는 MP의 극한 강수를 모의하는 데 매우 높은 수평 해상도를 사용하는 것이 중요하다는 것을 보여준다. 추가적으로, 이 강수 사례에 대해 여러 물리 모수화 방안에 따른 강수 예측의 민감도를 조사하고, 다중물리 앙상블의 강수 예측 성능을 평가하였다. 이를 위해 서로 다른 6개의 구름 미세물리 방안과 4개의 행성경계층 방안, 3개의 복사 방안을 사용하였고, 각 방안을 사용한 실험과 이들의 다중물리 앙상블의 강수 예측 성능을 평가하였다. 여기에 더해 확률 포착 방정식에 기반한 자동변환 및 결착 과정 모수화를 포함하도록 개선한 구름 미세물리 방안의 강수 예측 성능 또한 평가하였다. 서로 다른 구름 미세물리 방안을 사용했을 때 강수의 공간 분포 양상은 서로 유사하나, 강수 강도에 있어 큰 차이를 보인다. 다중물리 앙상블은 대부분의 개별 실험에 비해 좋은 강수 예측 성능을 보인다. 개선된 구름 미세물리 방안의 경우, 다중물리 앙상블과 비슷한 성능을 보여, 구름 미세물리 모수화의 개선이 강수 예측을 크게 향상시키는 것으로 드러났다.

주요어: 몬순 강수, 방글라데시, 메갈라야 고원, 일 변동, IMERG, 결착 과정 모수화, 극한 강수

학 번: 2017-33971

## Acknowledgements

I can clearly remember my first day at Seoul National University, four years ago, when I met my Ph.D. supervisor Professor Jong-Jin Baik. He has been the primary source of my motivation and energy to keep going on this long academic journey from that day. I would like to express my sincere gratitude to my supervisor Professor Baik, without whom I cannot imagine finishing my Ph.D. within four years. I could not have imagined having a better supervisor and mentor for my Ph.D. study. I would also like to thank the rest of my dissertation committee members: Professor Sungsu Park, Professor Sang-Woo Kim, Professor Hyunho Lee and Professor Hyo-Jong Song for their insightful comments and encouragement in this research work.

My sincere thanks also go to Dr. Han-Gyul Jin who gave me opportunities to ask any questions related to my Ph.D. study and taught me programming and simulation setup during my Ph.D. journey. Without his precious support it would not have been possible to conduct this research. I am very grateful to my fellow lab-mates Ye-Lim Jeon, Minchae Jwa, Joohyun Lee, Dr. Sungju Moon, Dr. Beom-Soon Han, Dr. Jambajants Lkhamjav, Jong-Won Kim, Seong-Ho Hong and Hyejin Lim for their helps in programming and for stimulating discussions during my study. I would like to give special thanks to Minchae Jwa for her endless support that led me to better understand Korean culture and to communicate with other people for my family needs.

I would like to thank Seoul National University for providing me the SNU President Fellowship and also thank SEES and OIA secretaries and SPF coordinators for their helps.



Finally, I would like to thank my family: my parents for supporting me spiritually throughout writing this dissertation and especially my wife, Fahima Akter Kona, my sons, Faiyaz Al Farabi and Fawad Al Fahmi for their love, understanding, prayers and continuous support to complete this research work.